Merger of Multiple Vortices

A Thesis
Submitted for the Degree of
Master of Science (Engineering)

by

Rohith V. S

Engineering Mechanics Unit
Jawaharlal Nehru Centre for Advanced Scientific Research
(A Deemed University)
Bangalore – 560 064

OCTOBER 2012

To Father and Mother

DECLARATION

I hereby declare that the matter embodied in the thesis entitled "**Merger of Multiple Vortices**" is the result of investigations carried out by me at the Engineering Mechanics Unit, Jawaharlal Nehru Centre for Advanced Scientific Research, Bangalore, India under the supervision of **Prof. Rama Govindarajan** and that it has not been submitted elsewhere for the award of any degree or diploma.

In keeping with the general practice in reporting scientific observations, due acknowledgment has been made whenever the work described is based on the findings of other investigators.

Rohith V. S

CERTIFICATE

I hereby certify that the matter embodied in this thesis entitled "**Merger of Multiple Vortices**" has been carried out by **Mr. Rohith V. S** at the Engineering Mechanics Unit, Jawaharlal Nehru Centre for Advanced Scientific Research, Bangalore, India under my supervision and that it has not been submitted elsewhere for the award of any degree or diploma.

Prof. Rama Govindarajan
(Research Supervisor)

Acknowledgements

First, I would like to thank my *parents*, elder brother, *Vikhram*, and family. They have been the greatest source of inspiration throughout my pursuits. I have always found their advise and philosophy to fall back on whenever I needed help to maintain focus and motivation. I dedicate this thesis to my *parents*, for giving me the opportunity and freedom to pursue research. And to *Vikhy* for setting the bar so high!

I would like to express my sincere gratitude to *Prof. Rama Govindarajan*, my advisor during the Masters program. I am extremely fortunate to have had the opportunity to work under her advise on vortex dynamics, a topic of my interest. During the course of the program, I have learned several things from her - on the art of conducting research, discipline, organization, communication, patience and most importantly, ethics. One of the most remarkable qualities that distinguishes her from other researchers is her ability to ask fundamental questions in problems of practical significance. *Rama* has also been extremely supportive and encouraging, even through difficult times. I am sure that my experience of working with her will stand me in good stead for future endeavors.

I thank *Prof. K. R. Sreenivas* for offering the course on Heat Transfer, where I had my first glimpse of Geophysical fluid dynamics while working on the course project. I would also like to thank *Prof. Jai Sukhatme* and *Prof. Debashish Sengupta* for the GFD course and advice on the field of climate sciences. Special thanks to *Prof. Roddam Narasimha* for his comments and suggestions on the thesis, and of course his words of wisdom and encouragement.

During my two years in JNC, I was lucky to have made so many wonderful friends, who have been with me through good times and bad ones. First, I would like to mention *Anubhab*, who has been a mentor and a friend during my stay. I have learnt so much from *Dada* during our countless discussions and debates, be it on technical issues, politics, philosophy, sports, movies or even mundane ones. I really appreciate his display of patience during all our conversations. Also, I must mention the help that I received for the derivation of the generalized Lamb-Oseen and for the stability analysis. His comments and criticism have definitely improved my thesis. Apart from this, I would like to thank *Anubhab* and *Senjuti* for throwing great parties in their home. The arrival of *Senjuti* meant playing 'catch me if you can' with *Anubhab*. She however made up for it dishing out awesome cakes and cocktails.

I am lucky to have a friend like *Navaneeth*, who has taught me a great deal on many aspects of life. I can never forget the discussions during lunch in *Chandraiah*, when except for great food, both of us has something or the other to complain about. Apart from his great taste in music, I have also enjoyed listening to his views on philosophy and religion. He has been an inspiration to me and I will definitely miss him. Anyways, we still have unfinished business in connection to Leh/Ladakh.

Rajesh has been another special friend here, always ready to go out for a samosa and relive his childhood days. He was and still is the passport to gossip in JNC. They say two is company, three is a crowd. That however, was not the case during dinner at *Nandini* with *Jose* and *Prasanth*, whose company I enjoyed very much. Jose and I go back to our college days in RVCE, when mass bunking was the order of the day. Of course, there is *Prasanth (PP)*, who will do anything and everything to simulate a cloud. I am sure he will inspire hordes of budding graduate students. And, talking about inspiration, I only needed to strain my neck to find *Sumesh*, who's discipline and organizational skills are second to none. I must also mention *Ponnu*, who has been and always will be the subject of friendly banter in the EMU circle. I would like to thank *Saikishan*, who is always eager to go out on a drive to escape the lonely constraints of JNC, and share a pizza or a drink. And talking about pizzas, I would be doing injustice by not mentioning Srikanth, who also helped me out with technical issues during my first year in JNC. I also enjoyed the light conversations with *Rakshith* in EMU 105.

Being a nocturnal animal, I enjoyed the company of *Dhiraj* during my all nighters. Special mention goes to *Deepak*, the lead and leading vocalist of JNC. And what would EMU be without the controversy courted by *Croor*. Controversy also spilled over on the football pitch during tense do or die football matches, when it was every man for himself. On that note, I would like to mention *Milind*, *Shashank*, *Sunil*, *Rohan*, *Siddharth*, *Reddy*, *Prof. Alam*, *Dhiraj*, *Jose* and *PP* again, without whom JNC would have been the most boring place for me. I would also like to mention *Harish*, *Ratul*, *Gayathri*, *Sourabh*, *Vinay*, *Divya*, *Mamta*, *Vybhav*, *Manjusha*, *Chakradhar*, *Kanwar*, *Shahjahan*, *Vikram*, *Deepak Rao*, *Vini*, *Vijay*, *Bharath*, *Charudatt* and *Juan*, all of whom have made my stay in JNC a memorable experience.

Oh, and just for the record, EMU 105 rules!

Abstract

We study the merger of three or more identical co-rotating vortices initially arranged on the vertices of a regular polygon, and compare it to the merger of two like-signed vortices. The latter is a well-studied problem, with the merger process there consisting of four stages. In the multiple (three or more) vortex case, we find a new stage in the merger process, where an annular vortical structure is formed and is long-lived. We find that merger on the whole is slowed down significantly as the number of vortices goes up, and the formation of the annular structure is primarily responsible for the delaying of the merger. In the three-vortex case, the vortices initially elongate radially, and then reorient their long axis closer to the azimuthal direction, and then diffuse out to form an annulus. The inviscid case is similar at short times, but at longer times, rather pronounced filaments are visible (in the three and four- vortex cases), which are practically absent in the viscous case. We find a qualitative change in the tilt history as we increase the number of vortices from three to six and more. In the six-vortex case, the vortices initially itself align themselves azimuthally. The annular stage is in contrast to the 'second diffusive stage' in two-vortex merger.

In addition to this, we find that at high Reynolds numbers, the vortices merge asymmetrically and the annulus even undergoes instabilities. In order to further understand the physics behind this, we perform a quasi-steady viscous linear stability analysis of an annular vortex. In other words, we study the cylindrical equivalent of a parallel shear flow in an infinite domain. Assuming azimuthal symmetry, we find a solution of the Navier-Stokes equation with the initial condition being that of an infinitesimally thin cylindrical vortex sheet. We obtain a Generalized Lamb-Oseen vortex profile, which we input as the mean flow for our stability analyses. We find that in the infinite Reynolds limit (inviscid case), there is an upper cut-off for the azimuthal modes going unstable. In general, we find that viscosity has a stabilizing effect, tending to preferentially stabilize the higher modes. We also find two modes going unstable for the azimuthal wavenumber two, till a low Re limit, where only one mode goes unstable.

List of Figures

Contents

Chapter 1

Introduction

1.1 Introduction

Vortices of the same sign in circulation tend to merge with each other. This thesis is a detailed study of the merger of several equal like-signed vortices placed initially with their centroids on the vertices of regular polygons.

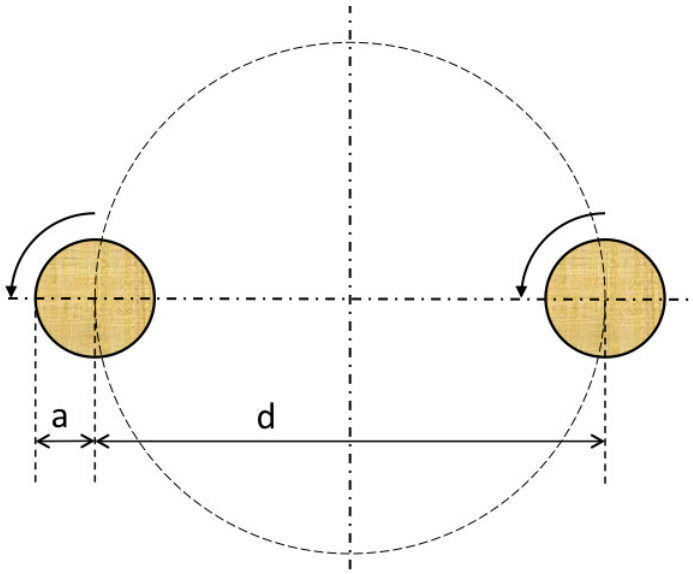

Figure 1.1: A schematic showing two equal co-rotating vortices, each having a circulation $\Gamma/2$, radius a and separated by a distance d. If $(a/d)_i < (a/d)_{crit}$, the vortices go around each other in a circle with a time period $T = 4\pi^2 d^2/\Gamma$. However, if $(a/d)_i \geq (a/d)_{crit}$, the vortices merge.

Consider first an inviscid system with two co-rotating point vortices each having a circulation $\Gamma/2$, and separated by a distance d. The motion of these vortices is governed by the Biot-Savart law, which confines the point vortices to motion on a circle of diameter d, with the azimuthal velocity of each vortex given by $u_\theta = \dfrac{\Gamma}{4\pi d}$. Next, if the point vortices are replaced by vortices of finite size (radius a) and finite uniform vorticity, we observe an interesting phenomenon. If the initial configuration is such that the ratio $(a/d)_i$ is less than a critical ratio $(a/d)_{crit}$, these vortices obey the point vortex dynamics described previously. However, if $(a/d)_i \geq (a/d)_{crit}$, the vortices while rotating around each other, deform and move towards each other. In a viscous flow they ultimately merge into a single larger vortex along with the formation of filaments of vorticity. This coalescence of vortices to form a single structure is called vortex merger. In the inviscid case, one has to keep in mind that the Kelvin's circulation theorem prevents the vortices from complete merger into a single structure. If $(a/d)_i < (a/d)_{crit}$, the behavior of these vortices is similar in the initial stages for the viscous and inviscid cases. However, the viscous vortices differ in that their cores grow in size (a increases) by diffusion, and at one particular stage,

(a) Merger. (b) Splitting.

Figure 1.2: A schematic of the two scenarios - Merger of multiple vortices to form an annulus, and splitting of an annulus into multiple vortices.

$(a/d)_{crit}$ is reached, when the vortices once again merge into a single core. The viscous case is thus different from the inviscid case in that the final merged structure is a gaussian vortex with a single vorticity maxima in addition to the filaments being smoothened out by viscosity.

Merger of two co-rotating vortices is one of the simplest and most important forms of interaction in the field of vortex dynamics, and is of both fundamental and practical significance. As a result, a considerable number of studies have been carried out over the last few decades to understand the physics governing vortex merger. One of the main reasons behind the increased attention and scrutiny is that vortex merger plays a key role in the decay of two-dimensional turbulence, wherein energy displays an inverse cascade, i.e. flows from smaller scales to larger ones. At the same time, the filaments ensuing from the merger process are believed to play a role in the enstrophy cascade from larger to small scales. A better understanding of the merger mechanism would also provide useful insight into the dynamics of coherent structures, which contain most of the kinetic energy in turbulent flows. The merger phenomenon is also a common occurrence in separating boundary layers (Freymuth 1966), mixing layers (Winant & Browand 1974) and high Reynolds number turbulent shear layers (Brown & Roshko 1974). On the other hand, merger and interaction of vortices find relevance in large-scale geophysical flows (Hopfinger & van Heijst 1993), especially in the formation and interaction of cyclones. Apart from this, vortex merger also finds engineering application in the context of aircraft trailing vortices and the hazards posed by them.

Most of the studies so far have concentrated on merger of two co-rotating vortices and not many have examined merger in the case of three or more vortices. In a turbulent flow dense with vorticity, it is not unusual for three or more vortices to interact simultaneously. Merger of multiple vortices could thus have an effect on the inverse energy cascade in two-dimensional turbulence. Multiple co-rotating point vortices of equal strength arranged at equal intervals on the circumference of a circle behave similar to the the two point vortex case in that they go around in a circle (time period $T = \frac{2n}{n-1}\frac{\pi^2 d^2}{\Gamma}$, where n is the number of vortices, Γ is the total circulation of all vortices put together, and d is the diameter of the circle), with the exception that they go unstable for eight or more vortices (Thomson 1883; Havelock 1932). In the case of vortices with finite size, non-linear inviscid studies (Dritschel 1986) so far have indicated that these vortices collapse into an annulus-like structure (Fig. 1.2a). On the other hand, some papers (Dritschel 1986) have carried out inviscid studies which find annular vortices to go unstable to azimuthal disturbances and split into smaller multiple vortices (Fig. 1.2b). In fact, multiple vortex phenomena have been observed in nature in cyclones and tornadoes. Cylindrical or

annular vortices can be viewed as the circular version of a plane parallel flow. Although the stability of parallel flows is well understood (Kelvin-Helmholtz Instability), the stability criteria and theorems are not directly applicable to rotating flows. There is a body of literature which addresses the stability of annular vortices (Michalke & Timme (1967), Rotunno (1978) to name a few), which are once again limited to inviscid studies. In the case of parallel flows, viscosity is capable of destabilizing rather than stabilizing the flow (higher order derivatives become important). Hence, there is a possibility of viscosity playing a non-intuitive role in the stability of rotating fluids too. It would be interesting to see how the merger of multiple vortices, and the instability of an annular vortex would be affected in the viscous context.

The thesis has been organized as follows. The rest of chapter 1 is dedicated to a literature survey for vortex merger, and for stability of an annular vortex. In chapter 2, we formulate the problem to study vortex merger. Here, we derive the vorticity streamfunction equations, and describe the Fourier pseudo-spectral technique used to solve the equations numerically. Chapter 2 also contains some relevant introduction to Fourier series and transform. In chapter 3, we validate the Fourier pseudo-spectral code, discuss the results from the vortex merger simulations in the case of multiple vortices, and finally conclude. In chapter 4, we obtain a solution (Generalized Lamb-Oseen vortex) of the Navier-Stokes equation, with the initial condition of an infinitesimally thin cylindrical vortex sheet. We also go on to validate the analytical expression with results from numerical simulations. Chapter 5 contains the formulation of the stability problem, wherein we derive the viscous and inviscid stability equations in cylindrical co-ordinates, and prescribe the boundary conditions. This chapter also contains a description of the Chebyshev collocation technique used to discretize the equations. In chapter 6, we validate the 2D and 3D viscous and inviscid stability codes, and go on to discuss the results from the 2D stability analysis of an annular vortex (Step, Tanh and Generalized Lamb-Oseen vorticity profiles). In chapter 7, we present our key findings and conclude the thesis.

1.2 Literature survey for vortex merger

One of the first studies on multiple vortices was carried out by Thomson (1883), where in, among other interesting problems, he investigated the stability of a system consisting of n equal straight cylindrical vortices (in other words, line vortices), arranged at equal intervals around the circumference of a circle. He showed analytically that six was the maximum number of vortices that can be arranged at equal intervals around the circumference of a circle, beyond which the system goes unstable. However, he arrived at this conclusion by treating each case of two, three, four, five, six and seven vortices individually, finding an instability in the last case. It was Havelock (1932) who generalized the result to n vortices, where in he found six and below to be stable, seven neutral and eight and above to go unstable. Apart from this, he also looked at the effects of inner and outer boundaries on such systems. Ever since, there has been a vast number of studies on the interaction of point vortices arranged in a multitude of configurations. Although point vortices in inviscid systems are ideal cases, they have been shown to capture most of the physics related to many problems in vortex dynamics, even those related to turbulence. This is mainly due to the fact that the interaction of point vortices is governed by the simple yet powerful Biot-Savart Law, which is a nonlinear relation.

The next step was then to look at interaction of vortices with finite areas or sizes. With the help of vortex methods for inviscid flows, Roberts & Christiansen (1972) observed the merger of two uniform vortex patches for certain critical ratios ($a/d > 0.29$) between the vortex core radius (a) and the initial vortex separation distance (d). Rossow (1977) performed similar inviscid numerical studies to study merger in the context of vortical structures in the wake of an aircraft. Here, he attempted to find the conditions for which the vortices would merge to form a dispersed wake, which is less hazardous. In his computations, he found $a/d > 0.26 - 0.30$ for convective merger. Zabusky *et al.* (1979) then introduced the concept of contour dynamics for the inviscid Euler equations, wherein the velocity at any point in the flow depends only on the boundary of the closed contours encircling the regions of uniform vorticity. Using this technique, Deem & Zabusky (1978), Saffman & Szeto (1980), Overman & Zabusky (1982) and Dritschel (1985) were able to find steady configurations of non-circular co-rotating patches (also referred to as V-States by some of them) for $a/d < 0.32$. Overman & Zabusky (1982) also analyzed the perturbed rotating V-States and found that for $a/d > 0.32$, the co-rotating vortices approached each other at an exponential rate and merged to reform into a single stable elliptical structure with filaments. They attribute the cause of merger to an instability of the perturbed V-States and hint that filaments are formed in order to conserve angular momentum. Dritschel (1985) extended these results to configurations of multiple vortices (two and above) rotating about a common center, and with the help of a linear stability analysis, found that the vortices may destabilize via a new form of instability derived from boundary perturbations, which are distinct from the displacement type instability occurring in the point vortex case previously discussed. In his analysis, he assumed the equilibrium configurations to be symmetric about the line joining the center of rotation to the centroid of the vortex. He also utilized the fact that the uniform vortex boundary is a streamline in the rotating frame, or that the local velocity is tangent to the boundary in the rotating frame. Using the same assumptions, Cerretelli & Williamson (2003*a*) were able to find a new family of uniform vortices prior to the merger process in the two-vortex case. Among this is an equilibrium configuration in which the vortices touch each other to form a dumb-bell. However, it must be noted that the assumptions made regarding the symmetry of the equilibrium configurations may make them impossible to achieve in reality. In a real merger process, the major axis of the vortex tilts from the line joining the center of rotation to the vortex centroids. Another point to note is that the studies mentioned so far have only looked at vortices with uniform vorticity, whereas, as we know it, real vortices have non-uniform or distributed vorticity.

Recently, there has been a lot of work on merger of vortices that have distributed vorticity. Ehrenstein & Rossi (1999) introduced a numerical method to find inviscid equilibrium solutions for co-rotating vortices with non-uniform vorticity profiles, based on computing perturbed streamlines using Green's function integrals. Meunier *et al.* (2002) adopted this technique to find similar equilibrium solutions for distributed vorticity profiles, and in doing so, deduce a merger criterion based on a new core radius which they term as the characteristic vorticity radius a_ω defined by $a_\omega = \sqrt{J/\Gamma}$, where J is the angular impulse or the second moment of vorticity and Γ is circulation or the zeroth moment of vorticity of each vortex. They computed the critical ratio based on this new vorticity radius and found $a_\omega/d \approx 0.22$, which matched reasonably well

with experimental values for a gaussian vorticity profile. They also argued that their critical core size showed much lesser variations for a variety of vorticity distributions than previously used definitions (the most common one being $a = \sqrt{Area/\pi}$).

Most of the papers mentioned so far have only looked at the conditions for the onset of merger, and haven't addressed the physical mechanism underlying the merger phenomenon. One of the first steps towards understanding the physical mechanism were taken by Melander *et al.* (1987). Employing a co-rotating reference frame, they studied the axisymmetrization of an isolated ellipse of uniform vorticity. They observe that filaments are formed, which are initially placed inside a region they call as the 'ghost vortex' outside the inner vortex core. They find that as a consequence of the co-rotating reference frame, this 'ghost vortex' region has a sense of rotation opposite to that of the inner core, thus advecting the vorticity away from the inner core. They argue that the filaments, although a small fraction of the total, breaks the elliptical symmetry and is the primary cause of the axisymmetrization. In essence, they observe a tilt in the vorticity contours with respect to the elliptical streamlines, which then leads to the formation of filaments. They find that this axisymmetrization is an inviscid mechanism acting on a circulation time scale, whose net effect is to reduce the aspect ratio of the ellipse. Melander *et al.* (1988) looked at the physical mechanism for the merger of two co-rotating vortices and proposed that it is the same axisymmetrization mechanism seen in the case of an ellipse, that is responsible for the reduction in aspect ratio (reduction in separation distance) of the two-vortex system. Essentially, it is the tilt in the vorticity contours with respect to the co-rotating frame streamlines which causes the merger. However, they came short of determining the exact reason for this tilt. At the same time they recognized two possible stages in merger : the 'viscous metastable state' proceeding on a dissipation time scale, and the 'convective merger state', where merger happens on a circulation timescale.

Following this, there have been many works that have attempted to study the physical mechanism behind the merger phenomenon. In addition to this, viscous effects have also been considered in the merger studies. With the help of experiments and simulations, Meunier & Leweke (2001), Meunier & Leweke (2005) and Meunier *et al.* (2005) have been able to observe three different stages in the entire merger process, where in, apart from the first two stages described by Melander *et al.* (1988), they define a third stage which happens to be the diffusion of the merged vortex. Their main finding however is a new cooperative elliptic instability for $Re > 2000$ ($Re = \Gamma/\nu$ where Γ is circulation and ν is kinematic viscosity), where the co-rotating vortices are three-dimensionally unstable, with a distinct phase relationship for the instabilities in each vortex. They find an excellent agreement between experiments, theory and computations, for the spatial structure, wavelength and growth rates of this instability. They also find that these three-dimensional effects, in the form an elliptic short-wave instability cause significant changes in the merging process, such as earlier merging and larger final vortex cores. Apart from this, Meunier *et al.* (2005) also propose a mechanism for merger based on the conservation of angular momentum. They argue that the formation of filaments increases the angular momentum of the system, and in order for this to be conserved, the vortices move closer to each other.

With the help of numerical simulations, Lé Dizès & Verga (2002) have studied the viscous

interactions between two co-rotating vortices before the onset of merger. They vary the steepness of the vorticity profile and the Reynolds number, and are able to identify two distinct relaxation processes. The first one, which is an inviscid phenomenon, is a rapid adaptation of each vortex to the strain field generated by the other vortex, and results from the fact that the initial condition is not a solution of the Navier-Stokes equation. They find this process to be profile dependent and have quantified it by measuring the eccentricity of the vortex core, which relaxes to a non-zero value in an oscillating fashion. They then relate this oscillating behavior to the damped linear (Kelvin) mode of each vortex. The second relaxation process is a slow viscous diffusion phenomenon similar to the evolution of any non-Gaussian axisymmetrical vortex towards the Gaussian. Apart from this, they also obtain a $Re^{1/3}$ scaling for the vorticity at the central hyperbolic point in the range of $500 < Re < 8000$. However, the peak of vorticity is bounded by its initial value, and hence, for a given (a/d), this scaling would break down for sufficiently large Reynolds numbers.

Cerretelli & Williamson (2003*b*) were the next to address the mechanism responsible for the vortex merger of two co-rotating vortices. Here, they propose that it is the antisymmetric vorticity field (primarily associated with filaments) which causes the reduction in separation distance between two vortices. With the help of experiments, they directly measure the structure of the antisymmetric vorticity field, which comprises of two counter-rotating vortex pairs and find a close agreement between the merging velocity induced by the antisymmetric field and that measured due to the total flow field. They also propose four stages in the merger process with an additional second diffusive stage immediately following the convective stage. Towards the end of the convective merging stage, they find that the antisymmetric vorticity is diminished by a symmetrization process. Here there is an increase in size of the separatrix (in the co-rotating frame) bounding the inner region of the flow, which recaptures some of the vorticity which originally escaped to become asymmetric vortex filaments. During this period, the induced velocity pushing vortex centroids together becomes too weak to cause the final merger into one structure. The final merging into one vorticity structure is achieved by a second diffusive stage which shifts the vortex maxima together form a single vortex.

Velasco Fuentes (2005) however, finds that filamentation does not always lead to merger and in the case of steep vorticity profiles, merger begins before filamentation takes place. He points out a weakness in the approach taken by others, who used an Eulerian geometry in the co-rotating frame (where the flow appears to be stationary) to explain the formation of filaments with the help of separatrices. Since merger is an unsteady phenomenon, such a system does not exist. Instead, by analyzing the Lagrangian flow geometry using a dynamical systems approach, he finds that filamentation occurs when the stable manifold of a hyperbolic trajectory enters the vortex. In effect, he recognizes the importance of filamentation in merger, but does not find it to be responsible for the onset of vortex merger. Huang (2005) too analyzes the flow in terms of Lagrangian flow structures, and shows that a "sheet-like structure" emanating from the opposite vortex, which includes both filament and exchange band fluid (defined by Melander *et al.* (1988) as the band immediately surrounding the inner vortex cores), is responsible for the induced merging velocity. So far, we have described papers where in it has been established that the primary reason for merger is the antisymmetric vorticity caused by tilt in the vorticity

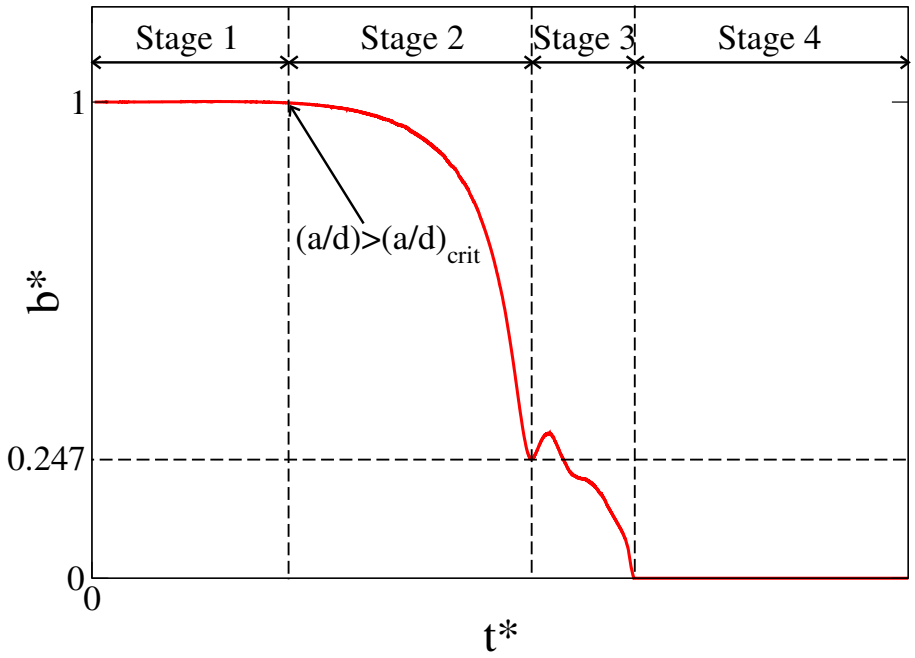

Figure 1.3: Non-dimensional separation distance b^* vs non-dimensional time t^* indicating the two-vortex merger as a four stage process.

contours with respect to the line joining the vortex centers. However, the exact reason for this tilt had not been explained.

Brandt & Nomura (2006) determine the relative contributions of filament and exchange band fluid to the reduction in the separation distance, and find the latter to be dominant. First, the inner circulation (cores and exchange band) and outer recirculation filaments regions are distinguished by the sign of vorticity ω (outer recirculation is associated with differential rotation) in the co-rotating frame. Next, the cores and exchange band are distinguished by considering the second invariant of the velocity gradient tensor in the co-rotating frame, $\Pi = \left(\omega^2 - S^2\right)/2$, where S is the strain rate tensor.Therefore, $\Pi > 0$ represents rotation-dominated regions, which effectively characterizes the cores, and $\Pi < 0$ represents strain-dominated regions, which characterizes the exchange band. They then calcualte the velocity induced by these regions using the Biot-Savart law, and find the exchange band to be the main contributor (although filaments also contribute). One of the main findings in their paper is reason for the tilt in vorticity contours, which they attribute to the interaction of strain rate and vorticity gradient near the center of rotation. This then leads to the entrainment of core fluid into the exchange band and the formation of filaments.

We now paint the overall picture of the symmetric vortex merger of two co-rotating vortices in a homogeneous fluid having an core radius a and centers initially separated by a distance d. The entire merger process can be divided into four stages as described by Cerretelli & Williamson (2003*b*) (Fig. 1.3, also see Figs. 3.4 and 3.6 from chapter 3).

The first stage is a diffusive stage, acting on a diffusive time scale, and is present if the initial $(a/d) < (a/d)_{crit}$. Here the vortices grow in size by viscous diffusion, while they rotate around each other in a circle with a constant separation distance (similar to behavior of two point vortices). Apart from this, the strain field of the two-vortex system causes the vortices

to deform and align themselves radially. Towards the end of this stage, as the vortices grow in size, they also begin to develop a slight tilt to the line joining their centers. This is once again caused by the strain field of the vortices.

The second (convective) stage is the key stage in the merger process, where most of the reduction in separation distance happens. At the end of the first stage, the (a/d) reaches a critical $(a/d)_{crit}$ (this critical ratio depends on the vorticity profile) when the deformation and the tilt is prominent enough to causes the vorticity to enter the exchange band fluid. At this point the vorticity gets entrained into the exchange band and the outer recirculation region (partly through diffusion), leading to the formation of an antisymmetric vorticity field. Here, the differential rotation of the outer recirculation region causes the formation of filaments. This antisymmetric vorticity field, consisting of exchange band fluid and filaments, in turn induces a velocity which pushes the vortices closer towards each other (the exchange band is found to be the dominant contributor in the two-vortex case). Towards the end of this stage, the antisymmetric vorticity is diminished by a symmetrization process (discussed earlier), and hence is no longer able to push the vortices together. Also, the second (convective) stage, which corresponds to the motion of the vortex centroids towards each other, is a process which is almost independent of viscosity, thus proceeding on a convective time scale. One should note that in the inviscid case, the entire merger comprises of only one convective stage.

The third stage, also known as the 'second diffusive stage', is one where in the vortex maxima are shifted together by viscous diffusion. Although few papers have looked at the Re scaling in this stage, not much attention has been devoted to this stage so far and is still not very well understood.

The fourth and final stage in the merger process involves axisymmetrization and growth of the merged vortex by viscous diffusion. This is also accompanied by the smoothening out of the filaments by viscosity.

Apart from the various works described above on symmetric merger of two co-rotating vortices in homogeneous fluids, there are also many papers which have looked at asymmetric merger and also considered the effects of rotation, stratification, etc. However, not many have studied the merger of multiple vortices (> 2). One paper worth mentioning though is Dritschel (1986), wherein, as a continuation of the linear analysis performed in the previously mentioned Dritschel (1985), he goes on to study the nonlinear evolution of perturbed rotating equilibrium configurations of N uniform vorticity patches. Viewing merger as an instability, he finds nonlinear stability whenever the configurations are linearly stable. In the case of linearly unstable equilibria, he finds that large-m (m is the azimuthal mode) symmetric neutral disturbances are the only ones that resist instability. The other disturbances eventually cause the collapse of the vortices into a central annular region surrounded by substantial streamers of vorticity except for the clean merger of two vortices into a near 6:1 ellipse. He attributed this to the close proximity of two vortices to the ellipse on the energy diagram. He also finds that three and four vortices do not merge cleanly, and believes this to be a consequence of their energy curves being distant from the energy curves of other equilibria of compatible symmetry. These studies are however limited to inviscid analyses and uniform vorticity patches.

1.3 Literature survey for stability of annular vortex

The first studies on the stability of cylindrical vortices were in the context of flow between concentric cylinders. Here, for zero axial flow, Rayleigh (1880) found a necessary condition for instability of swirling flows, that the vorticity shouldn't be a monotonically varying function of the radius r. In other words, the vorticity must have an extremum value inside the flow region for an instability to occur. This condition for instability is equivalent to Rayleigh's inflection point criterion for parallel flows. The inviscid stability problem for axisymmetric disturbances in the case of zero axial flow was then investigated by Rayleigh (1917), wherein he showed that a necessary and sufficient condition for stability is that the square of the circulation, $(rV)^2$ (V being the swirl velocity), should nowhere decrease as the radius r increases. As Rayleigh suggested, this problem has a strong analogy with the stability of a density-stratified fluid at rest, under the action of gravity. Restricting the analysis to axisymmetric perturbations, one may ignore the rotation and think of the fluid as being subject to a radially outward 'gravitational field', and having a 'density' which is determined by the distribution of swirl velocity V(r). In this interpretation, Rayleigh's criterion is simply the condition that for stability, the 'density' should not decrease 'downward', i.e. outward. Here, the kinetic energy associated with the swirl velocity is analogous to the 'potential energy of gravity '.

Chandrasekhar (1961)[§78b] went one step further by considering the stability of inviscid flows with both axial and swirl components of velocity, and concluded that stability is determined by Rayleigh's criterion alone (based on swirl component), without any dependence on the axial component. However, Howard & Gupta (1962) believed this result to be physically implausible and incorrect. They argued that the swirl component has a stabilizing influence if Rayleigh's criterion is satisfied and is capable of producing complete stability, but only if it is sufficiently strong in comparison to the shear in the axial component. In fact, they picked up a hint from Rayleigh's analogy between swirling flows and density stratified fluids, and found that in the presence of an axial flow, the effect of swirl component is analogous to the effect of density stratification (in the presence of gravity) on a parallel shear flow. Just like in the stratified parallel shear flow wherein a statically stable density stratification can have a stabilizing influence on the axial shear (the stability being governed by the Richardson number, with complete stability insured if local Richardson exceeds 1/4), they have defined an analogous Richardson number and a sufficient condition for stability ($Ri > 1/4$). Here, $Ri = \Phi/W'^2$, where base flow is given by $U = V(r)\,\hat{\theta} + W(r)\,\hat{k}$, and $\Phi = r^{-3}d/dr\left[r^2V^2\right]$. They proceed to show that the complex wave speed for any unstable mode must lie in a certain semicircle, a result also known for stratified parallel shear flow. Their result however, is once again applicable only to axisymmetric perturbations. Although they tried their hand at non-axisymmetric perturbations, they failed to reach any concrete conclusions beyond the already known Rayleigh Criterion.

Michalke & Timme (1967) then investigated the stability of a two-dimensional cylindrical vortex in the context of the breakdown phenomenon of vortices observed in the two-dimensional free boundary layer. With the help of linear inviscid stability theory of rotating fluids, they first looked at the stability of an infinitely thin cylindrical vortex sheet (cylindrical equivalent of a planar vortex sheet), and found it to go unstable for non-axisymmetric perturbations ($m \geq 1$, where m is the azimuthal wave number and integer valued for physical reasons), although

Rayleigh's criterion predicted stability. Thus, they showed that Rayleigh's criterion is applicable only to axisymmetric disturbances. Next, they studied the stability of a cylindrical vortex of finite thickness (they first considered a step vorticity profile), and found stability for $m = 1$ and $m = 2$ disturbances, with $m \geq 3$ going unstable. Also, they found that the finite thickness placed an upper cut off for m beyond which the flow is once again stable (thinner the cylindrical vortex, higher the cut off m, which is expected). For $m = 1$ and 2, there was an inconsistency in the limit of thickness $a \to 0$, their result didn't match with that of the infinitely thin cylindrical vortex sheet. Apart from this, they also looked at a continuous vorticity profile for which the Rayleigh criterion predicted stability and found similar results to that of the step profile (note that unlike the result for the step profile, they found $m = 2$ disturbance to be now unstable). In addition to this, they also found two-dimensional disturbances to be more unstable than the corresponding three dimensional ones for the cylindrical vortex sheet as well as the continuous vorticity profile, similar to a result well-known for parallel shear flows.

Rotunno (1978) revisited the problem of inviscid stability of an infinitely thin cylindrical vortex and corrected the inconsistency in Michalke & Timme (1967), in which the stability of $m = 1$ and $m = 2$ modes were uncertain. In fact, he found the $m = 1$ and 2 disturbances to be stable, and the rest of the modes from then on to be unstable. In other words, except the $m = 1$ and 2 modes, the results are analogous to those for the stability of plane parallel flows (where in all wavelengths are unstable, the smallest waves growing most rapidly). Motivated by the occurrence of multiple vortices, especially in the context of tornadoes, where a single tornado splits into two smaller ones, he went on to further investigate stability of the cylindrical vortex sheet by considering a central downdraft surrounded by a uniform updraft, and found the $m = 1$ and 2 modes to be destabilized in the presence of a non-zero vertical wavenumber k. He was able to support his result by the fact that double vortices have been observed in nature (tornadoes) as intertwining spirals i.e they have a vertical structure.

Leibovich & Stewartson (1983) considered the inviscid instability of columnar vortex flows in unbounded domains to three-dimensional perturbations, and formulated a sufficient condition for the instability of columnar vortices as

$$V\frac{d\Omega}{dr}\left[\frac{d\Omega}{dr}\frac{d\Gamma}{dr}+\left(\frac{dW}{dr}\right)^2\right]<0\ , \tag{1.1}$$

where $V(r)$ is the swirl velocity, $W(r)$ is the axial velocity, $\Omega = V/r$ is the angular velocity and $\Gamma = rV$ is the circulation. In the large m limit, they were able to develop the solution in an asymptotic expansion, which they then compared with numerical solutions for the case of a trailing vortex, finding a reasonable match for the most unstable wave (for values of m as low as 3, with accuracy increasing with increasing m). However, their theory is applicable only in the large m limit, and there is also no guarantee that the maximum growth rate should occur in that limit.

The papers mentioned so far have studied inviscid instability in case of vortices with one sign only (finite circulation). Gent & McWilliams (1986) studied the linear, normal mode instability of barotropic circular vortices with zero circulation (vorticity changes sign) in the f-plane quasi-geostrophic equations. They argued that mean flows with finite circulation are less

relevant physically because they decay very slowly with increasing radius and have unbounded kinetic energy in an infinite domain. In contrast, mean flows with zero circulation decay much quicker with radius and have finite kinetic energy, so that they can be considered as isolated structures. A new finding of theirs is that the fastest growing perturbation is often three-dimensional, having a finite vertical scale, but may also be two-dimensional, having no vertical structure (which is in contrast to the result for parallel shear flows, where the fastest growing perturbation is always an external instability, as predicted by the the Squire's theorem). This they found was dependent on the steepness of the streamfunction profiles (they worked with the vorticity streamfunction formulation), with instability being internal for less steep profiles and external for more steep streamfunction profiles. However, their condition was not a strict proof of the type of instability but just a guide identified by posteriori categorization of particular streamfunction profiles studied. Flierl (1988) then investigated the instabilities of barotropic and baroclinic, quasi-geostrophic, f-plane, circular vortices using a linearized contour dynamics model. He modeled the vortex using a circular region of horizontally uniform potential vorticity surrounded by an annulus of uniform, but different, potential vorticity. A key finding in his work is that in the case barotropic perturbations (two-dimensional), the $m = 2$ elliptic mode grows only when there is a change in the sign of vorticity (opposite sign vorticity for inner and outer cores) and the right thickness of annular region. This was not discovered by Michalke & Timme (1967) as they limited themselves to vorticity of one sign only. In the case of baroclinic perturbations (three-dimensional), the $m = 2$ elliptic mode was found to go unstable for the single signed vorticity case itself. Apart from this, he also found the barotropic eddy to become unstable in previously stable regimes to the $m = 1$ perturbations for the case with vortices of opposite signs in inner core and annular regions. In one of the more recent works, Terwey & Montgomery (2002) derived a necessary and sufficient criterion for $m = 2$ mode instability by considering a piecewise uniform three region vortex model, and confirmed the result obtained by Flierl (1988), which requires a change in sign of vorticity between the inner core and outer annulus in addition to an appropriate annulus thickness.

Using contour dynamics, Dritschel (1986) examined the behavior of small perturbations to an annular region of vorticity in an inviscid system. Here, he added finite-amplitude eigenmodes from the linear stability analysis to the annulus, and integrated the system in time for a variety of basic-states and disturbances. He determined that a linearly stable annular vortex is stable to sufficiently small disturbances. If the basic state is linearly unstable to both even and odd disturbances, only neutral eigenmodes with $m \neq 2$ are stable; also $m = 2$ can generate the $m = 4$ unstable eigenmode via wave-wave interactions (the reverse is not true). For thicker annuli in which only $m = 3$ is unstable, it takes a disturbance with a 3-fold component to cause instability. Linearly marginal, unstable and stable disturbances always lead to nonlinear instability. As for the character of the evolution, nonlinearly unstable disturbances tend to break apart the ring of vorticity. Of course, the ring does not completely break into multiple vortices (by Kelvin's circulation theorem in inviscid systems), but just forms distinct centers of vorticity. With the help of a pseudo-spectral algorithm solving the barotropic non-divergent vorticity model, Schubert *et al.* (1999) found a ring of elevated vorticity perturbed with azimuthally broad-banded initial conditions to go unstable and form multiple vortices, which undergo further rearrangement

to a near monopolar circular vortex. Thus there have been some studies confirming that multiple vortex phenomena observed in nature are strongly related to instabilities of annular vortices.

Apart from this, there are quite a few papers which study the instabilities in the context of hurricanes and tornadoes. They incorporate many more effects and are far more complicated, and although they are able to capture multiple vortex phenomena, they do not isolate the exact physics behind the phenomenon of multiple vortex merger. In addition to this, most of the studies so far have mainly looked at the stability of piecewise constant vorticity profiles which are not solutions to the Navier-Stokes equations. Another point to note is that none of them have performed a viscous linear stability analysis of an annular vortex. As observed in plane parallel flows, viscous effects can lead to an instability. In fact, this has already been observed in studies of trailing vortices.

Chapter 2

Vortex Merger: Problem formulation and numerical technique

2.1 Scope

In this chapter, we will first formulate the problem to study the merger of vortices. We numerically solve the vorticity equation for which we use a pseudo-spectral (Fourier bases) technique for spatial discretization and an explicit Runge-Kutta fourth order technique for temporal discretization. The chapter also contains some relevant introduction to Fourier series and transform.

2.2 Formulation and numerical technique

We first derive the equation governing the vorticity with viscous effects in a fixed frame of reference, assuming that the flow is barotropic (fluid density is constant). To begin with, we write down the set of continuity and Navier-Stokes equations in vector form in the cartesian co-ordinate system :

$$\nabla \cdot \mathbf{u} = 0 \ , \tag{2.1}$$

$$\frac{D\mathbf{u}}{Dt} = -\frac{1}{\rho}\nabla p + \nabla \Pi + \nu \nabla^2 \mathbf{u} \ , \tag{2.2}$$

where

$$\nabla = \frac{\partial}{\partial x}\hat{i} + \frac{\partial}{\partial y}\hat{j} + \frac{\partial}{\partial z}\hat{k}, \quad \nabla^2 = \frac{\partial^2}{\partial x^2} + \frac{\partial^2}{\partial y^2} + \frac{\partial^2}{\partial z^2}, \quad \frac{D}{Dt} = \frac{\partial}{\partial t} + \mathbf{u} \cdot \nabla \ , \tag{2.3}$$

In the above expressions, $\frac{D}{Dt}$ is the material derivative, $\mathbf{u}$ is the velocity field, p is pressure, ρ is density, ν is the absolute viscosity and Π is the body force potential.
Vorticity $\boldsymbol{\omega}$ is defined as

$$\boldsymbol{\omega} = \nabla \times \mathbf{u} \ . \tag{2.4}$$

Taking curl of Eq. 2.1 and noting that the curl of divergence vanishes, we get

$$\nabla \cdot \boldsymbol{\omega} = 0 \ , \tag{2.5}$$

Taking curl of Eq. 2.2, and using the identity

$$\mathbf{u} \cdot \nabla \mathbf{u} = (\nabla \times \mathbf{u}) \times \mathbf{u} + \frac{1}{2}\nabla (\mathbf{u} \cdot \mathbf{u}) = \boldsymbol{\omega} \times \mathbf{u} + \frac{1}{2}\nabla q^2 \ , \tag{2.6}$$

and noting that the curl of a divergence vanishes, we get

$$\frac{\partial \boldsymbol{\omega}}{\partial t} + \nabla \times (\boldsymbol{\omega} \times \mathbf{u}) = \nu \nabla^2 \boldsymbol{\omega} \ . \tag{2.7}$$

We can rewrite the second term in Eq. 2.7 with the help of Eqs. 2.1 and 2.5 as

$$\nabla \times (\boldsymbol{\omega} \times \mathbf{u}) = (\mathbf{u} \cdot \nabla)\, \boldsymbol{\omega} - (\boldsymbol{\omega} \cdot \nabla)\, \mathbf{u} \ , \tag{2.8}$$

and finally we are left with

$$\frac{D\boldsymbol{\omega}}{Dt} = (\boldsymbol{\omega} \cdot \nabla)\, \mathbf{u} + \nu \nabla^2 \boldsymbol{\omega} \ . \tag{2.9}$$

The term $(\boldsymbol{\omega} \cdot \nabla)\, \mathbf{u}$ represents the rate of change of vorticity due to stretching and tilting of vortex lines. We assume that the flow is two-dimensional. In other words, there is no variation of u_x and u_y velocities and other quantities with z and $u_z = 0$. The stretching and tilting term $(\boldsymbol{\omega} \cdot \nabla)\, \mathbf{u}$ vanishes under this assumption and we are left with

$$\frac{D\boldsymbol{\omega}}{Dt} = \nu \nabla^2 \boldsymbol{\omega} \ . \tag{2.10}$$

We can also write velocity in terms of a scalar streamfunction ψ.

$$\mathbf{u} = -\hat{k} \times \nabla \psi, \quad \mathbf{u} = u_x \hat{i} + u_y \hat{j} \ , \tag{2.11}$$

or

$$u = \frac{\partial \psi}{\partial y}, \quad v = -\frac{\partial \psi}{\partial x} \ . \tag{2.12}$$

Substituting Eq. 2.12 in Eq. 2.4, we get

$$\nabla^2 \psi = -\omega, \quad \nabla^2 = \frac{\partial^2}{\partial x^2} + \frac{\partial^2}{\partial y^2} \tag{2.13}$$

where ω is the vertical component of vorticity, perpendicular to the plane of the flow.
We are finally left with the following coupled system of equations, which will be referred to as the vorticity-streamfunction equations.

$$\left(\frac{\partial}{\partial t} + \frac{\partial \psi}{\partial y}\frac{\partial \omega}{\partial x} - \frac{\partial \psi}{\partial x}\frac{\partial \omega}{\partial y} \right) \omega = \nu \nabla^2 \omega \ , \tag{2.14}$$

$$\nabla^2 \psi = -\omega \ . \tag{2.15}$$

We numerically solve this system by adopting a pseudo-spectral (Fourier) technique for spatial discretization and an explicit Runge-Kutta fourth order technique for temporal discretization.

2.3 Spatial discretization : Pseudo-spectral

Now, we look at some of the important concepts and formulae related to the Fourier pseudo-spectral technique. In this entire section, we explain the concepts in only one dimension. The generalization to more than one dimension is straight forward. We start off with the continuous Fourier expansion :
The Fourier coefficients of a complex-valued function u defined on $(0, 2\pi)$ can be written as

$$\hat{u}_k = \frac{1}{2\pi} \int_0^{2\pi} u(x)\, e^{-ikx}\, dx, \quad k = 0, \pm 1, \pm 2, \dots \ . \tag{2.16}$$

The orthogonality relation for the set of Fourier basis functions $\phi_k(x) = e^{ikx}$ over the interval $(0, 2\pi)$ is given by

$$\int_0^{2\pi} \phi_k(x)\, \overline{\phi_l(x)}\, dx = 2\pi\delta_{kl} = \begin{cases} 0 & \text{if } k \neq l\ , \\ 2\pi & \text{if } k = l\ . \end{cases} \tag{2.17}$$

The Fourier series Su and the truncated Fourier series $P_N u$ can be written as

$$Su = \sum_{k=-\infty}^{k=\infty} \hat{u}_k \phi_k, \qquad P_N u(x) = \sum_{k=N/2}^{N/2-1} \hat{u}_k e^{ikx}, \quad \text{as } N \to \infty\ . \tag{2.18}$$

The error between u and the truncated expression is termed as the truncation error. Given that u is continuous, periodic and bounded on $[0, 2\pi]$, the Fourier series Su is uniformly convergent to u and we can write

$$u = \sum_{k=-\infty}^{k=\infty} \hat{u}_k \phi_k\ . \tag{2.19}$$

The Fourier coefficients related to the Fourier cosine and Fourier sine transform of u can be written as

$$\hat{a}_k = \frac{1}{2\pi} \int_0^{2\pi} u(x) \cos kx\, dx, \quad k = 0, \pm 1, \pm 2, \dots \tag{2.20}$$

and

$$\hat{b}_k = \frac{1}{2\pi} \int_0^{2\pi} u(x) \sin kx\, dx, \quad k = 0, \pm 1, \pm 2, \dots \ . \tag{2.21}$$

From Eqs. 2.16, 2.20 and 2.21, we get

$$\hat{u}_k = \hat{a}_k - i\hat{b}_k\ . \tag{2.22}$$

When u is real, $\hat{a}_k$ and $\hat{b}_k$ are real, and $\hat{u}_{-k} = \overline{\hat{u}_k}$.

Although the standard Fourier treatment looks elegant, there are many practical difficulties associated with its application. For example, the Fourier coefficients need not be known in a

closed form. Also, simple non-linearities can lead to complications. Hence, we use Discrete Fourier expansions to overcome these difficulties :
For an integer $N > 0$, consider the even set of points for collocation

$$x_j = \frac{2\pi j}{N}, \quad j = 0, 1, \ldots, N-1 \ . \tag{2.23}$$

The discrete Fourier coefficients of a complex-valued function u in $[0, 2\pi]$ with respect to these points are

$$\tilde{u}_k = \frac{1}{N} \sum_{j=0}^{N-1} u\left(x_j\right) e^{-ikx_j}, \quad k = -N/2, \ldots, N/2-1 \ . \tag{2.24}$$

The orthogonality relation is

$$\frac{1}{N} \sum_{j=0}^{N-1} e^{-ipx_j} = \begin{cases} 1 & \text{if } p = Nm, \ m = 0, \pm 1, \pm 2, \ldots \ , \\ 0 & \text{otherwise} \ . \end{cases} \tag{2.25}$$

Thus, we can write

$$u\left(x_j\right) = \sum_{k=-N/2}^{N/2-1} \tilde{u}_k e^{ikx_j}, \quad j = 0, \ldots, N-1 \ . \tag{2.26}$$

2.3.1 Differentiation

The techniques involved in differentiation in spectral methods depends upon whether one is working in the transform space or in the physical space. Here, we discuss only the method involved in differentiation in transform space due to its simplicity. To calculate the derivative in the physical space, one has to simply transform into the Fourier space, multiply each Fourier coefficient by an imaginary number, and finally transform back to physical space. If the Fourier series of a function u is given by

$$u = \sum_{k=-\infty}^{k=\infty} \hat{u}_k \phi_k \ , \tag{2.27}$$

then the Fourier derivative of u is given by

$$u' = \sum_{k=-\infty}^{\infty} ik\hat{u}_k \phi_k \ . \tag{2.28}$$

In the discrete form, called the Fourier interpolation derivative $\mathcal{D}_N u$ at the grid points x_j (based on even number of points according to Eq. 2.23) are given by,

$$\left(\mathcal{D}_N u\right)_j = \sum_{k=-N/2}^{N/2-1} \tilde{u}_k^{(1)} e^{2ikj\pi/N}, \quad j = 0, 1, \ldots, N-1 \ , \tag{2.29}$$

where

$$\tilde{u}_k^{(1)} = ik\tilde{u}_k = \frac{ik}{N}\sum_{l=0}^{N-1} u\left(x_l\right) e^{-2ikl\pi/N}, \quad k = -N/2, \ldots, N/2-1 \ . \tag{2.30}$$

2.3.2 Aliasing

The discrete Fourier coefficients can be expressed in terms of the exact Fourier coefficients of u given that the exact Fourier series converges at the nodal points given in Eq. 2.23 as

$$\tilde{u}_k = \hat{u}_k + \sum_{\substack{m=-\infty \\ m\neq 0}}^{\infty} \hat{u}_{k+Nm}, \quad k = -N/2, \ldots, N/2-1 \ . \tag{2.31}$$

This shows that the k-th mode of the interpolant of u depends on the k-th mode as well as all the modes of u that alias the k-th mode on the grid. The $(k+Nm)$-th wavenumber aliases the k-th wavenumber on the grid since $\phi_{k+Nm}\left(x_j\right) = \phi_k\left(x_j\right)$, making them indistinguishable at the nodes. Fig. 2.1 illustrates this phenomenon, wherein three sine waves with frequencies $k = 10$, 2 and -6 are superimposed with nine grid-point values of the function. It is evident that by using a course grid, both $k = 10$ and $k = -6$ waves are misinterpreted as a $k = 2$ wave. This phenomenon is called aliasing and is responsible for the aliasing error between the interpolated polynomial and the truncated Fourier series.

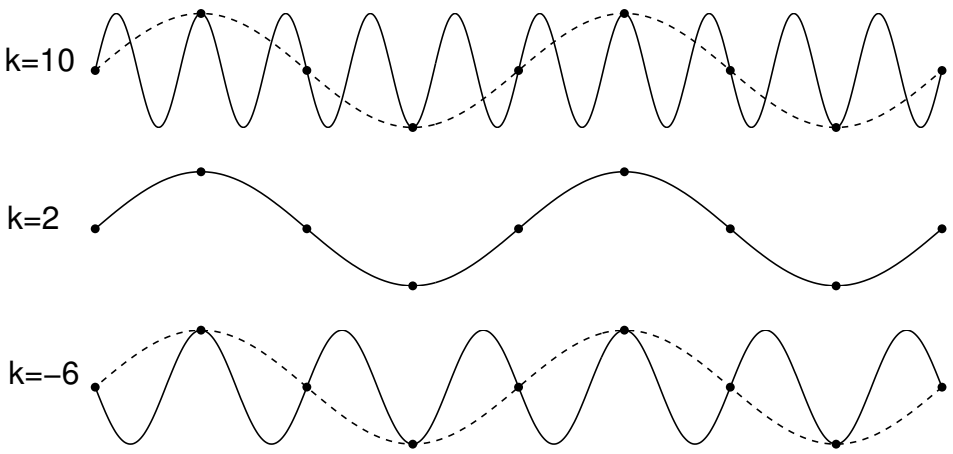

Figure 2.1: Three sine waves having the same $k = 2$ interpretation on a nine-point grid. The filled circles denote the nodes, and the solid curves denote the actual sine waves. By using a course grid, both $k = 10$ and $k = -6$ waves are misinterpreted as a $k = 2$ wave (dashed curve).

2.3.3 Convolution sum, the pseudo-spectral method and aliasing associated with it

Consider the following product

$$c(x) = u(x)\, v(x) \ . \tag{2.32}$$

Writing the infinite series expansion

$$\hat{c}_k = \sum_{m+n=k} \hat{u}_m \hat{v}_n \ , \tag{2.33}$$

where $u(x)$ and $v(x)$ can be expressed as an infinite Fourier series as in Eq. 2.19, and the coefficients $\hat{c}_k$ can be written as in Eq. 2.16. If u and v are finite Fourier series of degree $\leq N/2$, then Eq. 2.33 can be rewritten as

$$\hat{c}_k = \sum_{\substack{m+n=k \\ |m|,|n| \leq N/2}} \hat{u}_m \hat{v}_n, \quad |k| \leq N/2 \ . \tag{2.34}$$

This expression takes $O\left(N^2\right)$ operations in one dimension and is costly especially when compared to finite-difference algorithms which take $O(N)$ operations. To avoid this, Orszag suggested the pseudo-spectral technique of taking the inverse DFT (Discrete Fourier Transform) to transform $\hat{u}_m$ and $\hat{v}_n$ to the physical space, perform the multiplication like in Eq. 2.32, and transform back to Fourier space using the DFT to get the final expression. This greatly reduces the cost to $O(N \log_2 N)$ operations. However this method leads to an aliasing error as shown below.

Consider

$$c_j = u_j v_j, \quad j = 0, 1, \ldots, N-1 \ , \tag{2.35}$$

where u_j and v_j are the discrete Fourier series defined similar to Eq. 2.26, and $\tilde{c}_k$ are the discrete Fourier coefficients defined similar to Eq. 2.24. Using the orthogonality relation in Eq. 2.25, we get

$$\tilde{c}_k = \sum_{m+n=k} \hat{u}_m \hat{v}_n + \sum_{m+n=k\pm N} \hat{u}_m \hat{v}_n = \hat{c}_k + \sum_{m+n=k\pm N} \hat{u}_m \hat{v}_n \ . \tag{2.36}$$

The second term on the RHS is the aliasing error as previously explained.

2.3.4 De-aliasing by Zero Padding or Truncation

First consider M instead of N points. We will show here that using $M \geq 3N/2$ will be able to de-alias. Assuming the following for the discrete transform :

$$y_j = \frac{2\pi j}{M}, \quad \bar{u}_j = \sum_{k=-M/2}^{M/2-1} \tilde{u}_k e^{iky_j}, \quad \bar{v}_j = \sum_{k=-M/2}^{M/2-1} \tilde{u}_k e^{iky_j}, \quad \bar{c}_j = \bar{u}_j \bar{v}_j \ , \tag{2.37}$$

for $j = 0, 1, \ldots, M-1$, where

$$\check{u}_k = \begin{cases} \hat{u}_k, & |k| \leq N/2 \ , \\ 0 & \text{otherwise} \ . \end{cases} \tag{2.38}$$

Putting it into words, the coefficients $\check{u}_k$ are nothing but the coefficients $\hat{u}_k$ padded with zeros for the additional wavenumbers. Now, we can write

$$\check{c}_k = \frac{1}{M} \sum_{j=0}^{M-1} \bar{c}_j e^{-iky_j}, \quad k = -M/2, \ldots, M/2-1 \ , \tag{2.39}$$

giving

$$\check{c}_k = \sum_{m+n=k} \check{u}_m \check{v}_n + \sum_{m+n=k\pm M} \check{u}_m \ . \check{v}_n \tag{2.40}$$

We now choose M so that the second term on the RHS vanishes for $|k| \leq N/2$. Noting that $\check{u}_m$ and $\check{u}_n$ are zero for $|m| > N/2$, we can use

$$-N/2 - N/2 \leq N/2 - 1 - M, \quad \text{or} \quad M \geq 3N/2 - 1 \ . \tag{2.41}$$

We thus obtain the de-aliased coefficients

$$\hat{c}_k = \check{c}_k, \quad k = -N/2, \ldots, N/2-1 \ . \tag{2.42}$$

This de-aliasing technique is referred to as the 3/2-rule and requires FFT's that can handle multiples of 3 (power of 3). If only a prime factor 2 FFT is available, then this technique can be implemented by choosing M as the smallest power of 2 that satisfies Eq. 2.41. Then, the technique is known as truncation, also known as the 2/3 rule. For more information on the Fourier pseudo-spectral technique, refer Canuto *et al.* (2006) and Boyd (2001).

2.3.5 Application of Fourier bases to our system

We consider a domain that is doubly periodic. We discretize it into an even number of points in both x and y directions, and take the Fourier transform in space of Eq. set 2.14. We define the expressions for 2D DFT and inverse DFT respectively as

$$\hat{\omega}(m,n,t) = \frac{1}{M}\frac{1}{N} \sum_{j=0}^{M-1} \sum_{k=0}^{N-1} \omega(x_j, y_k, t)\, e^{-i(mx_j + ny_k)} \ , \tag{2.43}$$
$$m = -M/2, \ldots, M/2-1, \quad n = -N/2, \ldots, N/2-1 \ ,$$

$$\omega(x_j, y_k, t) = \sum_{m=-M/2}^{M/2-1} \sum_{n=-N/2}^{N/2-1} \hat{\omega}(m,n,t)\, e^{i(mx_j + ny_k)} \ , \tag{2.44}$$
$$j = 0, \ldots, M-1, \quad k = 0, \ldots, N-1 \ ,$$

where the collocation points are given by

$$x_j = \frac{2\pi j}{M}, \quad j = 0, \ldots, M-1 \qquad \text{and} \qquad y_k = \frac{2\pi k}{N}, \quad k = 0, \ldots, N-1 \ . \tag{2.45}$$

Note that the collocation points and wavenumbers defined above and previously are for a periodic domain of length 2π. The points and wavenumbers corresponding to a two dimensional periodic domain of arbitrary length L_x and L_y are given by

$$x_j = \frac{L_x j}{M}, \quad j = 0, \ldots, M-1 \qquad \text{and} \qquad y_k = \frac{L_y k}{N}, \quad k = 0, \ldots, N-1 \ , \tag{2.46}$$

$$\begin{aligned} m &= -(M/2) * dm, \ldots, (M/2-1) * dm, \qquad dm = 2\pi/L_x, \\ n &= -(N/2) * dn, \ldots, (N/2-1) * dn, \qquad dn = 2\pi/L_y \ . \end{aligned} \tag{2.47}$$

Taking the Fourier transform of Eqs. 2.14 and using some of the basic properties of differentiation described earlier, we get

$$\frac{d\hat{\omega}}{dt} + \widehat{C1} - \widehat{C2} = -\nu l^2 \hat{\omega} \ , \tag{2.48}$$

$$\hat{\psi} = \frac{\hat{\omega}}{l^2}, \quad l \neq 0 \ , \tag{2.49}$$

where $l^2 = m^2 + n^2$, and $\widehat{C1}$ and $\widehat{C2}$ are the convolution sums given by

$$\widehat{C1} = \widehat{\frac{\partial \psi}{\partial y}\frac{\partial \omega}{\partial x}}, \quad \widehat{C2} = \widehat{\frac{\partial \psi}{\partial x}\frac{\partial \omega}{\partial y}} \ . \tag{2.50}$$

We have used the 3/2 de-aliasing technique described earlier, in evaluating the convolution. Also, for $l = 0$, we set $\hat{\psi} = 0$ (mean of ψ is equal to zero).

2.4 Temporal discretization

We have used an explicit Runge-Kutta fourth order time-stepping technique for the temporal discretization. We perform the time stepping while still in the Fourier space. We move back to the physical space only when computing the convolution using the 3/2 de-aliased pseudo-spectral method. The steps involved are given below:

Step 1 :

$$\hat{\omega}_1 = \hat{\omega}_0 + \frac{\Delta t}{2}\left(-\nu l^2 \hat{\omega}_0 - \widehat{C1}_0 + \widehat{C2}_0\right) \ , \tag{2.51}$$

Step 2 :

$$\hat{\omega}_2 = \hat{\omega}_0 + \frac{\Delta t}{2}\left(-\nu l^2 \hat{\omega}_1 - \widehat{C1}_1 + \widehat{C2}_1\right) \ , \tag{2.52}$$

Step 3 :

$$\hat{\omega}_3 = \hat{\omega}_0 + \Delta t \left(-\nu l^2 \hat{\omega}_2 - \widehat{C1}_2 + \widehat{C2}_2 \right) \ , \tag{2.53}$$

Step 4 :

$$\begin{aligned} \hat{\omega}_4 = \hat{\omega}_0 + \frac{\Delta t}{6} \Bigg\{ & \left(-\nu l^2 \hat{\omega}_0 - \widehat{C1}_0 + \widehat{C2}_0 \right) + 2 \left(-\nu l^2 \hat{\omega}_1 - \widehat{C1}_1 + \widehat{C2}_1 \right) \\ & + 2 \left(-\nu l^2 \hat{\omega}_2 - \widehat{C1}_2 + \widehat{C2}_2 \right) + \left(-\nu l^2 \hat{\omega}_3 - \widehat{C1}_3 + \widehat{C2}_3 \right) \Bigg\} \ , \end{aligned} \tag{2.54}$$

where Δt is the time-step and

$$\hat{\psi}_n = \frac{\hat{\omega}_n}{l^2}, \quad \widehat{C1}_n = \widehat{\frac{\partial \psi_n}{\partial y}} \widehat{\frac{\partial \omega_n}{\partial x}}, \quad \widehat{C2}_n = \widehat{\frac{\partial \psi_n}{\partial x}} \widehat{\frac{\partial \omega_n}{\partial y}} \ . \tag{2.55}$$

Finally, we take the inverse DFT of Eq. 2.54 to get the value of the vorticity and streamfunction at each grid point.

Chapter 3

Vortex Merger: Validation and Results

3.1 Scope

This chapter contains the validation of the pseudo-spectral code and the results from the vortex merger simulations in the case of multiple vortices. To begin with, we define the initial conditions and the various parameters involved in the simulations. We go on to discuss our main findings and then conclude.

3.2 Setting up the problem

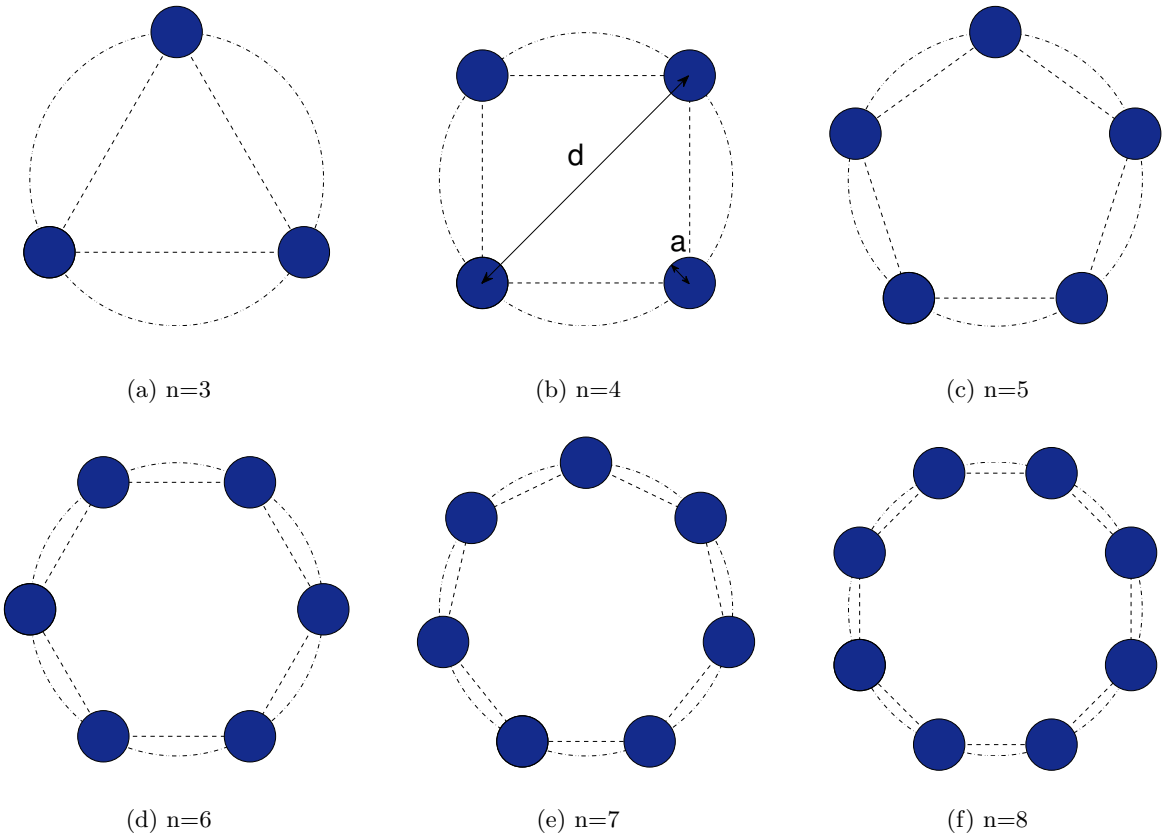

(a) n=3 (b) n=4 (c) n=5

(d) n=6 (e) n=7 (f) n=8

Figure 3.1: A schematic of n equal co-rotating vortices arranged at equal intervals on the circumference of a circle of radius R and diameter d, on the vertices of regular polygons. Each vortex has circulation Γ/n.

Here we look at the initial conditions, various parameters and non-dimensional numbers in

our merger simulations. To begin with, we consider n equal co-rotating vortices (n varying from 2 to 8), arranged at equal intervals on the circumference of a circle of radius R and diameter d, on the vertices of regular polygons (Fig. 3.1). Each of these vortices have a gaussian vorticity profile given by $\omega = \omega_0 e^{-r^2/a^2}$, and are of equal strength or circulation Γ/n. Here, a is the size of a vortex core ($a^2 = \langle r^2\omega\rangle/\langle\omega\rangle$) and ω_0 is the maximum vorticity, given by $\omega_0 = \Gamma/\left(n\pi a^2\right)$. The total circulation in the system is given by Γ and kinematic viscosity is represented by ν. In all our simulations, we keep the initial (a/d) constant, where a is the characteristic core size and d is the diameter of the circle on which the vortices lie. From now on, we refer to this as $(a/d)_i$.

We make comparisons between systems with different number of vortices by first keeping the $(a/d)_i$ constant. To make fair comparisons, we follow two approaches: we either fix the total circulation or the energy. Hence, we define the Reynolds number in the following two ways.

- In the first case, we keep the total initial circulation Γ constant across the set of simulations. The Reynolds number is then given by

$$Re_\Gamma = \frac{\Gamma}{\nu} \, . \tag{3.1}$$

  Here, time is non-dimensionalized by a convective time scale which is the time period of rotation of point vortices of the same strength, given by

$$T_\Gamma = \frac{8n}{n-1}\frac{\pi^2 R^2}{\Gamma} \, . \tag{3.2}$$

- In the second case, we keep the total initial energy constant across the set of simulations. The energy calculations are based on the root mean square velocity u_{rms} and a cut off diameter d_0, which are then used as the velocity and length scale respectively in the Reynolds number given by

$$Re_{Energy} = \frac{u_{rms} d_0}{\nu} \, . \tag{3.3}$$

  Here, the time scale chosen for non-dimensionalization is given by

$$T_{Energy} = \frac{d_0}{u_{rms}} \, . \tag{3.4}$$

The Reynolds number defined in either way is kept constant across a given set of simulations. We track each vortex individually by defining a separation distance b which is the distance between the vortex maximum and the center of the circle on which the vortices were initially placed. We non-dimensionalize this by the initial separation distance b_0 at $t = 0$.

All the results presented here are for a domain size of $2\pi \times 2\pi$. The diameter of the circle on which the vortices lie is chosen such that the vortices do not feel the effect of the ghost vortices on account of the periodic boundary condition due to the Fourier basis. By varying the diameter d, keeping the length L of the domain constant, we conducted a domain independence

study and found $d = 0.5$ to be a safe choice (this gives $L/d = 12.56637$). We the choose the grid such that we are able the capture the Kolomogorov length scale based on the Reynolds number. The grids that we have tried are 512×512, 1024×1024 and 2048×2048.

3.3 Validation and results

We performed the first validation of the code by giving the initial condition as a single gaussian vortex at the center of the domain, and let the vortex diffuse. We compared the time evolution of the vorticity profile from the simulation with that of the well established analytical result for a gaussian or Lamb-Oseen vortex given by

$$\omega = \frac{\Gamma_o}{4\pi\nu t} e^{-\left(\frac{r^2}{4\nu t}\right)} \ , \tag{3.5}$$

where Γ_o is total circulation, ν is the viscosity and t is the time. We choose $\nu t = 0.01$, $\Gamma_o = 1$, and let the vortex evolve. Fig. 3.2 shows the comparison of the numerical solution with the analytical one and we can immediately see that it is a good match. One must however note that diffusion of an axis-symmetric gaussian vortex is a linear phenomenon, and thus, this validation only proves that the code can capture linear effects.

Next, to check if non-linear effects can be captured, we perform the next validation of our pseudo-spectral code with Brandt & Nomura (2006) and Brandt & Nomura (2007), for the merger of two vortices. Fig. 3.3 shows the comparison of the non-dimensional separation distance b^* vs the non-dimensional time t^* at two different Reynolds numbers and it can be seen that there is a good match. It must be noted that the data available from their work is incomplete and doesn't resolve completely the third and final stages of merger, whereas our result is presented for all four stages and is able to accurately capture and resolve them.

We next move on to the results of our merger simulations. In order to simplify the understanding of the merger phenomenon, we first look at the Figs. 3.4 and 3.5 which depict separatrices in the co-rotating frame for point vortices placed at equal intervals on the circumference of a circle. It can be seen that the separatrices divide the fluid flow into distinct regions. We define the regions as follows: (1) central (not present for two vortices), (2) inner core, (3) exchange band, (4) outer recirculating and (5) outer flow. Note that the outer recirculating region has fluid rotating in a sense opposite to the the inner core and exchange band regions. Despite the name, this region has no net circulation. Note that only region 2 contains vorticity.

We now move on to discuss viscous simulations with patch vortices, and see that the regions discussed above are no longer distinct, but still retain some identity. Vorticity can now leak preferentially along what used to be separatrices in the point vortex case. Fig. 3.6 shows the viscous evolution of two gaussian vortices with $(a/d)_i = 0.1$ and $Re_\Gamma = 4000$. During the first stage of merger, the vortices first grow in size by viscous diffusion. It can also be seen that each vortex deforms and elongates slightly, which is due to the strain field produced by the others. Towards the end of this stage (when (a/d) is close to the $(a/d)_{crit}$), there is a development of

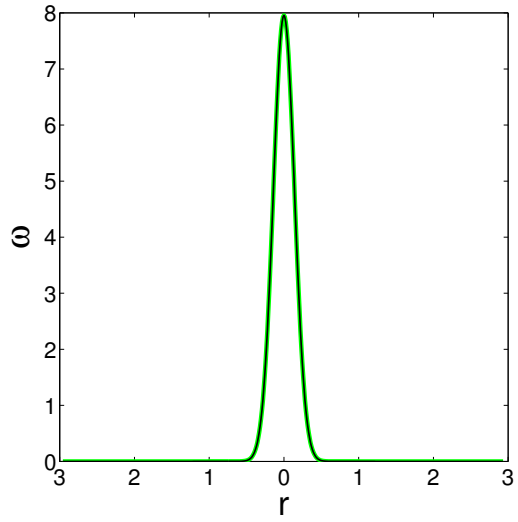

(a) $t = 10$

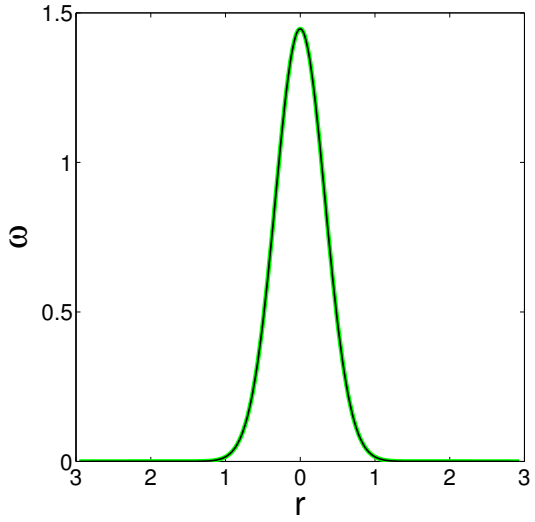

(b) $t = 55$

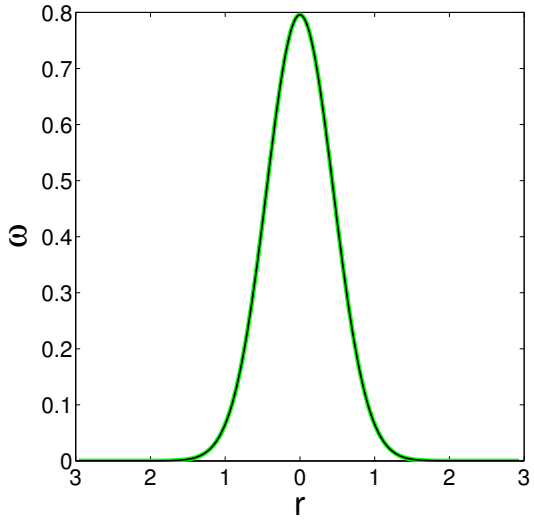

(c) $t = 100$

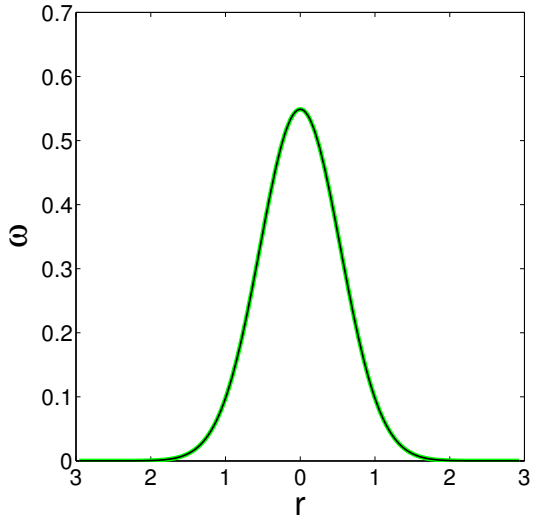

(d) $t = 145$

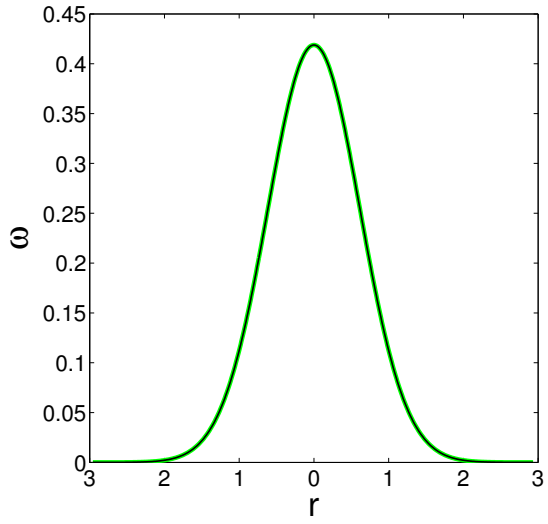

(e) $t = 190$

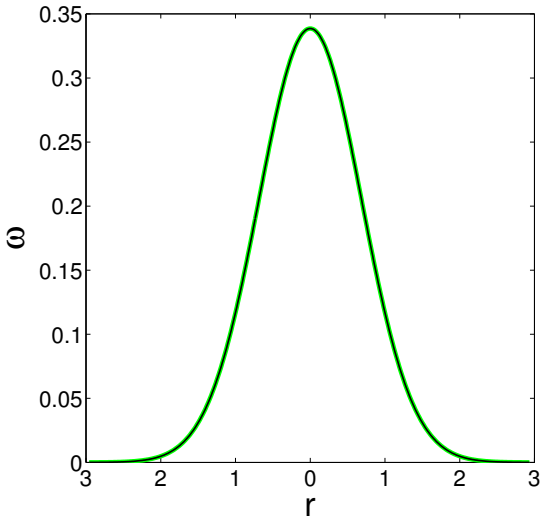

(f) $t = 235$

Figure 3.2: Validation of pseudo-spectral code (green line) with analytical result (black line), for an initial condition ($\nu t = 0.01$, $\Gamma_o = 1$) of a gaussian or a Lamb-Oseen vortex (line vortex at $t = 0$).

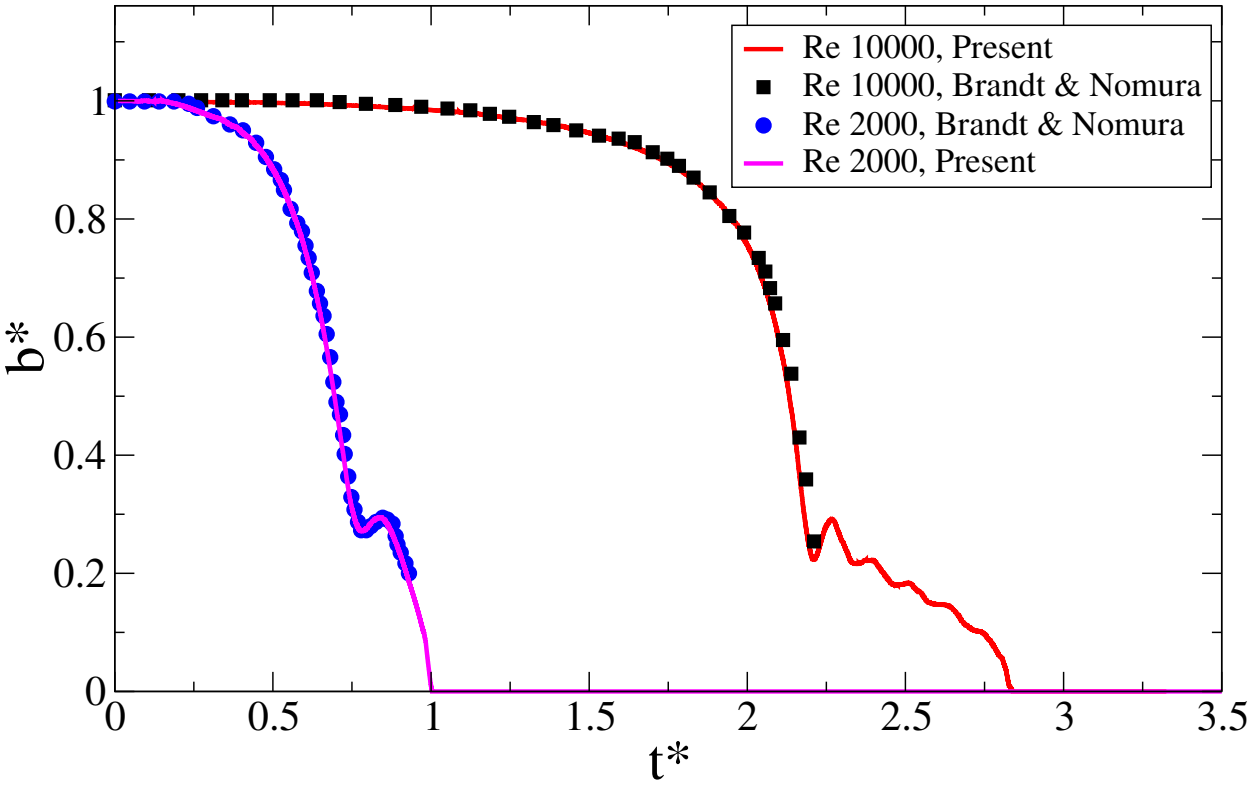

Figure 3.3: Validation of pseudo-spectral code with Brandt & Nomura (2006) ($Re = 2000, (a/d)_i = 0.177$) and Brandt & Nomura (2007) ($Re = 10000, (a/d)_i = 0.157$), Non-dimensional separation distance b^* vs non-dimensional time t^*.

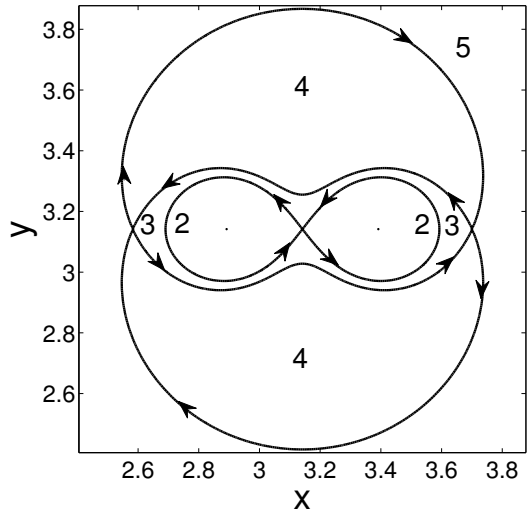

Figure 3.4: Co-rotating frame streamfunction for 2 point vortices. The regions are distinguished as follows: (2) inner core, (3) exchange band, (4) outer recirculating and (5) outer flow.

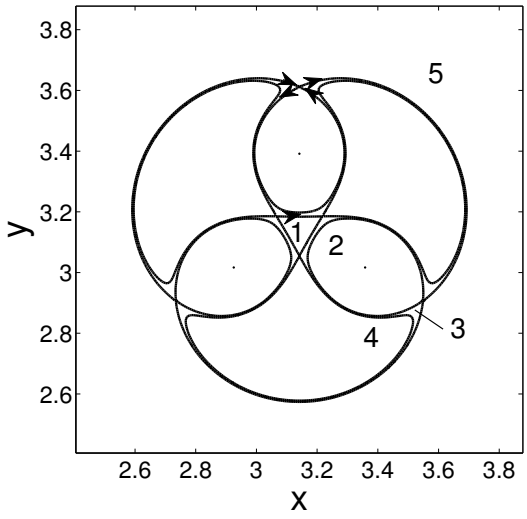

(a) 3 vortices

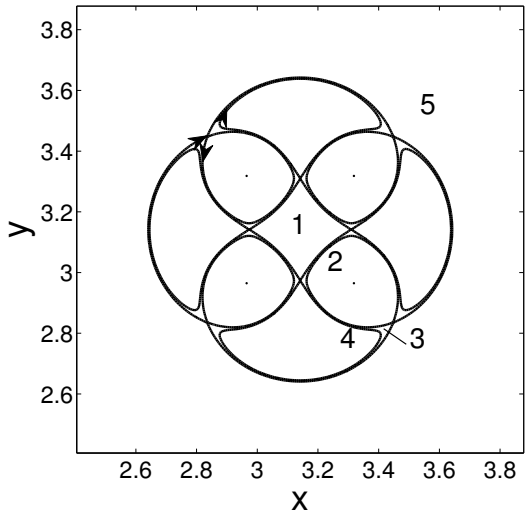

(b) 4 vortices

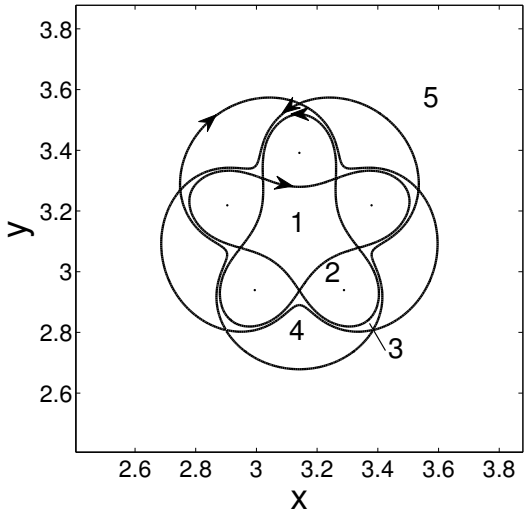

(c) 5 vortices

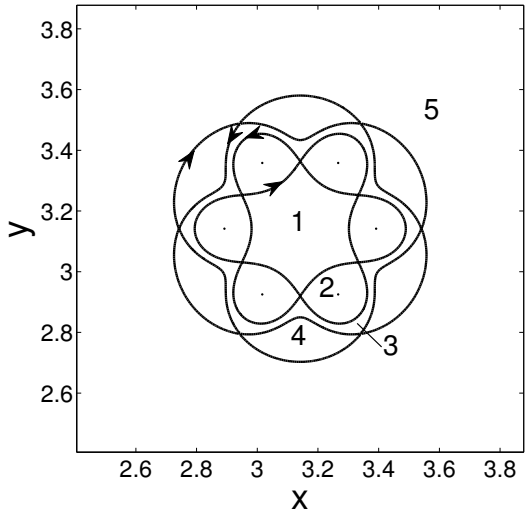

(d) 6 vortices

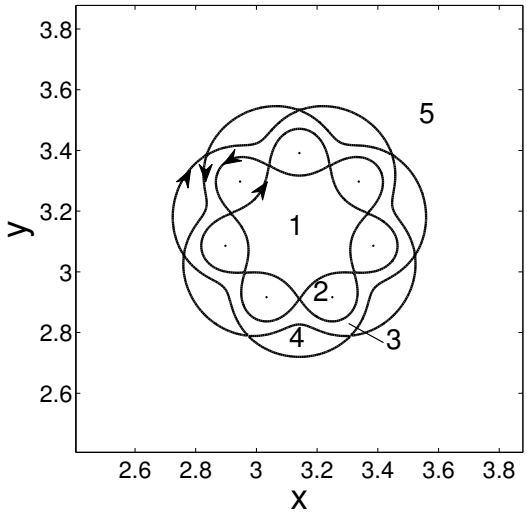

(e) 7 vortices

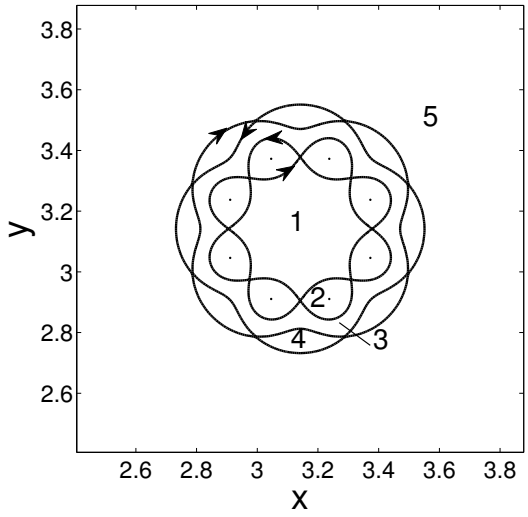

(f) 8 vortices

Figure 3.5: Co-rotating frame streamfunction for point vortices arranged at equal intervals around the circumference of a circle. The regions are distinguished as follows: (1) central (not present for 2 vortices), (2) inner core, (3) exchange band, (4) outer recirculating and (5) outer flow.

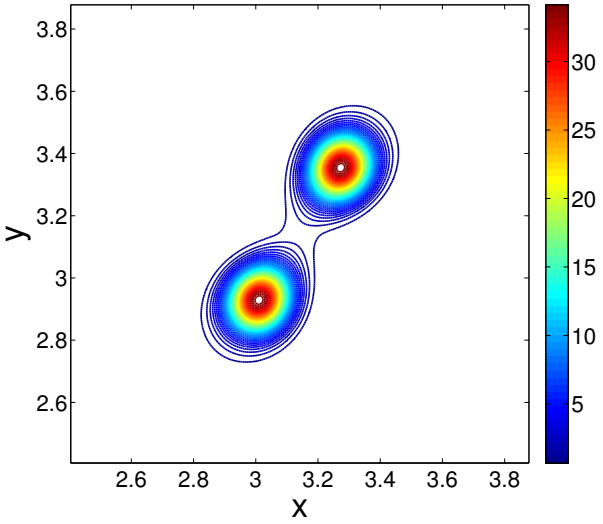

(a) $t^* = 0.669$

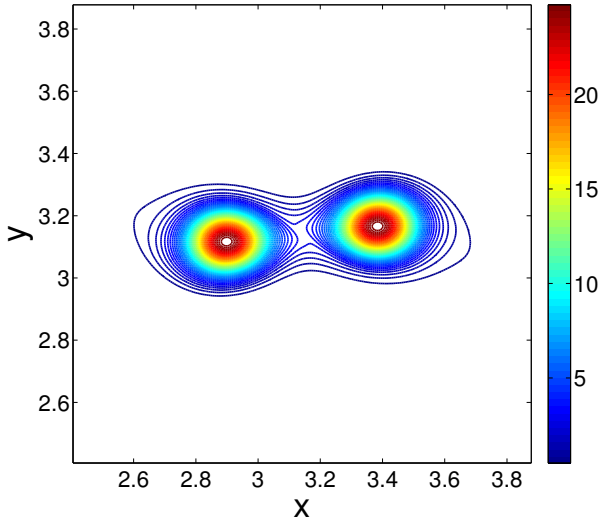

(b) $t^* = 1$

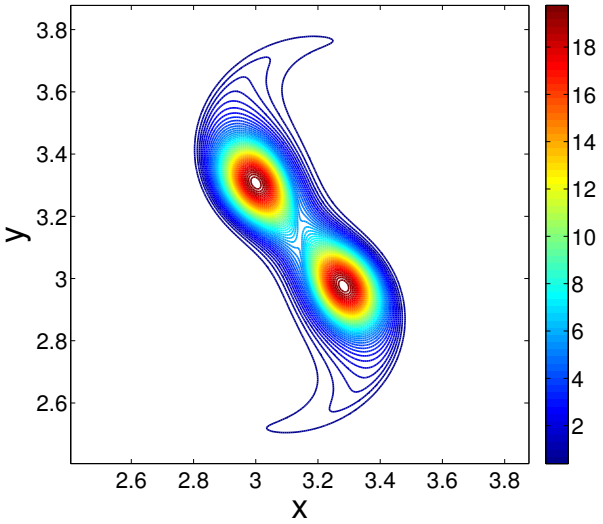

(c) $t^* = 1.317$

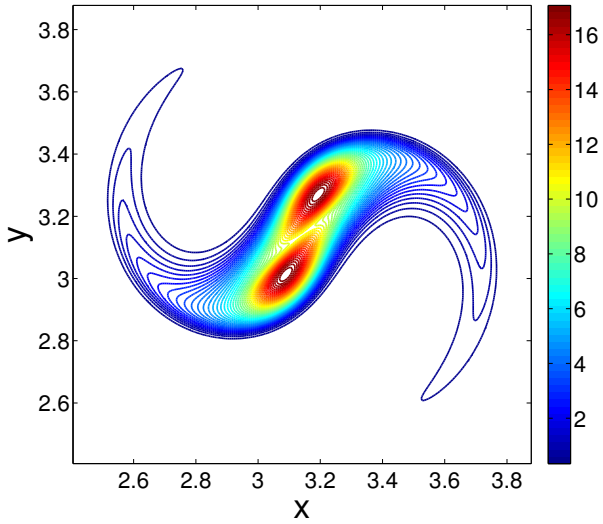

(d) $t^* = 1.52$

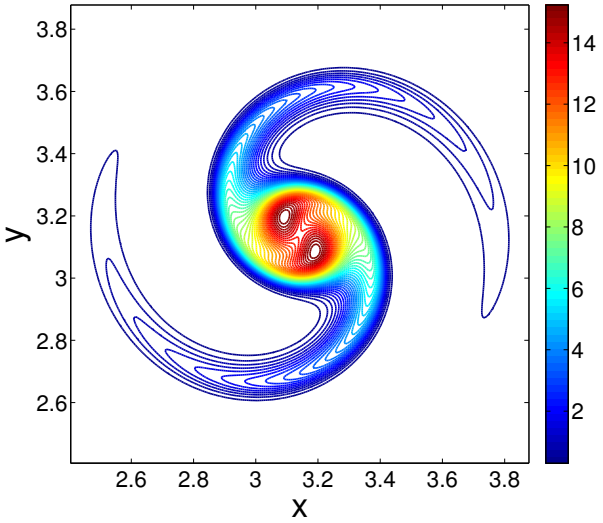

(e) $t^* = 1.66$

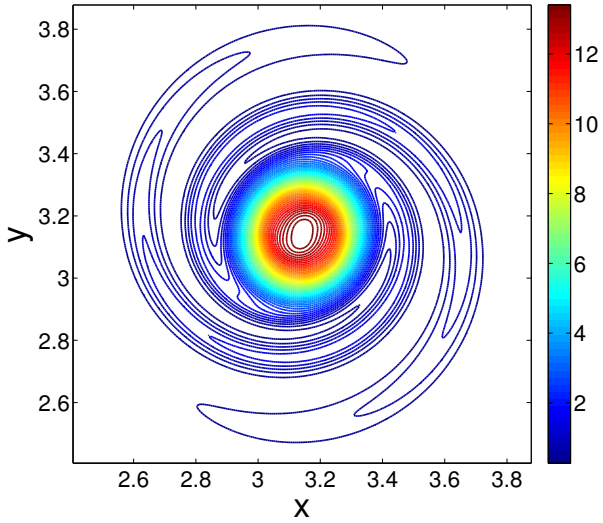

(f) $t^* = 2$

Figure 3.6: Viscous evolution of 2 gaussian vortices with $(a/d)_i = 0.1$ and $Re_\Gamma = 4000$. Observe the deformation of vortices and tilt with respect to the line joining the centers.

a slight tilt of the major axes of the deformed vortices with the line joining the the centroids to the center of rotation, once again due to the strain field. At one stage the critical (a/d) is reached, when the tilt is more pronounced and this places vorticity in the exchange band and outer recirculating regions (filaments) leading to the formation of antisymmetric ω. At this point the antisymmetric vorticity induces a velocity which is then responsible for pushing the vortices together, which occurs on a convective or circulation time scale. Also, it becomes very evident from Fig. 3.4 that the formation of filaments is due to the differential rotation of the outer recirculating region. At the end of the convective stage, the vortices are not yet completely merged and we still get two vorticity maxima. This is then followed by a second diffusive stage which is believed to be a diffusive stage where in the induced velocity of the antisymmetric vorticity field is not enough to push the vortices closer, and the coming together of the vorticity maxima is achieved by simple diffusion. The final stage is basically the axisymmetrization and growth in size of the merged vortex, which also includes the smoothening out of filaments.

We next move on to the three-vortex merger case with $(a/d)_i = 0.1$ and $Re_\Gamma = 4000$. From Fig. 3.7, It can be seen that initially that the vortex cores grow in size by diffusion. Also, due to the strain field of the three-vortex system, the vortices deform to elongate into an elliptical shape and align themselves radially. Towards the end of this first diffusive stage, the strain field results in a slight tilt of the vortices to the radius vector. Once a critical (a/d) is reached, the tilt becomes prominent and results in the formation of antisymmetric vorticity similar to the two vortex case discussed previously. This once again consists of vorticity in the exchange band as well as outer recirculation regions. The antisymmetric ω induces a velocity which causes the vortices to move radially inward (reduction in separation distance b^*). Once again, the formation of filaments can be explained from Fig. 3.5 based on the differential rotation in the outer recirculating region. Towards the end of the convective stage, we observe that the vortices realign themselves, changing their alignment from radial to azimuthal to form an annulus-like vortex structure. This is then followed by a diffusive stage, where the annulus-like structure forms a single maximum in the centre by viscous diffusion.

In order to improve our understanding of the three-vortex merger phenomenon, we also study the inviscid evolution of three uniform patch vortices and compare it with the high Reynolds number viscous evolution of gaussian vortices. These inviscid simulations are carried out with the help of a contour dynamics code from Pozrikidis (2011). Here, the contour bounding each vortex patch is discretized into N line segments joining N nodes, with each line segment approximated by an arc drawn for every three successive nodes. The velocity at any point is then a sum of the contribution from each of the arcs joining the nodes (integration carried out by gaussian quadrature). This code also includes a provision for the addition, removal and redistribution of nodes in order to resolve regions with small radius of curvature. Once the velocities are known, an explicit Runge-Kutta second order scheme is used to march the positions of the contours in time. Refer Zabusky *et al.* (1979) for details regarding the concept of contour integration. For both the inviscid and viscous simulations, we maintain the same $(a/d)_i = 0.26$ and total circulation $\Gamma = 2$. We must remember that in the inviscid case, there is no diffusion and 'merger'

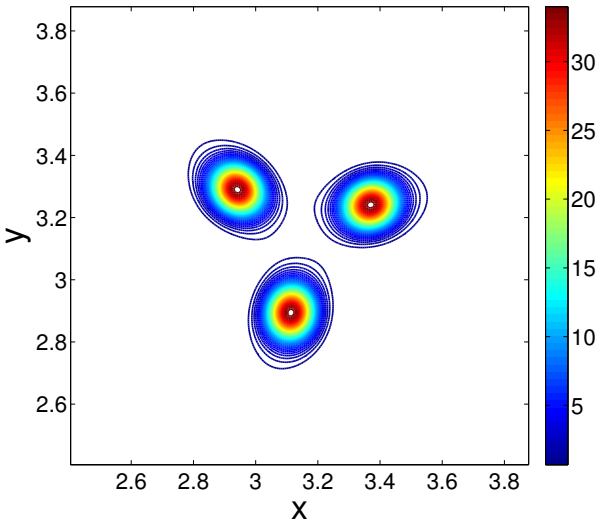

(a) $t^* = 0.49$

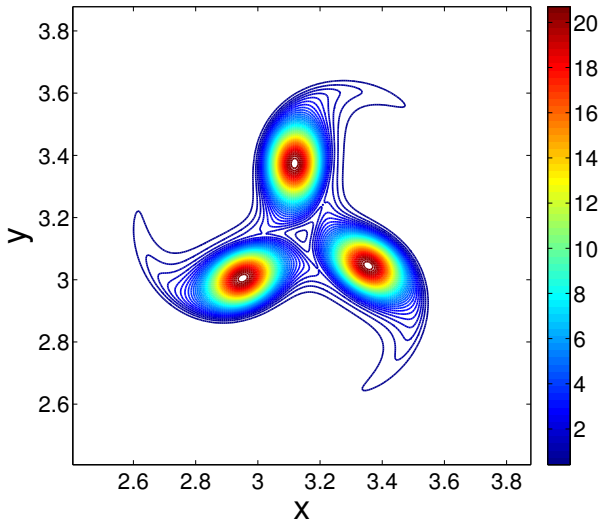

(b) $t^* = 1$

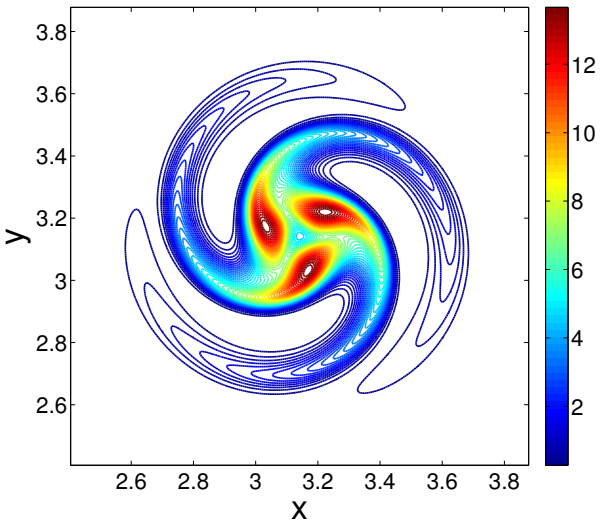

(c) $t^* = 1.513$

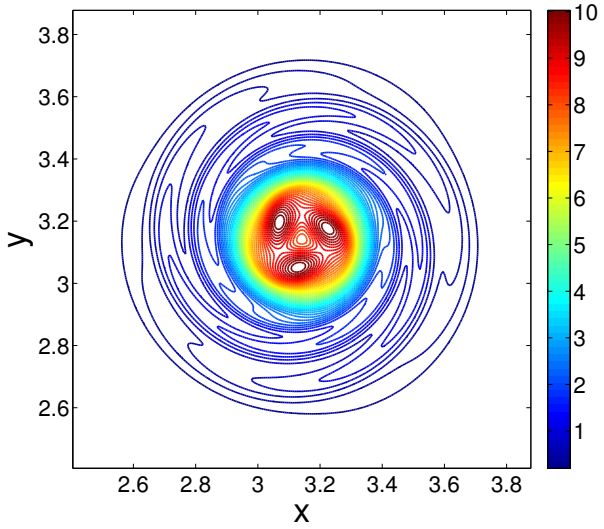

(d) $t^* = 2$

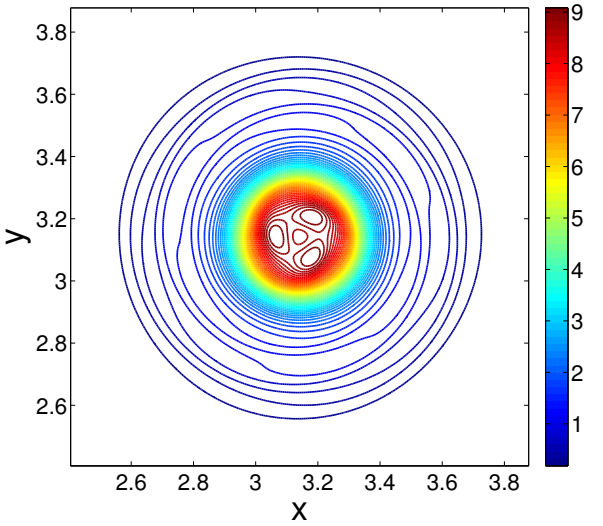

(e) $t^* = 2.3$

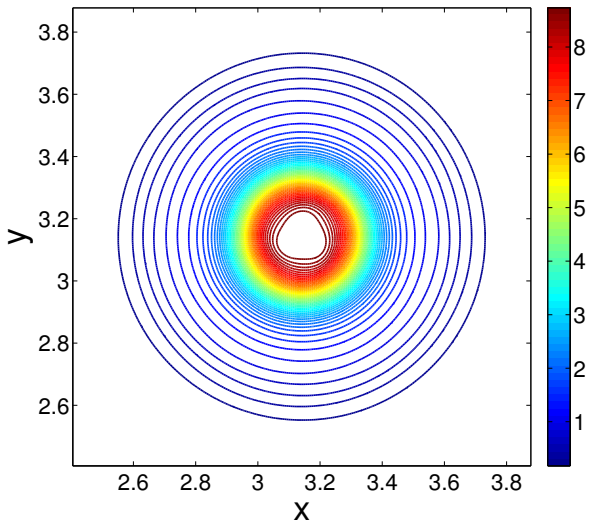

(f) $t^* = 2.6$

Figure 3.7: Viscous evolution of 3 gaussian vortices with $(a/d)_i = 0.1$ and $Re_\Gamma = 4000$, total initial $\Gamma = 2$ for both cases. Initial radial alignment of vortices with a tilt to the radius vector, azimuthal realignment towards the end of convective stage, annulus-like structure.

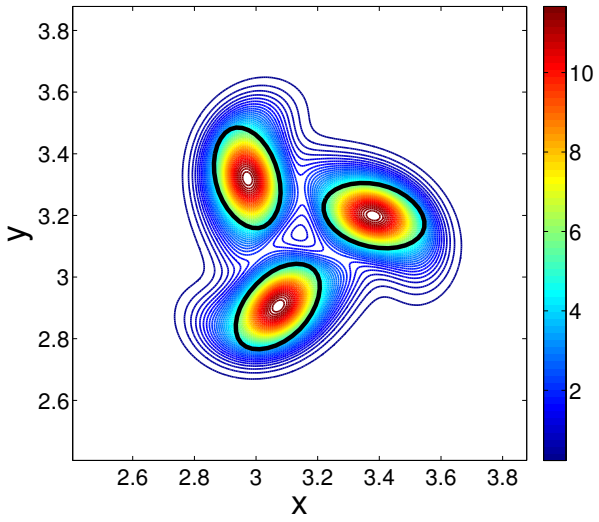

(a) $t^* = 0.12$

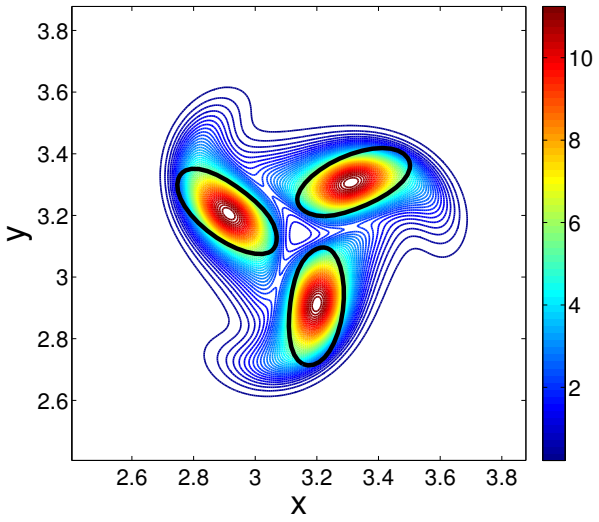

(b) $t^* = 2$

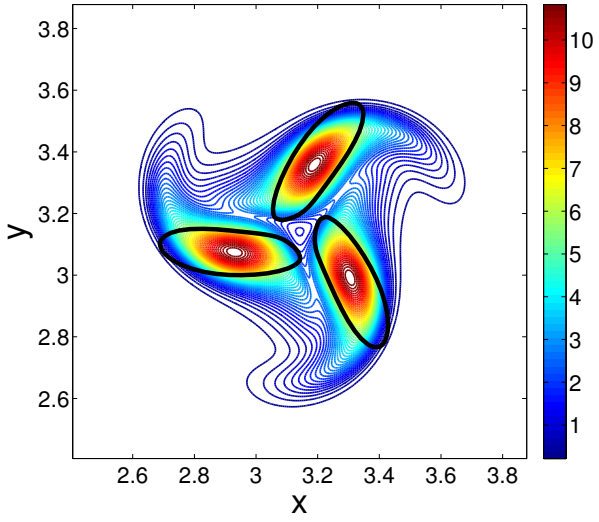

(c) $t^* = 0.28$

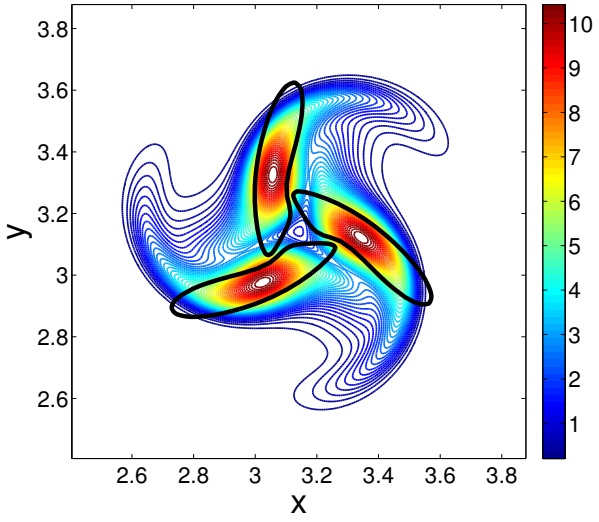

(d) $t^* = 0.36$

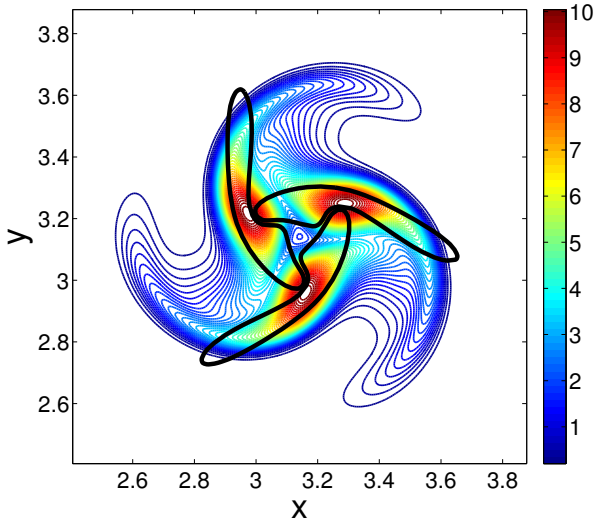

(e) $t^* = 0.45$

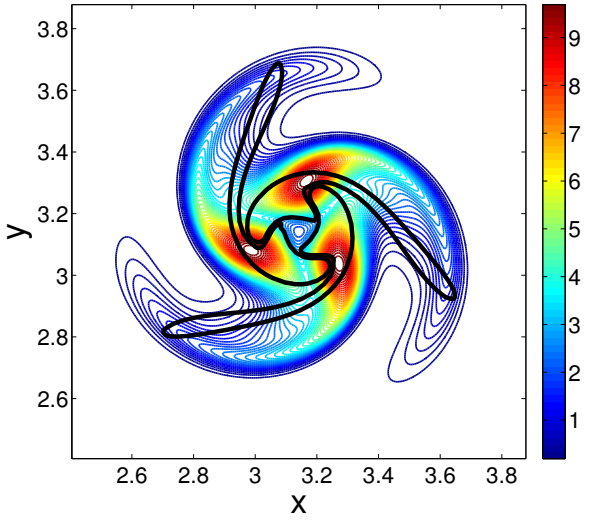

(f) $t^* = 0.53$

Figure 3.8: Inviscid evolution of 3 uniform patch vortices vs Viscous evolution of 3 gaussian vortices with $(a/d)_i = 0.26$ and $Re_\Gamma = 4000$. Total initial $\Gamma = 2$ for both cases. Observe similarity (initial radial alignment with a tilt to radius vector, azimuthal realignment towards the end to form annulus-like structure.

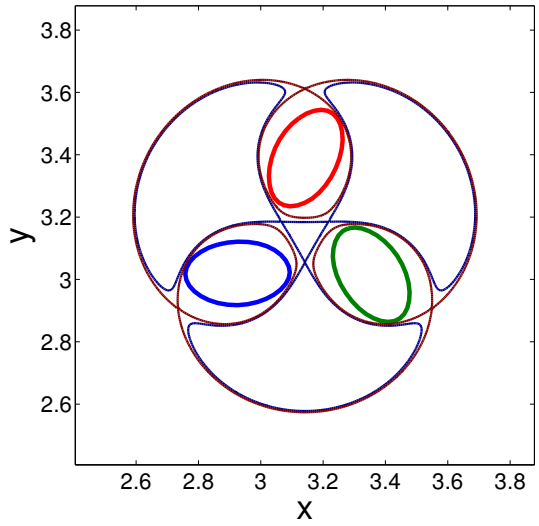

(a) $t^* = 1.8$

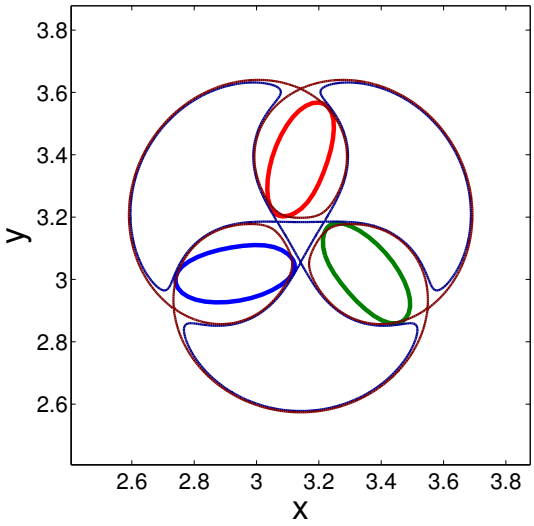

(b) $t^* = 3$

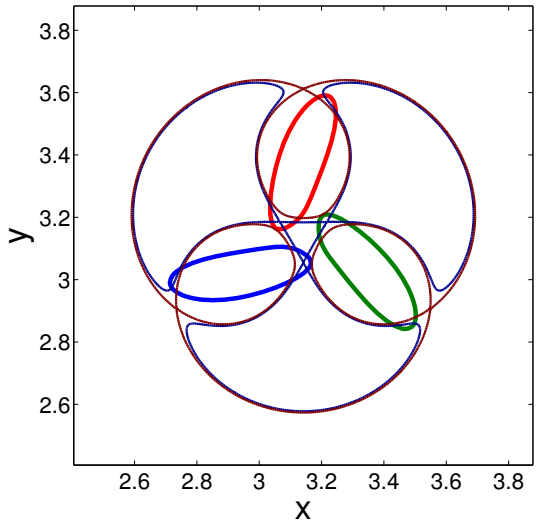

(c) $t^* = 4.2$

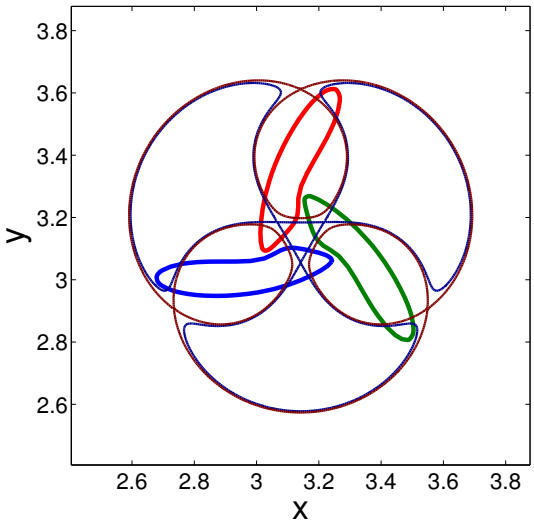

(d) $t^* = 5.4$

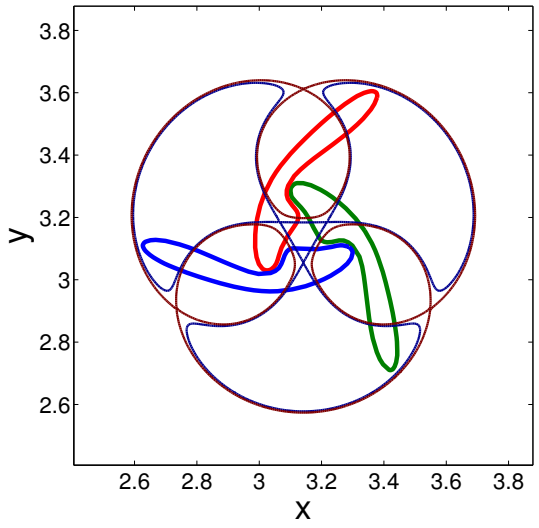

(e) $t^* = 6.6$

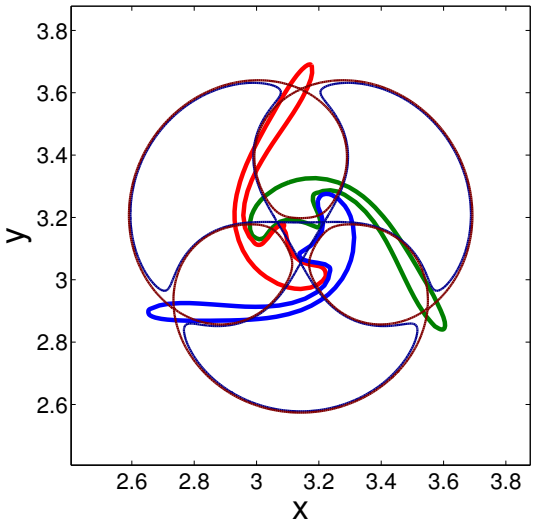

(f) $t^* = 7.8$

Figure 3.9: Inviscid evolution of 3 uniform patch vortices, shown in color, with $(a/d)_i = 0.26$ vs co-rotating streamfunction for 3 point vortices. The central band allows for the formation of annulus.

will occur only if the initial configuration itself is such that the $(a/d)_i \geq (a/d)_{crit}$. Hence the choice of $(a/d)_i = 0.26$. From Fig. 3.8, we can see clearly that the merger phenomenon in the inviscid case is similar to the viscous case during the convective stage (initial deformation and radial alignment with tilt to the radius, and azimuthal realignment towards the end) up until the formation of the annulus. At this point, in the inviscid case, an annular like structure is formed, but doesn't evolve any further (except that the filaments wrap around the annulus-like structure more tightly. As the filaments grow thinner and thinner, the numerical method cannot be continued forever, and fails at some finite time). Whereas, in the viscous case, as we have seen previously, this annulus-like structure diffuses to form a single vorticity maximum, with the added effect of viscosity smoothening out filaments.

The four-vortex merger is similar to the three-vortex case, as seen from Fig. 3.10. In fact the change in alignment from radial to azimuthal towards the end of the convective stage is more evident in the four vortex case. Also, the annular structure formed is cleaner in the four vortex case. Another phenomenon to be observed is the reduction in radius of the annulus to form a single gaussian vortex during the second diffusive stage. From Fig. 3.11, it can once again be seen clearly that the inviscid case is similar to the viscous evolution up until the formation of the annulus. In the inviscid case, Kelvin's circulation theorem dictates that the vortices cannot join to form a clean annulus. Whereas, in the viscous case, viscous diffusion assists in the formation of a clean annulus, followed by the reduction in radius of the annulus to form a single gaussian vortex. The formation of the annulus can be explained by looking at Figs. 3.9 and 3.12, where in we have superimposed the inviscid simulations over separatrices for point vortices. It is clear from these figures that there is an additional central region of fluid circulation which is absent in the two vortex case. Hence the two vortex case is not able to form an annulus and the multiple (>2) vortex case does.

Fig. 3.13 shows the viscous evolution of six gaussian vortices for $(a/d)_i = 0.1$ and $Re_\Gamma = 4000$. The strain field of the six-vortex case is such that even at short times, the vortices align themselves azimuthally. The antisymmetric ω and the formation of filaments is minimal, and hence the convective stage is completely absent in this case (unlike the two, three, four and five-vortex cases). It can be seen that this initial azimuthal alignment aids in the formation of an annulus from the beginning itself. So, the vortices just diffuse to form a clean annulus, which is then followed by a slow reduction in radius of the annulus on a diffusive time scale, to finally form a single gaussian vortex.

Fig. 3.14 shows the non-dimensional separation distance b^* vs non-dimensional time t^* for varying number of vortices, at $Re_\Gamma = 4000$ and same $(a/d)_i = 0.1$. The first thing that we observe is that the merger history for three or more vortices is quite different from that of the two-vortex merger case. It can be seen that the separation distance drop during the convective stage decreases as we increase the number of vortices from two to five, and convective stage completely disappears for six and more vortices. The most important finding here is that the second diffusive stage in the two-vortex merger is replaced by an annular stage which is again

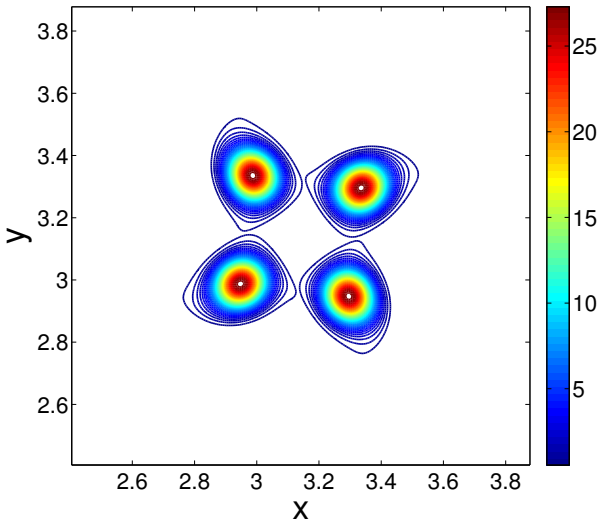

(a) $t^* = 0.486$

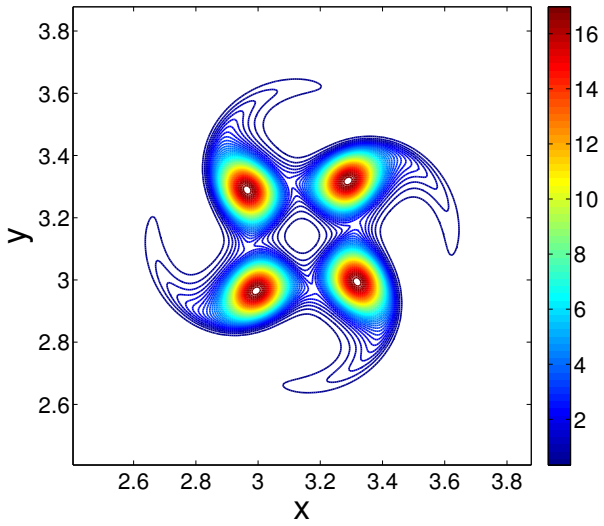

(b) $t^* = 1$

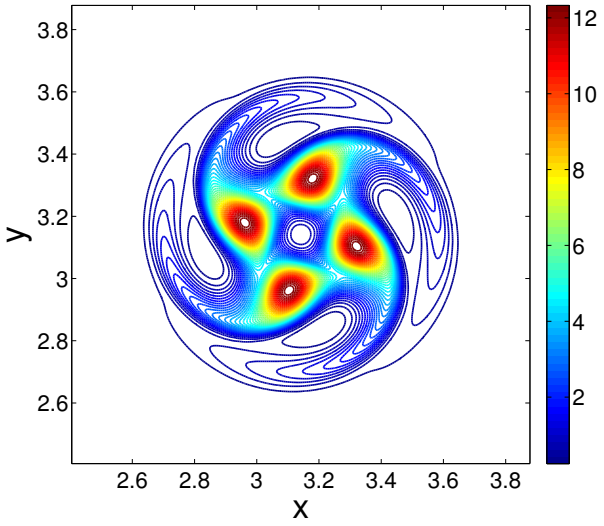

(c) $t^* = 1.49$

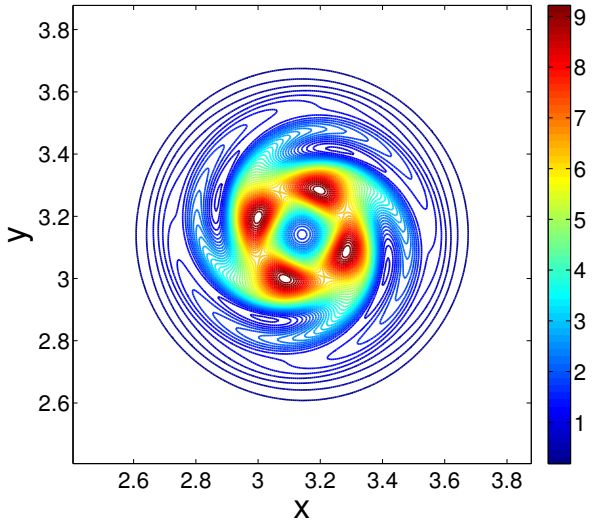

(d) $t^* = 2$

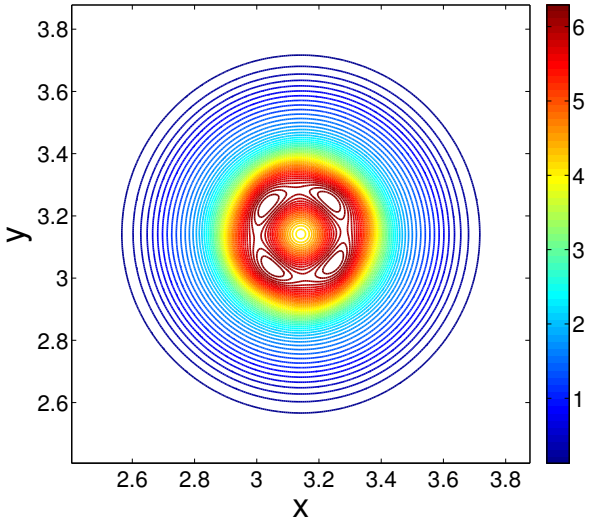

(e) $t^* = 3$

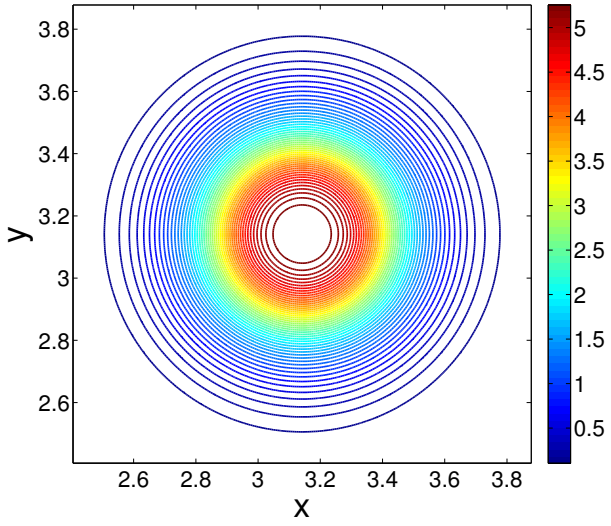

(f) $t^* = 5.5$

Figure 3.10: Viscous evolution of 4 gaussian vortices with $(a/d)_i = 0.1$ and $Re_\Gamma = 4000$. Initial radial alignment of vortices with a tilt to the radius vector, azimuthal realignment towards the end of convective stage, cleaner annulus.

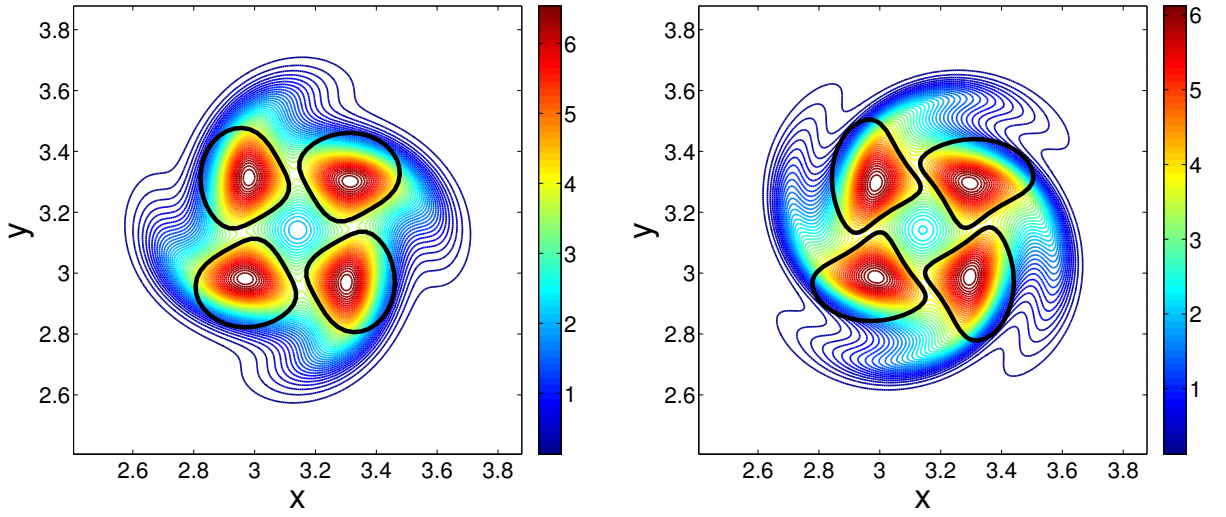

(a) $t^* = 0.81$ (b) $t^* = 1.62$

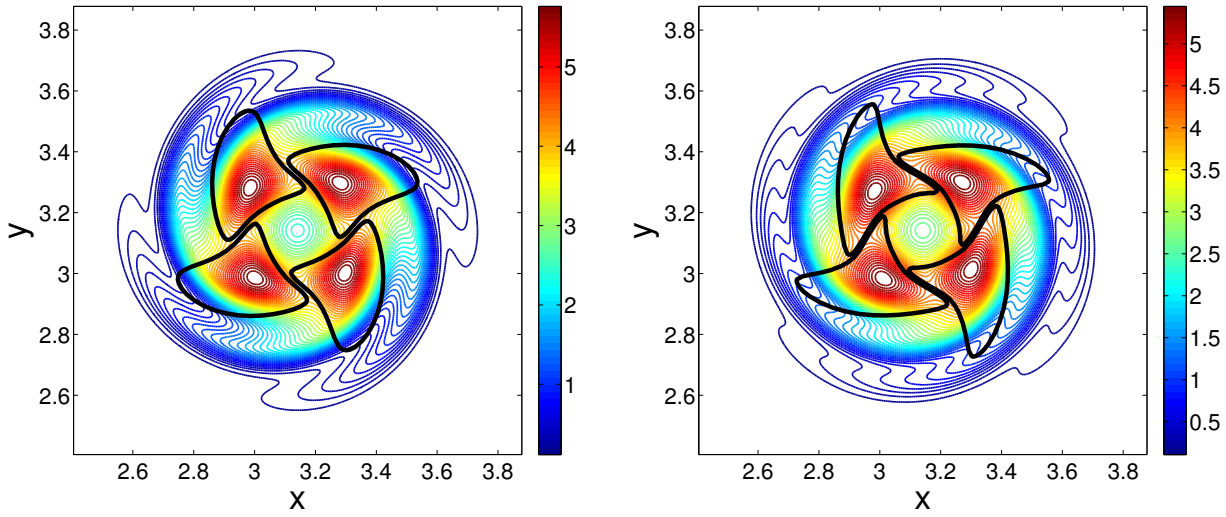

(c) $t^* = 2.43$ (d) $t^* = 3.24$

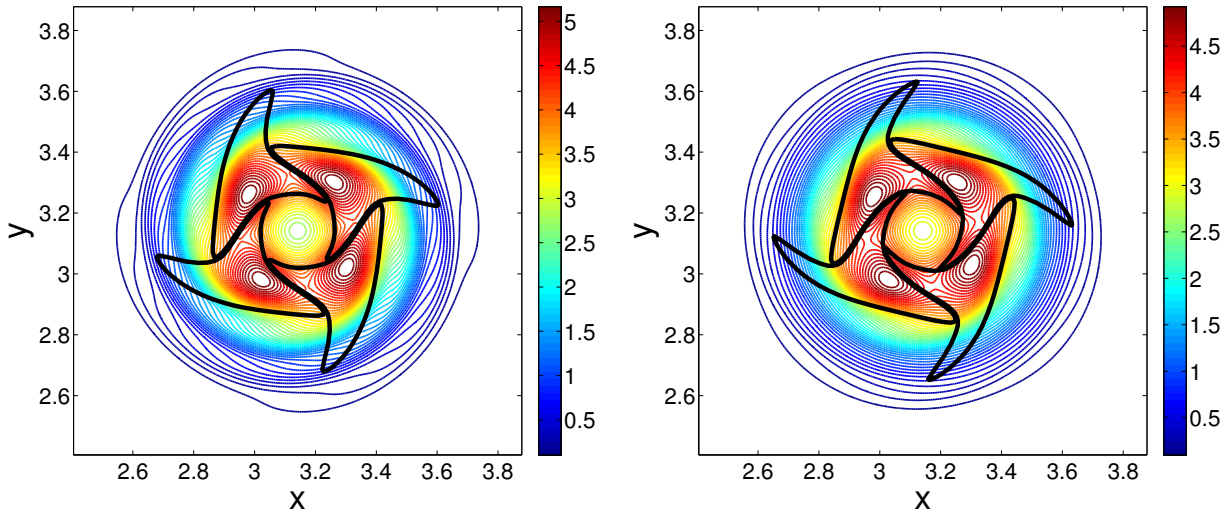

(e) $t^* = 4.05$ (f) $t^* = 4.86$

Figure 3.11: Inviscid evolution of uniform 4 patch vortices vs viscous evolution of 4 gaussian vortices with $(a/d)_i = 0.3$ and $Re_\Gamma = 4000$, total initial $\Gamma = 2$ for both cases. Observe similarity (initial radial alignment with a tilt to radius vector, azimuthal realignment towards the end to form annulus-like structure.

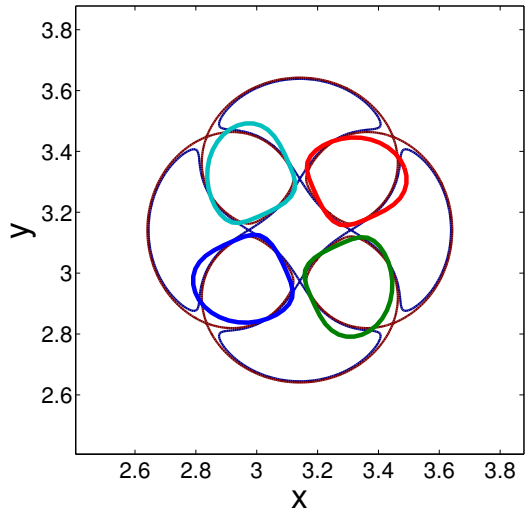

(a) $t^* = 0.81$

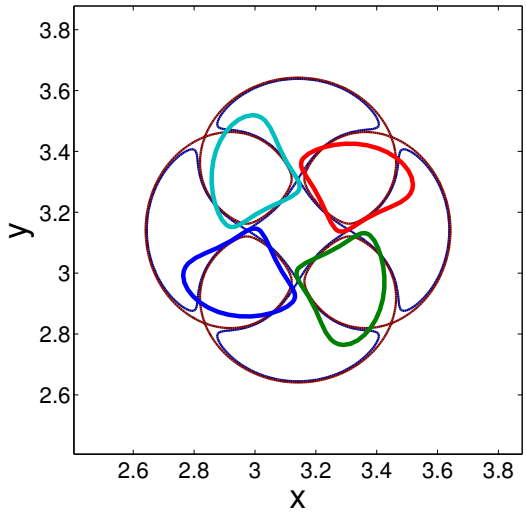

(b) $t^* = 1.62$

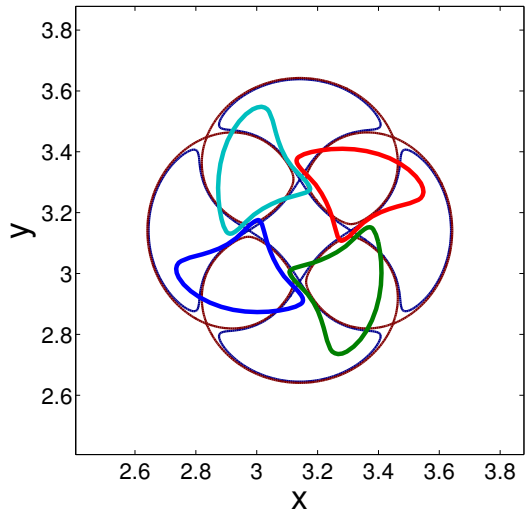

(c) $t^* = 2.43$

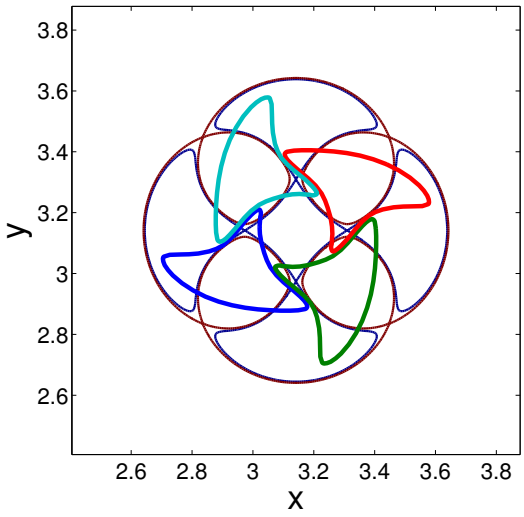

(d) $t^* = 3.24$

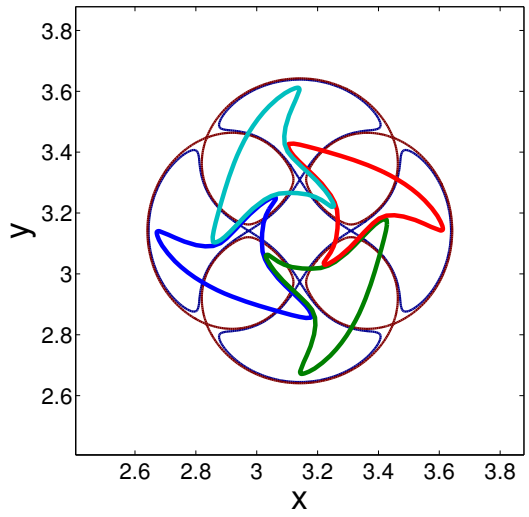

(e) $t^* = 4.05$

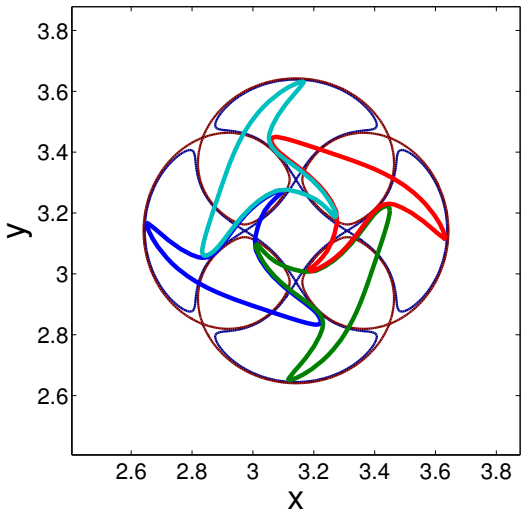

(f) $t^* = 4.86$

Figure 3.12: Inviscid evolution of 4 uniform patch vortices, shown in color, with $(a/d)_i = 0.3$ vs co-rotating streamfunction for 4 point vortices. The central band allows for the formation of annulus.

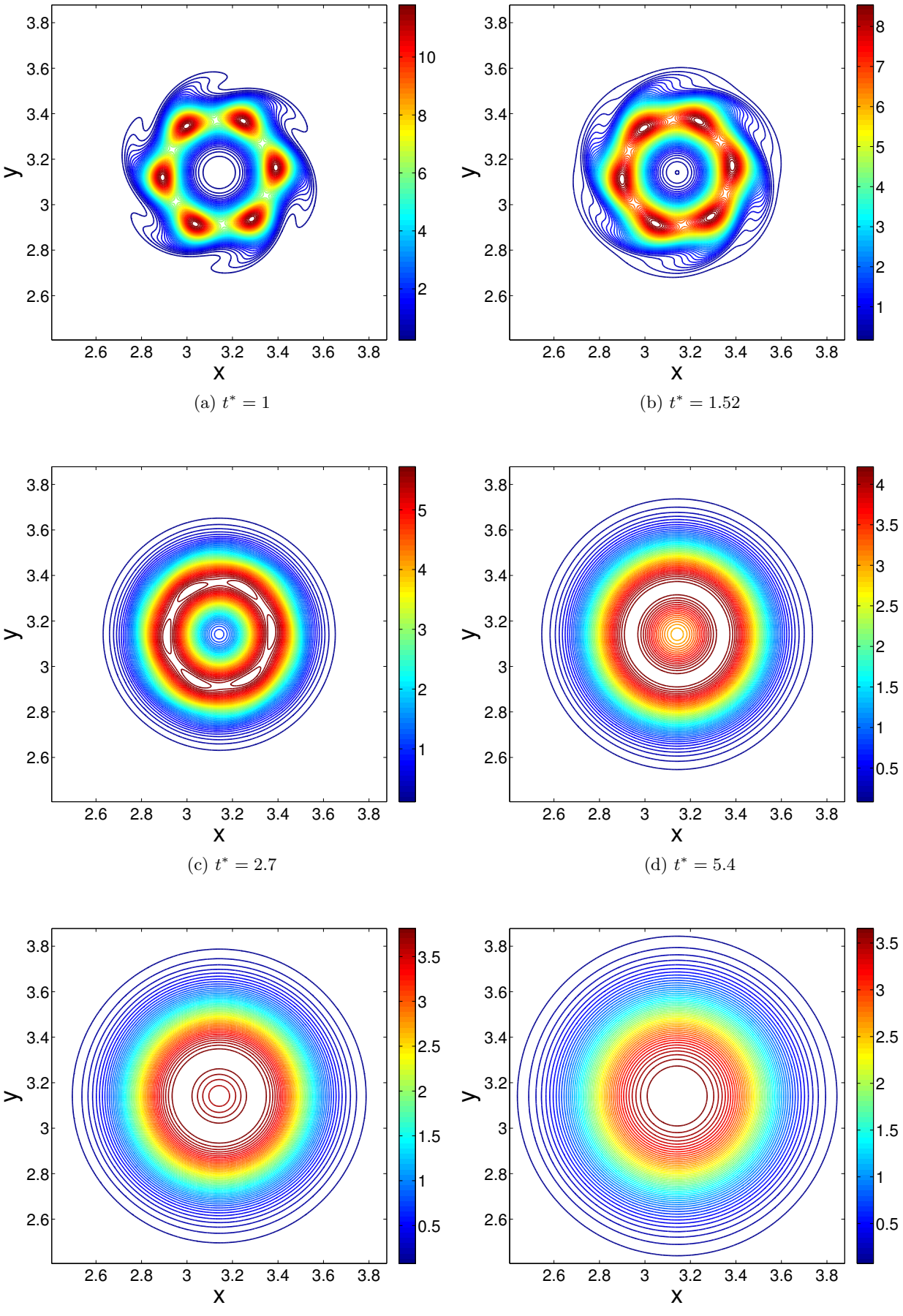

(a) $t^* = 1$

(b) $t^* = 1.52$

(c) $t^* = 2.7$

(d) $t^* = 5.4$

(e) $t^* = 7.5$

(f) $t^* = 10.47$

Figure 3.13: Viscous evolution of 6 gaussian vortices with $(a/d)_i = 0.1$ and $Re_\Gamma = 4000$. Observe initial azimuthal alignment, very clean annulus, reduction in radius of annulus to form single maximum.

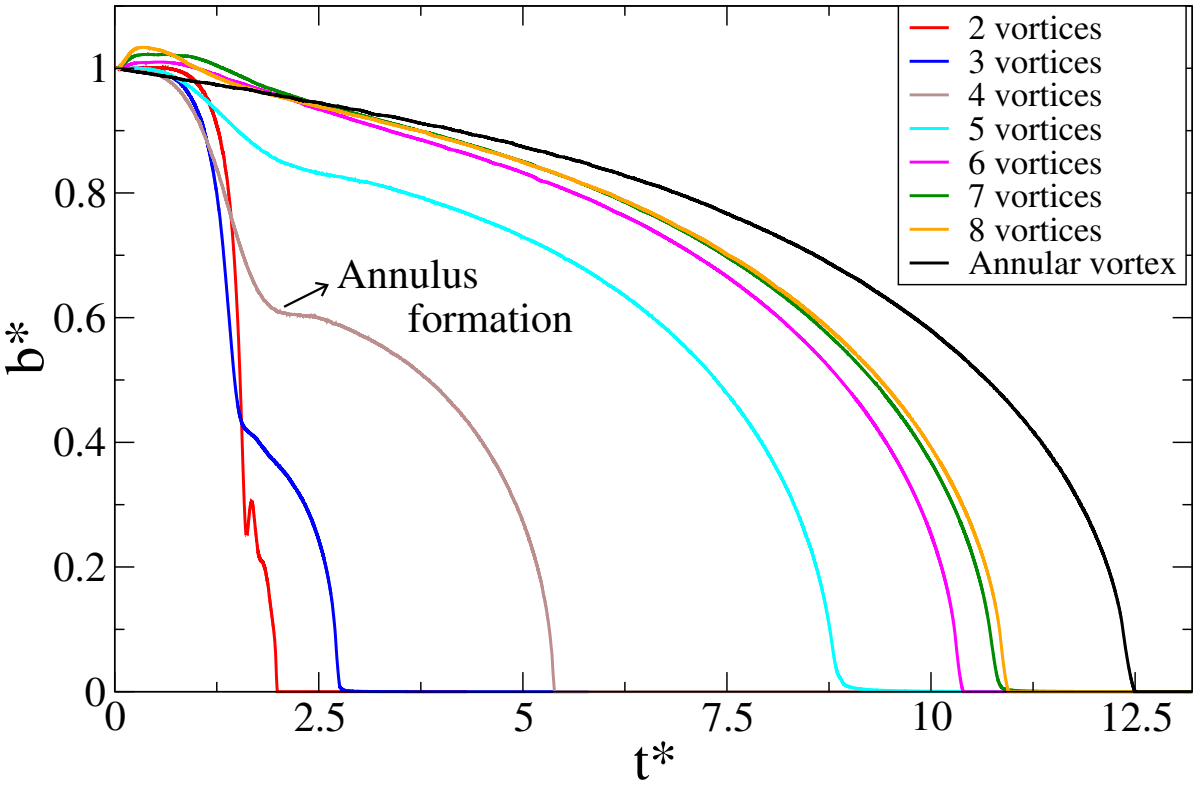

Figure 3.14: Non-dimensional separation distance b^* vs non-dimensional time t^* at $Re_\Gamma = 4000$, same $(a/d)_i = 0.1$. Starting with six or more vortices is qualitatively the same as starting with a pure annular vortex.

diffusive. We clearly observe that the annular stage dominates the merger process as we increase the number of vortices and spans the entire merger process for six and more vortices. Since the annular stage proceeds on a diffusive time scale, it is a slow stage and effectively delays the merger. It can also be seen that as we increase the number of vortices to seven and above, the process does not depend on the number of vortices. Also note that during the convective stage, the separation distance curve becomes less steep as we increase the number of vortices from two to five. In other words, the velocity at which the vortices move inward reduces as we go from two to five vortices. This is because, as we increase the number of vortices, the antisymmetric ω formed decreases (there is a reduction in filament formation), thereby decreasing the induced velocity. In the simulations above, we keep the initial Γ the same as we increase the number of vortices, and one may argue that in order to make a fair comparison between two different systems, it is the initial energy which has to be kept the same and not the initial Γ. We acknowledge this fact and have repeated the simulations keeping the initial energy the same as we change n. From Fig. 3.15, it is clear that the merger trend is similar to the one with constant initial Γ and that the annular stage once again begins to dominate the merger process as n increases and effectively delays the merger.

Next we look at the merger trend for varying Re_Γ for a particular number of vortices. We once again maintain the $(a/d)_i = 0.1$ for each of the 3 and 4 vortex cases, and find from Figs. 3.16 and 3.17, that there is a strong dependence of the final stage of merger on the Reynolds

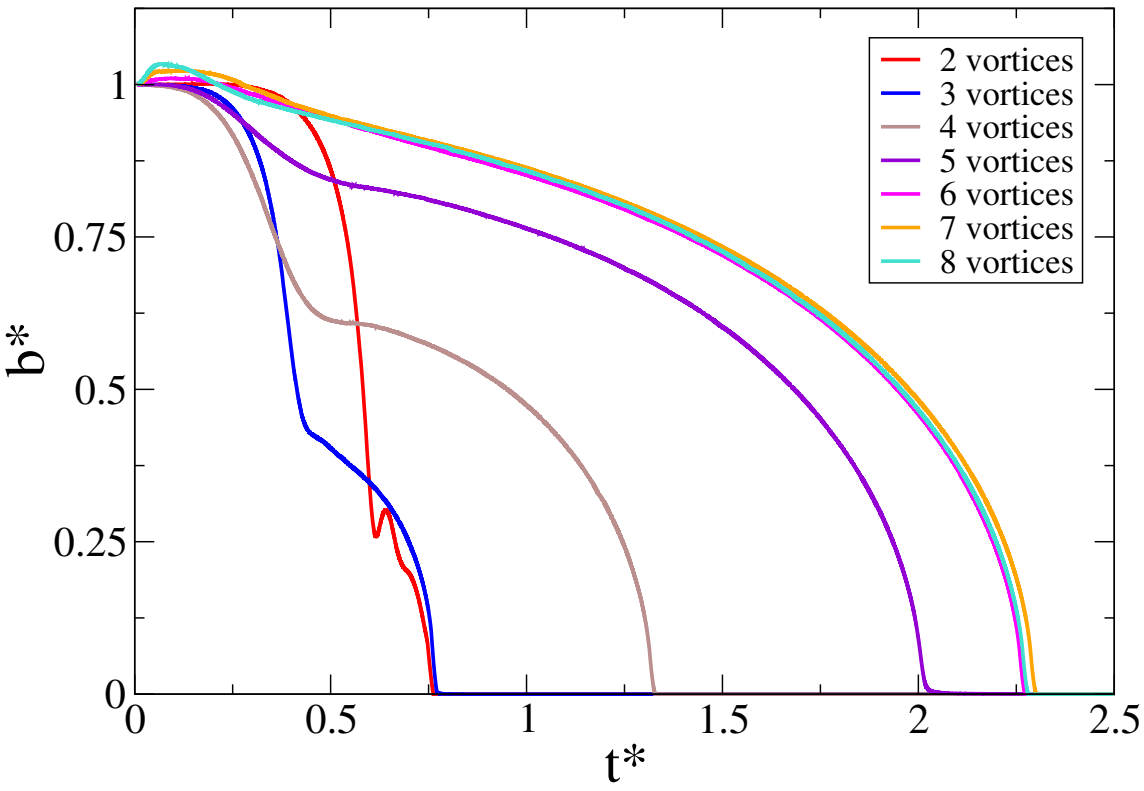

Figure 3.15: Non-dimensional separation distance b^* vs non-dimensional time t^* at $Re_{Energy} = 2366$, same $(a/d)_i = 0.1$.

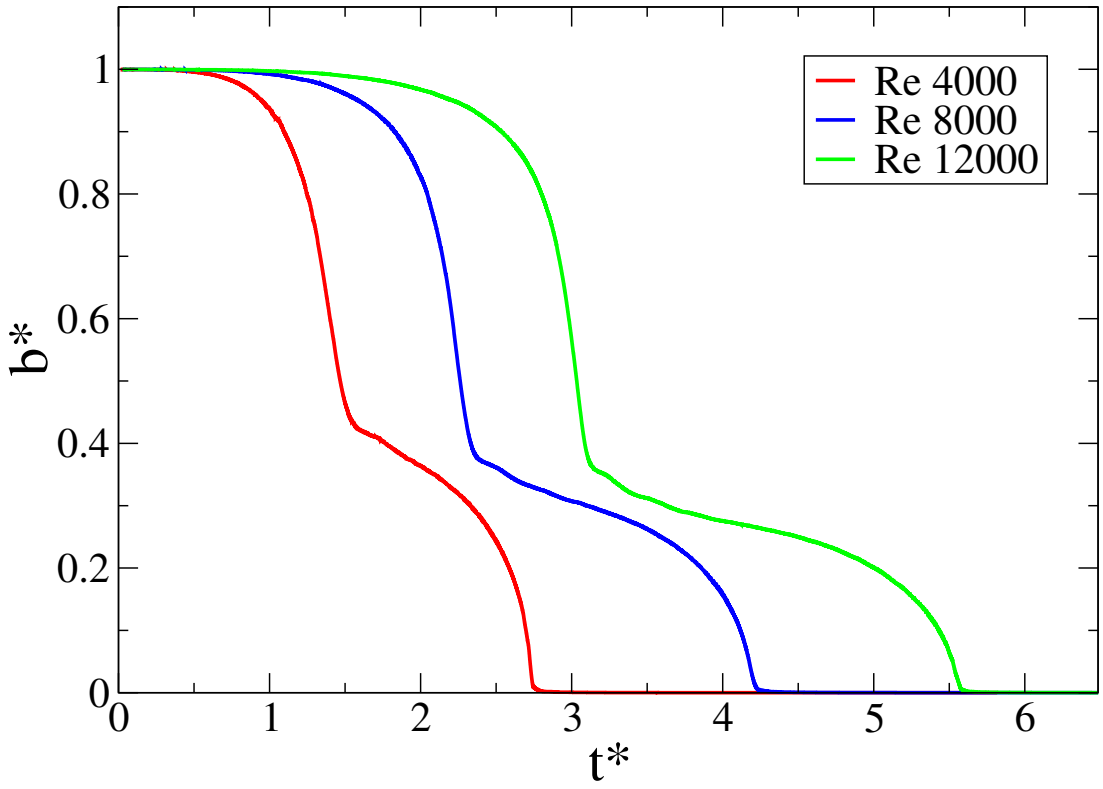

Figure 3.16: Non-dimensional separation distance b^* vs non-dimensional time t^* for 3 vortices, with varying Re_Γ, same $(a/d)_i = 0.1$.

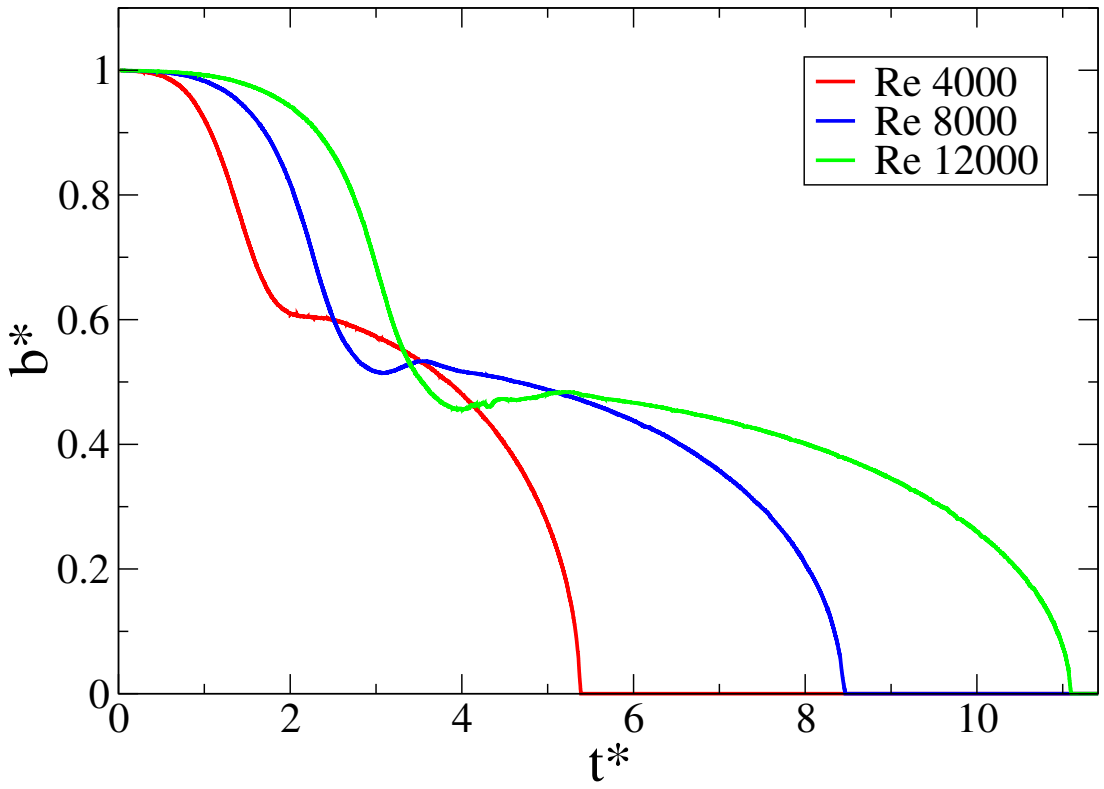

Figure 3.17: Non-dimensional separation distance b^* vs non-dimensional time t^* for 4 vortices, with varying Re_Γ, same $(a/d)_i = 0.1$.

number, suggesting that the annular stage is a diffusive stage. First it can be seen that the duration of the first diffusive stage increases as the Reynolds increases. This is expected as critical (a/d) is reached at a much later stage for higher Reynolds due to slower growth of the vortex core by diffusion. Next it can be seen that the slopes of the convective stage are the same for varying Reynolds, suggesting that this stage is more or less independent of Reynolds. But it is also observed that the durations are slightly longer with increasing Reynolds. This is due to the fact that the viscous diffusion takes place during the convective stage too. Therefore, in the case of higher Reynolds, the vortices must come closer to each other to form the annulus because of slower diffusion. Most importantly the final stage is strongly dependent on Reynolds and the curves become flatter and the time duration goes as Reynolds.

Now, we try to understand the exact reason for the reduction in radius of the annulus resulting in a single vortex maximum at the centre. At first viewing, it may seem that this reduction in radius is a convective phenomenon. However, as we have observed from the simulations, this is a slower stage. In order to clarify this, we study the evolution of an annulus as an axisymmetric problem, in polar co-ordinates.

$$\frac{\partial \omega}{\partial t} + \mathbf{u} \cdot \nabla \omega = \frac{\nu}{r}\frac{\partial \omega}{\partial r} + \nu \frac{\partial^2 \omega}{\partial r^2} \ . \tag{3.6}$$

First, from Eqn. 3.6, it is clear that the absence of u_r and $\dfrac{\partial \omega}{\partial \theta}$ arising from an axisymmetric vorticity profile of an annular vortex, would cause the non-linear term to disappear. Looking

at the viscous terms, it is evident that the $\frac{1}{r}$ term causes more diffusion towards the inside (towards the axis) than outside. Therefore, the reduction in radius of the annular vortex is just a simple linear diffusion phenomenon. A solution of Eqn. 3.6 is also shown in Fig. 4.2. It is seen that once an annulus is formed, the dynamics is governed by Eqn. 3.6.

So far, we have seen simulations in which the merger process is symmetric and all the vortices move inward in the same way. This has been the case for lower Reynolds numbers like $Re_\Gamma = 4000$ and $Re_\Gamma = 8000$. We remember from chapter 1 however, that for many point and patch vortices on the vertices of a polygon form an unstable mean flow. Clearly this is being stabilized by viscosity. We wish to see whether the picture changes at higher Reynolds numbers. As expected, simulations at higher Reynolds such as $Re_\Gamma = 12000$ in systems with five or more vortices begin to show asymmetric merger. One such example is the eight-vortex simulation at $Re_\Gamma = 12000$ and $(a/d)_i = 0.1$ shown in Figs. 3.18 and 3.19. Here, it is observed initially that the eight vortices diffuse out to form an annulus-like structure. However, there are vorticity maxima within the annulus which are still persistent. On close viewing, it can be seen that the eight vortices merge (diffuse) to form four maxima which further go on to merge to form two maxima. Although initially the viscous diffusion tries to smoothen out the two maxima to an annular vortex, they reappear to form a tripole which can be thought of as an $m = 2$ azimuthal mode instability of the annular vortex. Viscosity however wins in this case and the tripolar state diffuses out to form a single vortex maximum. Thus, at low Re, we find symmetric merger of multiple vortices and at high Re we are able to observe asymmetric merger.

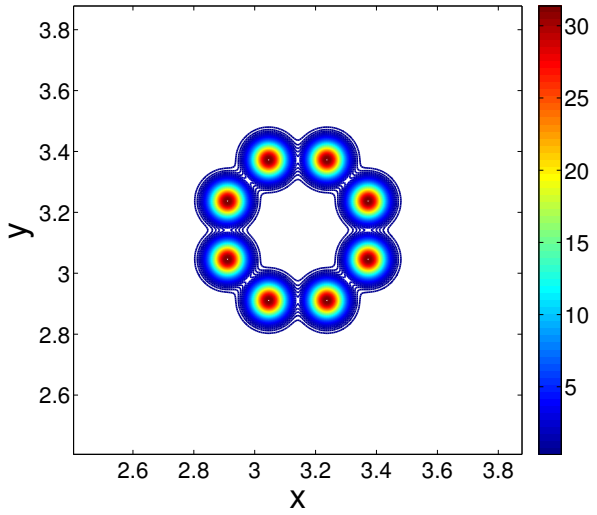

(a) $t^* = 0$

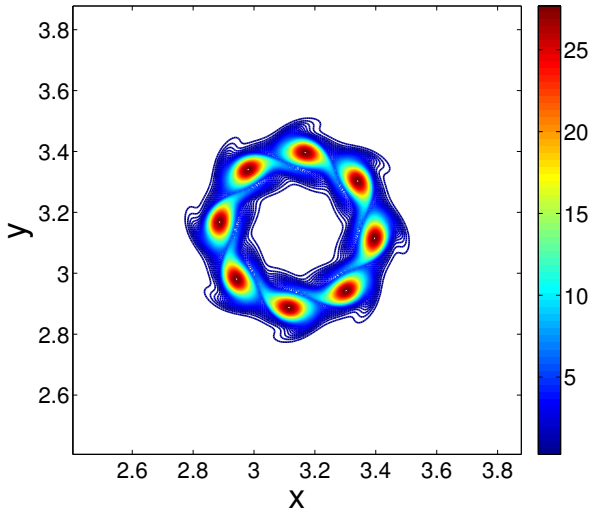

(b) $t^* = 0.1685$

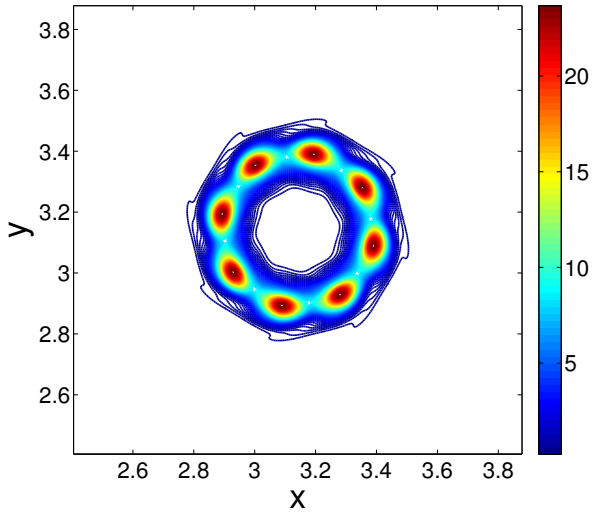

(c) $t^* = 0.39$

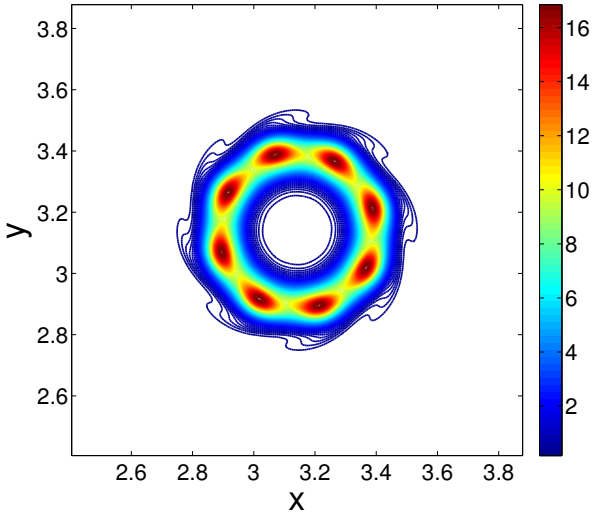

(d) $t^* = 0.9486$

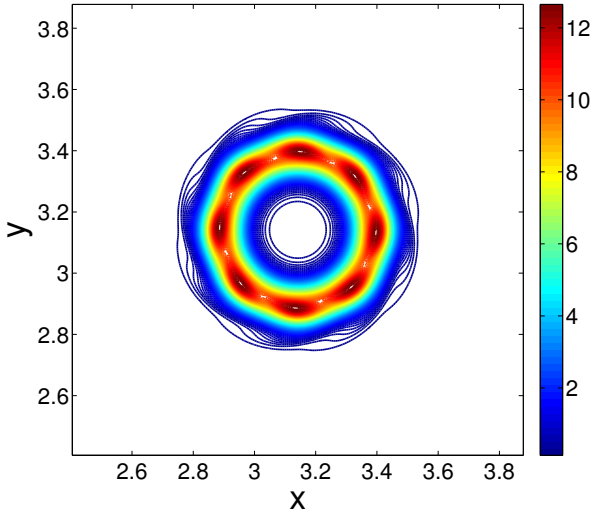

(e) $t^* = 1.4983$

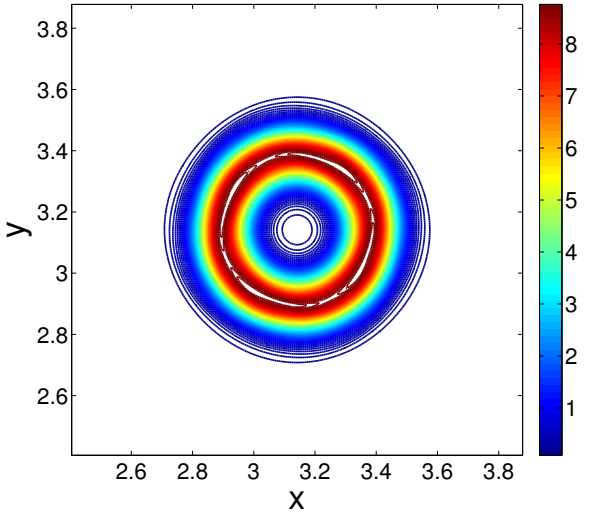

(f) $t^* = 2.837$

Figure 3.18: Viscous evolution of 8 gaussian vortices with $(a/d)_i = 0.1$ and $Re_\Gamma = 12000$.

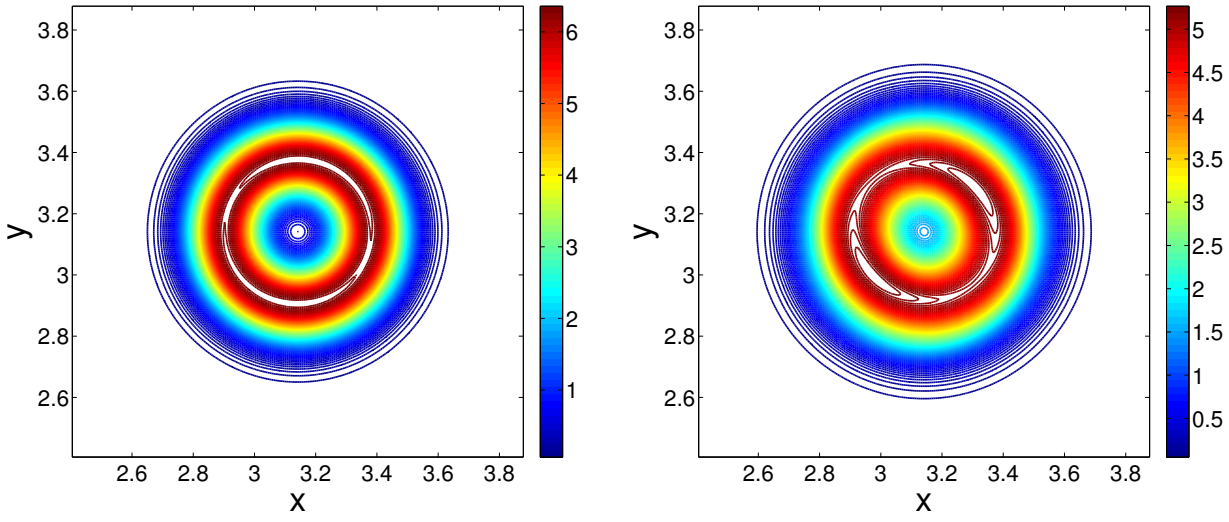

(a) $t^* = 6.1616$

(b) $t^* = 10.0447$

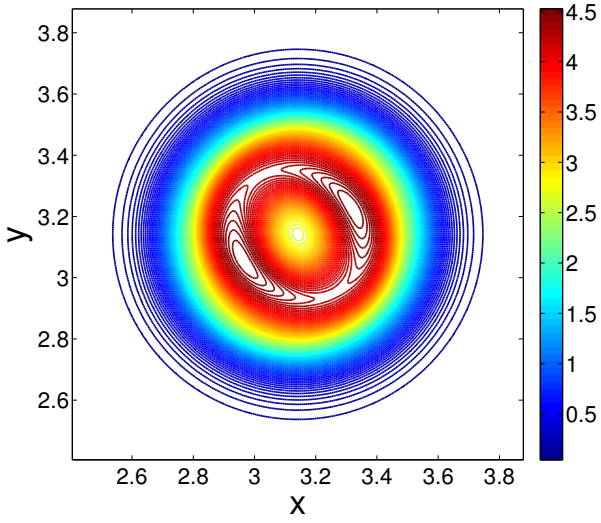

(c) $t^* = 15.2665$

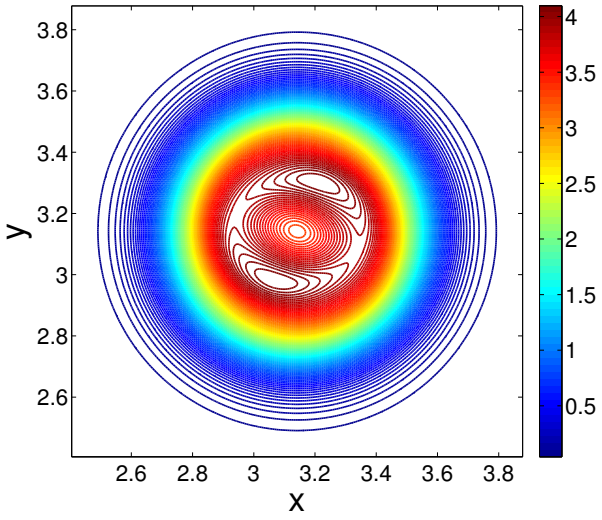

(d) $t^* = 20.1515$

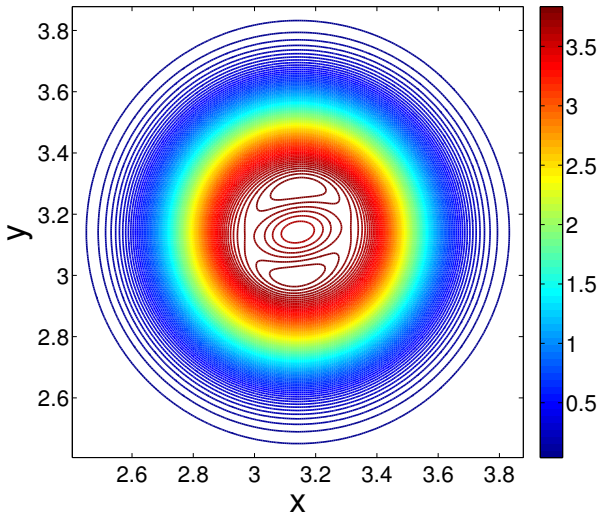

(e) $t^* = 25.0276$

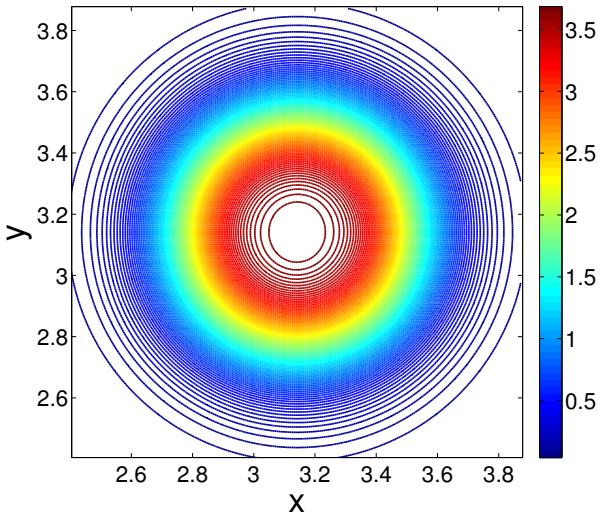

(f) $t^* = 33.574$

Figure 3.19: Viscous evolution of 8 gaussian vortices with $(a/d)_i = 0.1$ and $Re_\Gamma = 12000$ - Continued. Observe the tripolar vortex indicating an $m = 2$ mode instability.

3.4 Conclusion

With the help of a pseudo-spectral code, we studied the merger of n equal co-rotating vortices (n varying from 2 to 8), arranged at equal intervals on the circumference of a circle, for a viscous homogeneous flow. We find a new stage in the merger of multiple (three or more) vortices - an annulus which is long-lived. This stage, which is absent in the two-vortex merger, appears mainly because of the presence of a central region of fluid flow in the streamlines observed in the co-rotating frame for three or more vortices. Also, this stage evolves on a diffusive time scale and involves the reduction in radius of an annular vortex by a simple diffusion process to form one single vortex maximum.

We also observe a quantitative and quantitative change in the separation distance as we go from two to six vortices. The second diffusive stage in the two-vortex merger gives way to an annular stage from three onwards. In fact, this stage begins to dominate the merger process as we proceed from three to six vortices, where it is observed that the convective stage completely disappears. Thus the annulus begins to dominate the merger process as we increase the number of vortices and effectively delays the merger, as it then proceeds slowly due to radial diffusion. We attribute the change in separation distance history to a change in the vortex tilt history as the number of vortices increases from two to six. For three, four and five vortices, we observe that the vortices initially align themselves radially with a slight tilt towards the radius vector. This deformation and alignment, attributed to the strain field of the vortex systems, places vorticity in the exchange band and outer recirculation (filaments) regions giving rise to antisymmetric vorticity. It is this antisymmetric vorticity which induces a velocity and pushes the vortices radially inward. Towards the end of the convective stage, we find that the vortices realign themselves azimuthally to aid in the formation of an annulus. As the number of vortices increases from three to five, the radius at which the annulus is formed also increases, which is expected. However, for systems with six and more vortices, the vortices even at short times align themselves azimuthally due to the strain field, assisting in the formation of an annular vortex and thus leading to the absence of the convective stage. In essence, the tilt history changes, whereas the merger mechanism remains the same.

In addition to this, we also find the annulus to be more stable at low Re where we are able to observe symmetric merger in which all the vortices move inwards in the same fashion. At high Re, we observe asymmetric merger and even instabilities setting in leading to the breakup of the annular vortex. Analyzing such a problem using DNS can can be costly and thus, this necessitates a viscous stability analysis of the annular vortex, which we deal with in the coming chapters.

Chapter 4

Viscous Evolution of a Cylindrical vortex sheet

4.1 Scope

Our objective in this chapter is to see whether there exists a vortex of cylindrical structure, which is axisymmetric, i.e vorticity pointing outside the plane which is a function of the radial coordinate alone. We find that the Navier-Stokes equations do support such an annular vortex, with its maximum vorticity at the radial location r_{max}. We call this a generalized Lamb-Oseen vortex, since the Lamb-Oseen is the limiting case of an annular vortex, with $r_{max} = 0$. We find that any cylindrical vortex will diffuse inwards, i.e r_{max} reduces with time, until it adopts a classical Lamb-Oseen form at a large time. We utilize Laplace transforms to convert a PDE in space and time, into an ODE in space, and solve the problem using variation of parameters. It must be noted that this problem can even be solved using other techniques such as Fourier transform, Hankel transform, etc.

4.2 Formulation and solution

Consider the two-dimensional vorticity equation in cylindrical co-ordinates obtained by taking the curl of the Navier-Stokes equations. Assuming symmetry in the azimuthal direction $\left(\frac{\partial\,(anything)}{\partial\theta} = 0\right)$, and zero radial velocity ($u_r = 0$), we can drop the non-linear term ($u.\nabla\omega$) and simplify the viscous term to obtain

$$\frac{\partial\omega}{\partial t} = \frac{\nu}{r}\frac{\partial}{\partial r}\left(r\frac{\partial\omega}{\partial r}\right) \ , \tag{4.1}$$

where ω is the axial vorticity and ν is the kinematic viscosity. The initial condition prescribed is that of a cylindrical vortex sheet at a radius a with a total circulation of Γ_o, as follows :

$$\omega\,(r,0) = \omega_o = \frac{\Gamma_o}{2\pi}\frac{\delta\,(r-a)}{r} = f\,(r) \ . \tag{4.2}$$

From symmetry we have

$$\frac{\partial\omega\,(0,t)}{\partial r} = 0 \ . \tag{4.3}$$

We also consider the farfield to be a vorticity-free one, i.e

$$\omega\,(r\to\infty,t)\to 0 \ . \tag{4.4}$$

Now we define the Laplace transform as

$$L\{\omega(t)\} = \hat{\omega}(s) = \int_0^\infty \omega(t)\, e^{-st}\, dt \ . \tag{4.5}$$

Taking the Laplace transform in time of Eqs. 4.1, 4.3, 4.4 and using the Eq. 4.2 as the initial condition,we get the following equation set

$$\frac{d^2\hat{\omega}}{dr^2} + \frac{1}{r}\frac{d\hat{\omega}}{dr} - \frac{s\hat{\omega}}{\nu} = -\frac{\omega_o}{\nu} = f(r) \ , \tag{4.6}$$

$$\frac{d\hat{\omega}(0,s)}{dr} = 0 \ , \tag{4.7}$$

$$\hat{\omega}(r \to \infty, s) \to 0 \ , \tag{4.8}$$

where $\hat{\omega}$ is the laplace transform, defined in the standard way as append A. To solve the above set, we first find the solution to the homogeneous equation

$$\frac{d^2\hat{\omega}_h}{dr^2} + \frac{1}{r}\frac{d\hat{\omega}_h}{dr} - \frac{s\hat{\omega}_h}{\nu} = 0 \ . \tag{4.9}$$

Putting $y \equiv r\sqrt{\frac{s}{\nu}}$, we get

$$y^2\frac{d^2\hat{\omega}_h}{dy^2} + y\frac{d\hat{\omega}_h}{dy} - \left(n^2 + y^2\right)\hat{\omega}_h = 0, \quad \text{where} \quad n = 0 \ . \tag{4.10}$$

This is a modified form of the Bessel equation to which the solution can be expressed as a linear combination of the modified Bessel functions I_n and K_n, n being the order of the Bessel function. We thus have

$$\hat{\omega}_h = c_1 I_0(y) + c_2 K_0(y) \ , \tag{4.11}$$

where I_0 and K_0 are given by Abramowitz & Stegun (1965):

$$I_0(y) = 1 + \frac{\frac{y^2}{4}}{(1!)^2} + \frac{\frac{(y^2)^2}{4}}{(2!)^2} + \frac{\frac{(y^2)^3}{4}}{(3!)^2} + \dots \ , \tag{4.12}$$

$$K_0(y) = -\{\ln(z/2) + \gamma\} I_0(y) + \frac{\frac{y^2}{4}}{(1!)^2} + \left(1 + \frac{1}{2}\right)\frac{\frac{(y^2)^2}{4}}{(2!)^2} + \left(1 + \frac{1}{2} + \frac{1}{3}\right)\frac{\frac{(y^2)^3}{4}}{(3!)^2} + \dots \ , \tag{4.13}$$

By using the method of variation of parameters, we get the particular solution as

$$\hat{\omega}_p = -I_0\left(r\sqrt{\frac{s}{\nu}}\right)\int_0^r \frac{f(r')\, K_0\left(r'\sqrt{\frac{s}{\nu}}\right)}{W(r')}\, dr' + K_0\left(r\sqrt{\frac{s}{\nu}}\right)\int_0^r \frac{f(r')\, I_0\left(r'\sqrt{\frac{s}{\nu}}\right)}{W(r')}\, dr' \ , \tag{4.14}$$

where $W(r)$ is the Wronskian given by

$$W(r) = I_0\left(r\sqrt{\frac{s}{\nu}}\right) K_1\left(r\sqrt{\frac{s}{\nu}}\right) - I_0\left(r\sqrt{\frac{s}{\nu}}\right) I_1\left(r\sqrt{\frac{s}{\nu}}\right) = -\frac{1}{r} \ . \tag{4.15}$$

The complete solution is given by $\hat{\omega} = \hat{\omega}_h + \hat{\omega}_p$, i.e

$$\hat{\omega} = c_1 I_0\left(r\sqrt{\frac{s}{\nu}}\right) + c_2 K_0\left(r\sqrt{\frac{s}{\nu}}\right)$$
$$-I_0\left(r\sqrt{\frac{s}{\nu}}\right)\int_0^r \frac{f(r')\,K_0\left(r'\sqrt{\frac{s}{\nu}}\right)}{W(r')}\,dr' + K_0\left(r\sqrt{\frac{s}{\nu}}\right)\int_0^r \frac{f(r')\,I_0\left(r'\sqrt{\frac{s}{\nu}}\right)}{W(r')}\,dr' \ . \tag{4.16}$$

Now we apply the boundary conditions. At $r = 0$, we find that $K_0(0)$ is divergent. In order for $\hat{\omega}$ to be well-defined, c_2 must be 0. Next, since $\hat{\omega} \to 0$ as $r \to \infty$, we get

$$\lim_{r\to\infty}\left\{c_1 - \int_0^r \frac{f(r')\,K_0\left(r'\sqrt{\frac{s}{\nu}}\right)}{W(r')}\,dr'\right\} I_0\left(r\sqrt{\frac{s}{\nu}}\right) = 0 \ . \tag{4.17}$$

Since $I_0\left(r\sqrt{\frac{s}{\nu}}\right)$ is divergent at $r \to \infty$, the only way eqn (17) can be satisfied is if

$$c_1 = \int_0^\infty \frac{f(r')\,K_0\left(r'\sqrt{\frac{s}{\nu}}\right)}{W(r')}\,dr' \ . \tag{4.18}$$

We therefore have

$$\hat{\omega} = I_0\left(r\sqrt{\frac{s}{\nu}}\right)\int_r^\infty \frac{f(r')\,K_0\left(r'\sqrt{\frac{s}{\nu}}\right)}{W(r')}\,dr' + K_0\left(r\sqrt{\frac{s}{\nu}}\right)\int_0^r \frac{f(r')\,I_0\left(r'\sqrt{\frac{s}{\nu}}\right)}{W(r')}\,dr' \ . \tag{4.19}$$

Now, substituting for $f(r')$ from Eq. 4.2 into eq. 4.19, we get

$$\hat{\omega} = \begin{cases} \dfrac{\Gamma_o}{2\pi\nu} I_0\left(r\sqrt{\dfrac{s}{\nu}}\right) K_0\left(a\sqrt{\dfrac{s}{\nu}}\right) & \text{for } r \le a \ , \\ \dfrac{\Gamma_o}{2\pi\nu} I_0\left(a\sqrt{\dfrac{s}{\nu}}\right) K_0\left(r\sqrt{\dfrac{s}{\nu}}\right) & \text{for } r > a \ . \end{cases} \tag{4.20}$$

It must be noted that we did not have to use the symmetry condition (Eq. 4.7) to obtain Eq. 4.20. It can be seen that this condition (Eq. 4.7) is automatically satisfied by Eq. 4.20. Taking the inverse Laplace transform of the convolution in the above expression, and using the following standard result from Erdélyi (1954),

$$L^{-1}\left\{K_n\left[\sqrt{s}\left(\sqrt{\alpha}+\sqrt{\beta}\right)\right] I_n\left[\sqrt{s}\left(\sqrt{\alpha}-\sqrt{\beta}\right)\right]\right\} = \frac{1}{2t} e^{-\left(\frac{\alpha+\beta}{2t}\right)} I_n\left\{\frac{\alpha+\beta}{2t}\right\} \ , \tag{4.21}$$

we get

$$\omega = \frac{\Gamma_o}{4\pi\nu t} e^{-\left(\frac{a^2+r^2}{4\nu t}\right)} I_0\left\{\frac{ar}{2\nu t}\right\} \ . \tag{4.22}$$

This is a generalized form of the Lamb-Oseen vortex. Note that this is not a similarity solution as we have a natural length scale (a) in the problem. The Lamb-Oseen vortex, which is a similarity solution, is obtained by putting $a = 0$ (initial condition of a line vortex), to get

$$\omega = \frac{\Gamma_o}{4\pi\nu t} e^{-\left(\frac{r^2}{4\nu t}\right)} \ . \tag{4.23}$$

Now, in addition to the solution given by Eq. 4.22, we can find other solutions for cylindrical vortices which satisfy the Navier-Stokes, by differentiating Eq. 4.22 with respect to time t. However, we will only consider the first solution obtained, which has a finite circulation associated with it. We will now look at some interesting features of the Generalized Lamb-Oseen vortex.

For $t \to 0$, we expect the vortex to diffuse symmetrically about $r = a$. Let $y = ar/(2\nu t)$. As $t \to 0$, $y \to \infty$ and at leading order,

$$I_0(y) = \frac{e^y}{\sqrt{2\pi y}} = \frac{e^{\frac{ar}{2\nu t}}}{\sqrt{\frac{\pi ar}{\nu t}}} \,. \tag{4.24}$$

Also, we can consider $r = a + \epsilon + \epsilon^2 + \ldots$ and write $ar \sim a^2$ at leading order. Using this asymptotic approximation and Eq. 4.24 in Eq. 4.22, we get

$$\omega = \frac{\Gamma_o}{4\pi\sqrt{\pi\nu tar}} e^{-\frac{(r-a)^2}{4\nu t}} = \frac{\Gamma_o}{4\pi a\sqrt{\pi\nu t}} e^{-\frac{\epsilon^2}{4\nu t}} \,. \tag{4.25}$$

Note that this is a similarity solution and is similar to the diffusion of a planar vortex sheet, which is as expected.

4.2.1 Evolution of vorticity maximum

Now we track the vorticity maximum (ω_{max}) to understand how the annular vortex diffuses inward reducing in radius to ultimately evolve into a regular gaussian or the Lamb-Oseen vortex. Applying $\dfrac{\partial \omega}{\partial r} = 0$ to Eq. 4.22, we get

$$r_{max} I_0(y) = a I_1(y), \quad \text{where} \quad y = \left(\frac{a r_{max}}{2\nu t}\right) \,. \tag{4.26}$$

This can be solved numerically. In addition, we can also find the asymptotic behavior when $t \to 0$, and at $r_{max} \to 0$.

When $t \to 0$, $y \to \infty$, and

$$I_o(y) \sim \frac{e^y}{\sqrt{2\pi y}}\left(1 + \frac{1}{8y}\right), \qquad I_1(y) \sim \frac{e^y}{\sqrt{2\pi y}}\left(1 - \frac{3}{8y}\right) \,. \tag{4.27}$$

We therefore get

$$r_{max} = \frac{(4a^2 - \nu t) + \sqrt{16a^4 + \nu^2 t^2 - 56a^2\nu t}}{8a}, \text{when} \quad t \to 0 \,. \tag{4.28}$$

When $r_{max} \to 0$, $y \to 0$, and

$$I_o(y) \sim \left(1 + \frac{y^2}{4}\right), \qquad I_1(y) \sim \left(\frac{y}{2} + \frac{y^3}{16}\right) \,. \tag{4.29}$$

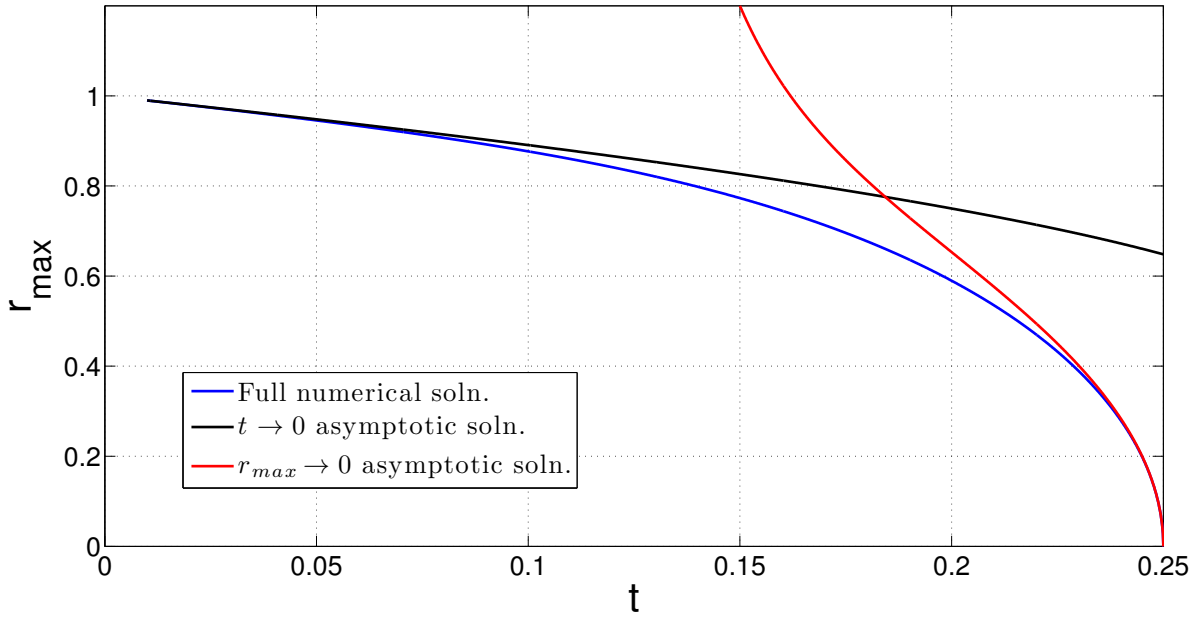

Figure 4.1: Evolution of position of vorticity maximum r_{max} with time t, for $a = 1$ and $\nu = 1$.

Therefore, we get

$$r_{max} = \frac{4\nu t}{a}\sqrt{\frac{\frac{a^2}{4\nu} - t}{t - \frac{a^2}{8\nu}}}, \quad \text{when} \quad r_{max} \to 0 \ . \tag{4.30}$$

From this it is clear that we can pick out a time scale for the vorticity maximum to reach the center (axis).

$$T|_{(r_{max}=0)} = \frac{a^2}{4\nu} \ . \tag{4.31}$$

At any time less than this, the vorticity has a maximum away from the axis. Beyond this time, the vorticity is a monotonically reducing quantity, radially.

Fig. 4.1 contains plots for Eqs. 4.26, 4.28 and 4.30. Here it can be seen that initially, the vorticity maximum moves inward in a ballistic manner. Later on its behavior is different as the thickness of the annulus increases, and finally the vorticity maximum hits the axis after a time scale corresponding to Eq. 4.31.

4.2.2 Validation with pseudo-spectral code

To further validate the obtained analytical expression for the generalized gaussian vortex, we input the vorticity profile as the initial condition in our 2D pseudo-spectral code previously discussed. To compare the analytical result with the numerical one, we take a section of the vorticity profile from the 2D numerical result and plot its evolution with time for a particular set of initial conditions. We superimpose the profile obtained from the 2D pseudo-spectral code

with that from the analytical result and observe that the two plots are a perfect match (Fig. 4.2). It must be noted that we never switched off the non-linear terms in the pseudo-spectral code while running it. The symmetry of profile automatically removes the non-linear advective terms as it should.

4.2.3 Circulation and velocity

The circulation associated with the generalized Lamb-Oseen is given by

$$\Gamma(r) = \int_A \omega \cdot \, dA = 2\pi \int_0^r r\omega \, dr \ . \tag{4.32}$$

Therefore total circulation

$$\Gamma(\infty) = 2\pi \int_0^\infty r\omega \, dr = \Gamma_o \ . \tag{4.33}$$

However, we have not been able to arrive at a closed form expression for $\Gamma(r)$, and hence the azimuthal velocity, which is given by $U_\theta = \dfrac{\Gamma}{2\pi r}$. The velocity can be calculated with the help of a numerical integration technique such as gaussian quadrature. At the same time, it is useful to note the asymptotic behavior of U_θ as $r \to 0$ and ∞. As $r \to \infty$, it is evident from Eq. 4.33 that $U_\theta \sim \dfrac{1}{r}$. For $r \to 0$ asymptotic limit, we write out the leading order terms of ω in Eq. 4.22 as

$$\omega = \frac{\Gamma_o}{4\pi\nu t} e^{-\left(\frac{a^2}{4\nu t}\right)} \left\{ 1 + \frac{r^2\left(a^2 - \nu t\right)}{4\nu^2 t^2} + \cdots \right. \tag{4.34}$$

From Eqs. 4.32 and 4.34, it is evident that as $r \to 0$, $\Gamma \sim r^2$, and hence $U_\theta \sim r$.

4.3 Conclusion

Thus, we have obtained an analytical expression for a generalized Lamb-Oseen vortex which is a solution of the Navier-Stokes equations, with the initial condition of a cylindrical vortex sheet. We find that this shows short time (planar vortex sheet) and long time (regular Lamb-Oseen or gaussian vortex) similarity solutions. More importantly, the annular vortex obtained reduces in radius by pure diffusion and ultimately evolves into a regular gaussian vortex. Next, we will perform a linear stability analysis of this vorticity profile frozen at a given instant of time.

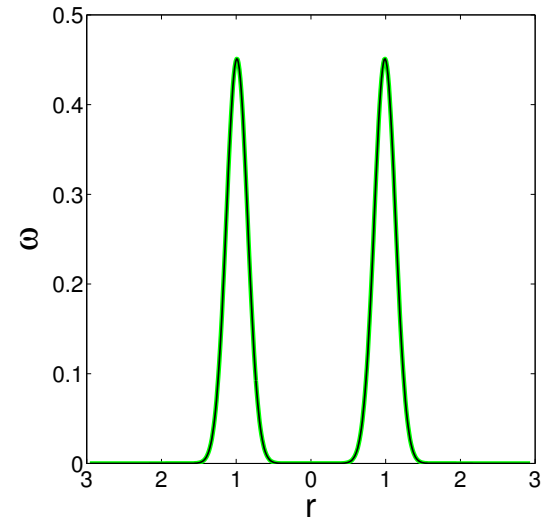

(a) $t = 10$

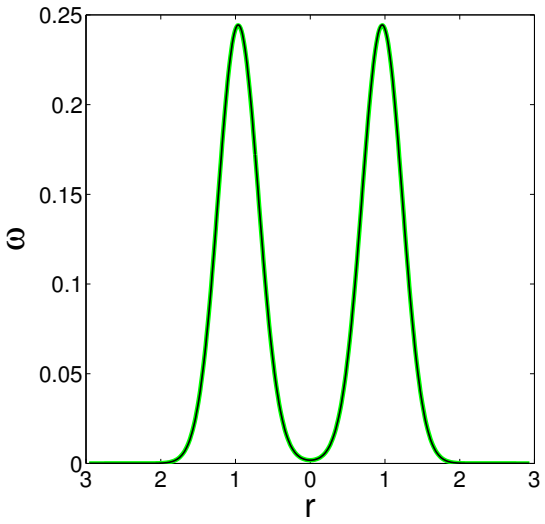

(b) $t = 35$

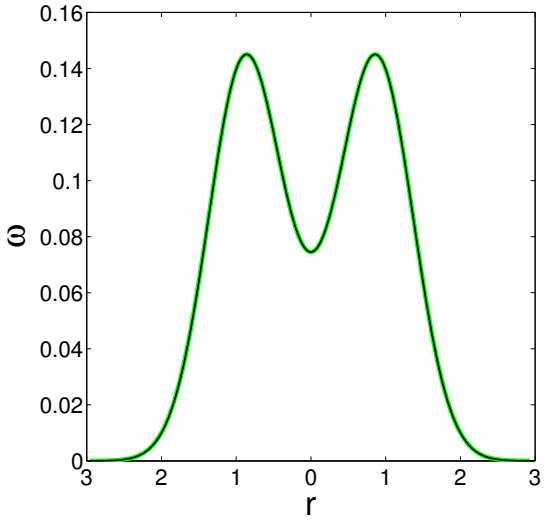

(c) $t = 110$

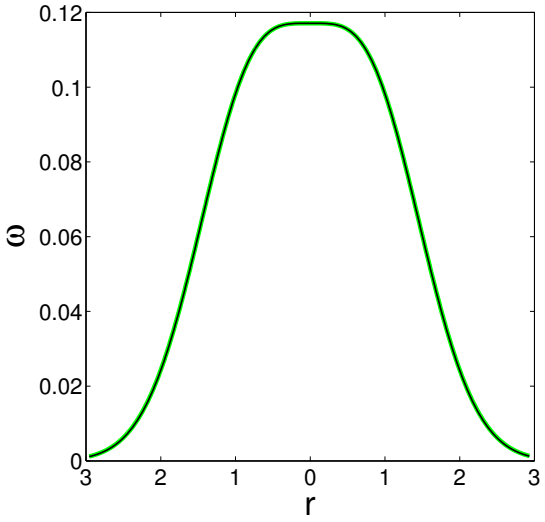

(d) $t = 250$

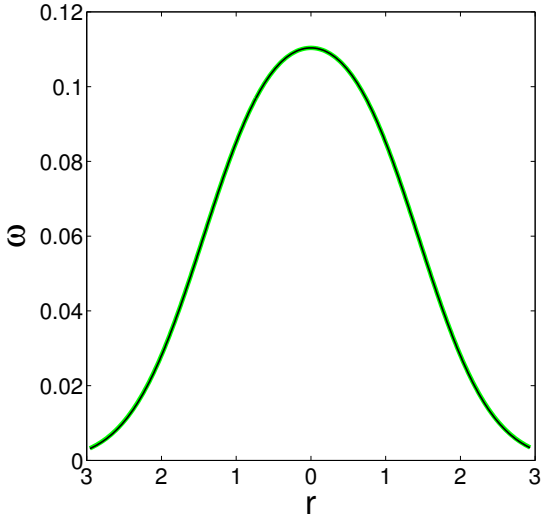

(e) $t = 360$

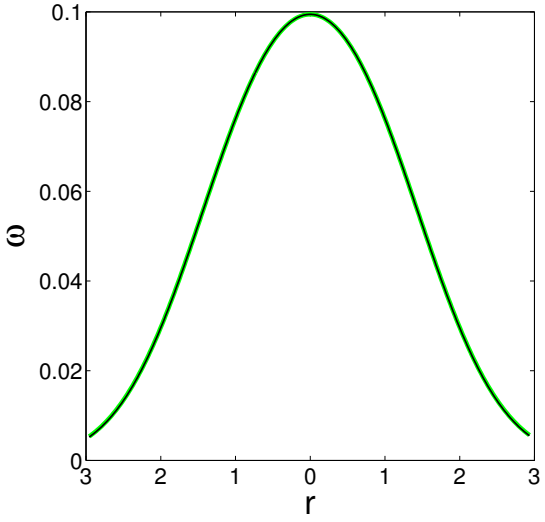

(f) $t = 470$

Figure 4.2: Validation of analytical result (black line) with pseudo-spectral code (green line), for an initial condition ($\nu t = 0.01$, $\Gamma_o = 1$) of a generalized Lamb-Oseen vortex (cylindrical vortex sheet at $t = 0$).

Chapter 5

Linear stability analysis of annular vortex: Formulation and numerical technique

5.1 Scope

In this chapter, we carry out a quasi-steady linear stability analysis of an annular vortex. We systematically derive the stability equations using a standard technique and obtain a set of ordinary differential equations. We employ a Chebyshev collocation technique to discretize the ensuing set of differential equations, which can then be formulated as an eigenvalue problem. Some of the important properties of the Chebyshev interpolation technique used are also discussed.

5.2 Formulation and solution-2D perturbations

Consider the two-dimensional continuity and Navier-Stokes equations for an incompressible homogenous fluid in plane polar co-ordinates:

$$\frac{1}{r}\frac{\partial}{\partial r}\left(ru_r\right)+\frac{1}{r}\frac{\partial}{\partial \theta}\left(u_\theta\right)=0\ , \tag{5.1}$$

$$\frac{\partial u_r}{\partial t}+u_r\frac{\partial u_r}{\partial r}+\frac{u_\theta}{r}\frac{\partial u_r}{\partial \theta}-\frac{u_\theta^2}{r}=-\frac{1}{\rho}\frac{\partial p}{\partial r}+\frac{1}{Re}\left(\nabla^2 u_r-\frac{u_r}{r^2}-\frac{2}{r^2}\frac{\partial u_\theta}{\partial \theta}\right)\ , \tag{5.2}$$

$$\frac{\partial u_\theta}{\partial t}+u_r\frac{\partial u_\theta}{\partial r}+\frac{u_\theta}{r}\frac{\partial u_\theta}{\partial \theta}+\frac{u_r u_\theta}{r}=-\frac{1}{\rho r}\frac{\partial p}{\partial \theta}+\frac{1}{Re}\left(\nabla^2 u_\theta+\frac{2}{r^2}\frac{\partial u_r}{\partial \theta}-\frac{u_\theta}{r^2}\right)\ , \tag{5.3}$$

where

$$\nabla^2=\frac{1}{r}\frac{\partial}{\partial r}\left(r\frac{\partial}{\partial r}\right)+\frac{1}{r^2}\frac{\partial^2}{\partial \theta^2}\ . \tag{5.4}$$

We decompose the total motion into a background state plus perturbations, as

$$u_{r_{tot}}=U_r+\tilde{u}_r\ , \tag{5.5}$$

$$u_{\theta_{tot}}=U_\theta+\tilde{u}_\theta\ , \tag{5.6}$$

$$p_{tot}=P+\tilde{p}\ , \tag{5.7}$$

where the variables with tildes ($\tilde{}$) denote the perturbations. Substituting the background state and the total motion separately into Eqs. 5.1,5.2 and 5.3, we obtain equations for the base state and the total motion respectively. Subtracting the equation for the background state from the

equations for the total motion, we obtain a set of equations for the perturbations. Neglecting non-linear terms in the perturbations, we finally get

$$\frac{1}{r}\frac{\partial}{\partial r}\left(r\tilde{u}_r\right)+\frac{1}{r}\frac{\partial}{\partial\theta}\left(\tilde{u}_\theta\right)=0\ , \tag{5.8}$$

$$\frac{\partial\tilde{u}_r}{\partial t}+\frac{U_\theta}{r}\frac{\partial\tilde{u}_r}{\partial\theta}-\frac{2U_\theta\tilde{u}_\theta}{r}=-\frac{1}{\rho}\frac{\partial\tilde{p}}{\partial r}+\frac{1}{Re}\left(\nabla^2\tilde{u}_r-\frac{\tilde{u}_r}{r^2}-\frac{2}{r^2}\frac{\partial\tilde{u}_\theta}{\partial\theta}\right)\ , \tag{5.9}$$

$$\frac{\partial\tilde{u}_\theta}{\partial t}+\tilde{u}_r\frac{\partial U_\theta}{\partial r}+\frac{U_\theta}{r}\frac{\partial\tilde{u}_\theta}{\partial\theta}+\frac{\tilde{u}_rU_\theta}{r}=-\frac{1}{\rho r}\frac{\partial\tilde{p}}{\partial\theta}+\frac{1}{Re}\left(\nabla^2\tilde{u}_\theta+\frac{2}{r^2}\frac{\partial\tilde{u}_r}{\partial\theta}-\frac{\tilde{u}_\theta}{r^2}\right)\ . \tag{5.10}$$

Assuming the perturbations or infinitesimal disturbances to be of the normal mode form in θ and t, characterized by an azimuthal wavenumber m and a complex frequency f :

$$\{\tilde{u}_r,\tilde{u}_\theta,\tilde{p}\}=\{\hat{u}_r\left(r\right),\hat{u}_\theta\left(r\right),\hat{p}\left(r\right)\}e^{i(m\theta-ft)}\ , \tag{5.11}$$

and substituting Eq. 5.11 in the Eqs. 5.8 to 5.10, we obtain a set of ordinary differential equations. Eliminating $\hat{p}$ and $\hat{u_\theta}$ from the set of ODE's, we are left with a single ODE in $\hat{u_r}$, which can eventually be expressed as an eigenvalue problem of the form :

$$A\hat{u}_r=fB\hat{u}_r\ . \tag{5.12}$$

Let us denote f_r as the real part of the eigenvalue f, and f_i as the complex part of f. The system is stable if the $f_i<0$, neutral if $f_i=0$ and unstable if $f_i>0$.

A and B are linear differential operators given by

$$\begin{aligned}A=\frac{i}{Re}\Big\{&r^4D^4+6r^3D^3+\left(5-2m^2\right)r^2D^2-\left(1+2m^2\right)rD+\left(m^2-1\right)^2\Big\}\\&+m\Omega r^2\left(\left(r^2D^2+3rD+\left(1-m^2\right)\right)-mrZ'\right)\ ,\end{aligned} \tag{5.13}$$

and

$$B=r^2\left(r^2D^2+3rD+\left(1-m^2\right)\right)\ , \tag{5.14}$$

where $D\equiv\dfrac{d}{dr}$, angular velocity $\Omega=\dfrac{U_\theta}{r}$, and base vorticity $Z=U_\theta'+\dfrac{U_\theta}{r}$. Note that $'$ or prime here denotes derivate with respect to r and it not related to perturbations as previously used in deriving the equations.

In the inviscid case, we are left with

$$A=m\Omega\left(r^2D^2+3rD+\left(1-m^2\right)\right)-mrZ'\ , \tag{5.15}$$

and

$$B=r^2D^2+3rD+\left(1-m^2\right)\ . \tag{5.16}$$

5.2.1 Boundary Conditions

The physically relevant solutions, which must be continuous, can be expanded as a Taylor series about $r = 0$ and $r = \infty$. The boundary conditions depend on the background flow or mean profile being studied. All our mean profiles are such that $U_\theta \sim r$ as $r \to 0$, $U_\theta \sim \frac{1}{r}$ as $r \to \infty$. The boundary conditions are then deduced from inspection of the leading order terms of the Taylor series, and depend on the azimuthal wavenumer m,

For $\mathbf{r} \to \mathbf{0}$,

$$\hat{u}_r = O(r^{|m|-1}), \quad \hat{u}_\theta = O(r^{|m|-1}) \ . \tag{5.17}$$

For $\mathbf{r} \to \infty$,

$$\hat{u}_r = O(r^{-|m|-1}), \quad \hat{u}_\theta = O(r^{-|m|-1}) \ . \tag{5.18}$$

5.3 Formulation and solution-3D perturbations

Consider now the three-dimensional continuity and Navier-Stokes equations for an incompressible homogenous fluid in cylindrical polar co-ordinates:

$$\frac{1}{r}\frac{\partial}{\partial r}(ru_r) + \frac{1}{r}\frac{\partial}{\partial \theta}(u_\theta) + \frac{\partial}{\partial z}(u_z) = 0 \ , \tag{5.19}$$

$$\frac{\partial u_r}{\partial t} + u_r\frac{\partial u_r}{\partial r} + \frac{u_\theta}{r}\frac{\partial u_r}{\partial \theta} + u_z\frac{\partial u_r}{\partial z} - \frac{u_\theta^2}{r} = -\frac{1}{\rho}\frac{\partial p}{\partial r} + \frac{1}{Re}\left(\nabla^2 u_r - \frac{u_r}{r^2} - \frac{2}{r^2}\frac{\partial u_\theta}{\partial \theta}\right) \ , \tag{5.20}$$

$$\frac{\partial u_\theta}{\partial t} + u_r\frac{\partial u_\theta}{\partial r} + \frac{u_\theta}{r}\frac{\partial u_\theta}{\partial \theta} + u_z\frac{\partial u_\theta}{\partial z} + \frac{u_r u_\theta}{r} = -\frac{1}{\rho r}\frac{\partial p}{\partial \theta} + \frac{1}{Re}\left(\nabla^2 u_\theta + \frac{2}{r^2}\frac{\partial u_r}{\partial \theta} - \frac{u_\theta}{r^2}\right) \ , \tag{5.21}$$

$$\frac{\partial u_z}{\partial t} + u_r\frac{\partial u_z}{\partial r} + \frac{u_\theta}{r}\frac{\partial u_z}{\partial \theta} + u_z\frac{\partial u_z}{\partial z} = -\frac{1}{\rho}\frac{\partial p}{\partial z} + \frac{1}{Re}\left(\nabla^2 u_z\right) \ , \tag{5.22}$$

where

$$\nabla^2 = \frac{1}{r}\frac{\partial}{\partial r}\left(r\frac{\partial}{\partial r}\right) + \frac{1}{r^2}\frac{\partial^2}{\partial \theta^2} + \frac{1}{r^2}\frac{\partial^2}{\partial z^2} \ . \tag{5.23}$$

As before, we decompose the total motion into a background state plus perturbations:

$$u_{r_{tot}} = U_r + \tilde{u}_r \ , \tag{5.24}$$

$$u_{\theta_{tot}} = U_\theta + \tilde{u}_\theta \ , \tag{5.25}$$

$$u_{z_{tot}} = U_z + \tilde{u}_r \ , \tag{5.26}$$

$$p_{tot} = P + \tilde{p} \ . \tag{5.27}$$

Following the same procedure as before, we get

$$\frac{1}{r}\frac{\partial}{\partial r}\left(r\tilde{u}_r\right)+\frac{1}{r}\frac{\partial}{\partial\theta}\left(\tilde{u}_\theta\right)+\frac{\partial}{\partial z}\left(\tilde{u}_z\right)=0\ , \tag{5.28}$$

$$\frac{\partial\tilde{u}_r}{\partial t}+\frac{U_\theta}{r}\frac{\partial\tilde{u}_r}{\partial\theta}+U_z\frac{\partial\tilde{u}_r}{\partial z}-\frac{2U_\theta\tilde{u}_\theta}{r}=-\frac{1}{\rho}\frac{\partial\tilde{p}}{\partial r}+\frac{1}{Re}\left(\nabla^2\tilde{u}_r-\frac{\tilde{u}_r}{r^2}-\frac{2}{r^2}\frac{\partial\tilde{u}_\theta}{\partial\theta}\right)\ , \tag{5.29}$$

$$\frac{\partial\tilde{u}_\theta}{\partial t}+\tilde{u}_r\frac{\partial U_\theta}{\partial r}+\frac{U_\theta}{r}\frac{\partial\tilde{u}_\theta}{\partial\theta}+U_z\frac{\partial\tilde{u}_\theta}{\partial z}+\frac{\tilde{u}_rU_\theta}{r}=-\frac{1}{\rho r}\frac{\partial\tilde{p}}{\partial\theta}+\frac{1}{Re}\left(\nabla^2\tilde{u}_\theta+\frac{2}{r^2}\frac{\partial\tilde{u}_r}{\partial\theta}-\frac{\tilde{u}_\theta}{r^2}\right)\ , \tag{5.30}$$

$$\frac{\partial\tilde{u}_z}{\partial t}+\tilde{u}_r\frac{\partial U_z}{\partial r}+\frac{U_\theta}{r}\frac{\partial\tilde{u}_z}{\partial\theta}+U_z\frac{\partial\tilde{u}_z}{\partial z}=-\frac{1}{\rho}\frac{\partial\tilde{p}}{\partial z}+\frac{1}{Re}\left(\nabla^2\tilde{u}_z\right)\ . \tag{5.31}$$

Assuming the perturbations or infinitesimal disturbances to be of the normal mode form in θ, z and t, characterized by an axial wavenumber α, an azimuthal wavenumber m and a complex frequency f :

$$\{\tilde{u}_r,\tilde{u}_\theta,\tilde{u}_z,\tilde{p}\}=\{\hat{u}_r\left(r\right),\hat{u}_\theta\left(r\right),\hat{u}_z\left(r\right),\hat{p}\left(r\right)\}e^{i(m\theta+\alpha z-ft)}\ , \tag{5.32}$$

and substituting Eq. 5.11 in the Eqs. 5.9 and 5.10, we obtain a set of ordinary differential equations. Eliminating $\hat{p}$ and $\hat{u_z}$ from this set, we are left with set of simultaneous ordinary differential equations in $\hat{u_r}$ and $\hat{u_\theta}$, which can be expressed as an eigenvalue problem of the form :

$$A\hat{u}=fB\hat{u},\quad \hat{u}=\begin{bmatrix}\hat{u}_r\\ \hat{u}_\theta\end{bmatrix},\quad A=\begin{bmatrix}A_{11} & A_{12}\\ A_{21} & A_{22}\end{bmatrix},\quad B=\begin{bmatrix}B_{11} & B_{12}\\ B_{21} & B_{22}\end{bmatrix}\ . \tag{5.33}$$

Again, the system is stable if the $f_i<0$, neutral if $f_i=0$ and unstable if $f_i>0$.

A and B are linear differential operators given by

$$A_{11} = \frac{i}{Re}\left\{ mr^3D^3 + 2mr^2D^2 - m\left(1+m^2\right)rD - m\alpha^2r^3D + m\left(1-m^2\right) - 3m\alpha^2r^2 \right\}$$
$$+ \left\{ m^2r^2U_\theta D + m\alpha r^3U_zD - m\alpha r^3U_z' + m^2rU_\theta + \alpha^2r^4U_\theta' + m\alpha r^2U_z + \alpha^2r^3U_\theta \right\}, \quad (5.34)$$

$$A_{12} = \frac{1}{Re}\left\{ -m^2r^2D^2 - \alpha^2r^4D^2 + m^2rD - \alpha^2r^3D - m^2\left(1-m^2\right) + \alpha^2\left(1+2m^2\right)r^2 + \alpha^4r^4 \right\}$$
$$+ i\left\{ m^3rU_\theta + m\alpha^2r^3U_\theta + m^2\alpha r^2U_z + \alpha^3rU_z \right\}, \quad (5.35)$$

$$A_{21} = \frac{i}{Re}\left\{ -mr^2D^2 + mrD + m\left(m^2-1\right) + m\alpha^2r^2 \right\}$$
$$+ \left\{ -r^3U_\theta' - r^2U_\theta D - r^2U_\theta' - r^3Z' - \left(1+m^2\right)rU_\theta - m\alpha r^2U_z \right\}, \quad (5.36)$$

$$A_{22} = \frac{1}{Re}\left\{ r^3D^3 + 2r^2D^2 - \left(1+m^2\right)rD + \alpha^2r^3D + \left(1-m^2\right) - \alpha^2r^2 \right\}$$
$$+ i\left\{ -mr^2U_\theta D - \alpha r^3U_zD - mr^2U_\theta' - 2mrU_\theta - \alpha r^3U_z' - \alpha r^2U_z \right\}, \quad (5.37)$$

$$B_{11} = \left(mr^2 + mr^3D\right), \quad (5.38)$$

$$B_{12} = i\left(\alpha^2r^4 + m^2r^2\right), \quad (5.39)$$

$$B_{21} = \left(-mr^2\right), \quad (5.40)$$

$$B_{22} = -i\left(r^3D + r^2\right). \quad (5.41)$$

Note that $'$ or prime again denotes derivate with respect to r.

In the inviscid case, we are left with

$$A_{11} = \left\{ m^2rU_\theta D + m\alpha r^2U_zD - m\alpha r^2U_z' + m^2U_\theta + \alpha^2r^3U_\theta' + m\alpha rU_z + \alpha^2r^2U_\theta \right\}, \quad (5.42)$$

$$A_{12} = i\left\{ m^3U_\theta + m\alpha^2r^2U_\theta + m^2\alpha rU_z + \alpha^3U_z \right\}, \quad (5.43)$$

$$A_{21} = \left\{ -r^2U_\theta' - rU_\theta D - rU_\theta' - r^2Z' - \left(1+m^2\right)U_\theta - m\alpha rU_z \right\}, \quad (5.44)$$

$$A_{22} = i\left\{ -mrU_\theta D - \alpha r^2U_zD - mrU_\theta' - 2mU_\theta - \alpha r^2U_z' - \alpha rU_z \right\}, \quad (5.45)$$

$$B_{11} = \left(mr + mr^2D\right), \quad (5.46)$$

$$B_{12} = i\left(\alpha^2r^3 + m^2r\right), \quad (5.47)$$

$$B_{21} = \left(-mr\right), \quad (5.48)$$

$$B_{22} = -i\left(r^2D + r\right). \quad (5.49)$$

5.3.1 Boundary conditions

As explained earlier in the 2D case, we inspect the leading-order terms in the Taylor series expansion about $r = 0$ and $r = \infty$. Depending on the azimuthal wavenumber m, we get

As $\mathbf{r} \to \mathbf{0}$,
if $m = 0$,

$$\hat{u}_r = O(r), \quad \hat{u}_\theta = O(r), \quad \hat{u}_z = O(1), \quad \hat{p} = O(1) \ ; \tag{5.50}$$

if $m \neq 0$,

$$\hat{u}_r = O(r^{|m|-1}), \quad \hat{u}_\theta = O(r^{|m|-1}), \quad \hat{u}_z = O(r^{|m|}), \quad \hat{p} = O(r^{|m|}) \ . \tag{5.51}$$

As $\mathbf{r} \to \infty$,

$$\hat{u}_r \to 0, \quad \hat{u}_\theta \to 0, \quad \hat{u}_z \to 0, \quad \hat{p} \to 0 \quad \text{(exponential decay)}. \tag{5.52}$$

Note that while 3D perturbations decay exponentially, 2D perturbations decay algebraically. These boundary conditions were originally derived by Batchelor & Gill (1962) in the form of compatibility relations, and were formalized later on by Lessen & Paillet (1974) and Khorrami *et al.* (1989).

5.4 Chebyshev collocation technique

We solve the eigenvalue problems formulated above using a Chebyshev collocation technique. Here, we describe some of the basic formulas and important aspects of the technique.

The Chebyshev polynomials of the first kind, $T_k(x)$, $k = 0, 1, 2, \ldots$, are the eigenfunctions of the singular Sturm-Liouville problem

$$\left(\sqrt{1-x^2}\,T_k'(x)\right)' + \frac{k^2}{\sqrt{1-x^2}}T_k(x) = 0 \ . \tag{5.53}$$

Normalizing T_k so that $T_k(1) = 1$, we get

$$T_k(x) = \cos k\theta, \quad \theta = \arccos x \ . \tag{5.54}$$

From this, we see that Chebyshev polynomials are basically cosine functions after a change of independent variable. The transformation $x = \cos\theta$ lets us take advantage of many properties related to the Fourier system (being a Fourier cosine series).

Using the trigonometric identity $\cos(k+1)\theta + \cos(k-1)\theta = 2\cos\theta\cos k\theta$, we get the following

recurrence relation

$$T_{k+1}(x) - 2xT_k(x) + T_{k-1}(x) = 0,\ k \geq 1\ , \tag{5.55}$$

with $T_0(x) = 1$ and $T_1(x) = x$. Some other interesting properties of Chebyshev polynomials are

$$|T_k(x)| \leq 1, \quad -1 \leq x \leq 1\ , \tag{5.56}$$

$$|T_k'(x)| \leq k^2, \quad -1 \leq x \leq 1\ , \tag{5.57}$$

$$T_k(\pm 1) = (\pm 1)\,, \quad T_k'(\pm 1) = (\pm 1)^{k+1} k^2\ , \tag{5.58}$$

$$T_k(-x) = (-1)^k T_k(x)\ . \tag{5.59}$$

Also, $T_k(x)$ vanishes at Gauss points x_i defined by

$$x_i = \cos\left(i + \frac{1}{2}\right)\frac{\pi}{k}, \quad i = 0, \ldots, k-1\ , \tag{5.60}$$

and reaches its extremal value (± 1) at Gauss-Lobatto points x_i defined by

$$x_i = \cos\frac{\pi i}{k}, \quad i = 0, \ldots, k\ . \tag{5.61}$$

Chebyshev polynomials are orthogonal on $[-1, 1]$ with the weight $w = \left(1 - x^2\right)^{-1/2}$ as follows :

$$(T_k, T_l)_w = \int_{-1}^{1} T_k T_l w\, dx = \frac{\pi}{2} c_k \delta_{k,l}\ , \tag{5.62}$$

where $\delta_{k,l}$ is the Kronecker delta and c_k is defined by

$$c_k = \begin{cases} 2 & \text{if } k = 0\ , \\ 1 & \text{if } k \geq 1\ . \end{cases} \tag{5.63}$$

The discrete orthogonality relationship based on Gauss-Lobatto points $x_i, i = 0, 1, \ldots, N$ can be deduced from quadrature formula and is given by

$$\sum_{i=0}^{N} \frac{1}{\bar{c}_i} T_k(x_i)\, T_l(x_i) = \frac{\bar{c}_k}{2} N \delta_{k,l} \quad 0 \leq k, l \leq N\ , \tag{5.64}$$

where

$$\bar{c}_k = \begin{cases} 2 & \text{if } k = 0, N\ , \\ 1 & \text{if } 1 \leq k \leq N-1\ . \end{cases} \tag{5.65}$$

Now, let us consider the Chebyshev expansion of a function $u(x)$ defined for $x \in [-1, 1]$:

$$u(x) = \sum_{k=1}^{\infty} \hat{u}_k T_k(x)\,, \quad \hat{u}_k = \frac{2}{\pi c_k} \int_{-1}^{1} u(x)\, T_k(x)\, w(x)\ dx\ . \tag{5.66}$$

In the discrete case based on Gauss-Lobatto points $x_k, k = 0, 1, \ldots, N$, we use a truncated Chebyshev series given by

$$u_N(x) = \sum_{k=1}^{N} \hat{u}_k \cos k\theta, \qquad \hat{u}_k = \frac{2}{\bar{c}_k N} \sum_{i=0}^{N} \frac{1}{\bar{c}_i} u_i \cos \frac{k\pi i}{N}, \quad k = 0, \ldots, N \ . \tag{5.67}$$

As observed in Eq. 5.67, we will use the Chebyshev Gauss-Lobatto method in our interpolation, for which the quadrature points and weights are given by

$$x_j = \cos \frac{\pi j}{N}, \quad w_j = \begin{cases} \dfrac{\pi}{2N}, & j = 0, N \ , \\ \dfrac{\pi}{N}, & j = 1, \ldots, N-1 \ . \end{cases} \tag{5.68}$$

5.4.1 Differentiation

By using the trigonometrical identity $2 \sin\theta \cos k\theta = \sin(k+1)\theta - \sin(k-1)\theta$, we can get the following recurrence relation on the derivative :

$$2T_k(x) = \frac{T'_{k+1}(x)}{k+1} - \frac{T'_{k-1}(x)}{k-1}, \quad k \geq 1 \ . \tag{5.69}$$

We can then write

$$T'_k(x) = 2k \sum_{n=0}^{K} \frac{1}{c_{k-1-2n}} T_{k-1-2n}(x), \quad K = (k-1)/2 \ . \tag{5.70}$$

So the first order derivative can be written as

$$u'_N(x) = \sum_{k=0}^{N} \hat{u}_k T'_k(x) = \sum_{k=0}^{N} \hat{u}'_k T_k(x) = \sum_{k=0}^{N} \hat{u}^{(1)}_k T_k(x) \ . \tag{5.71}$$

From Eq. 5.70, we get

$$\hat{u}^{(1)}_k = \frac{2}{c_k} \sum_{\substack{p=k+1 \\ p+k \text{ odd}}}^{N} p\hat{u}_p, \quad k = 0, 1, \ldots, N-1 \ . \tag{5.72}$$

Eq. 5.69 gives

$$2k\hat{u}_k = c_{k-1}\hat{u}^{(1)}_{k-1} - \hat{u}^{(1)}_{k+1}, \quad k \geq 1 \ . \tag{5.73}$$

To find the derivative in physical space, one can transform the expression into Chebyshev space (this can be done using an FFT), find the discrete Chebyshev coefficients of the derivative using the recurrence relation, and then transform back into physical space. We will however use another technique to find the Chebyshev interpolation derivative. The pth Chebyshev collocation

derivative $u_N^{(p)}$ can be expressed in terms of the grid values of the function as :

$$u_N^{(p)}(x_i) = \sum_{j=0}^{N} d_{i,j}^{(p)} u_N(x_j), \quad i = 0, \ldots, N \ . \tag{5.74}$$

The coefficients $d_{i,j}^{(p)}$ can be calculated as follows. First, we eliminate $\hat{u}_k$ from the derivative

$$u_N^{(p)}(x_i) = \sum_{k=0}^{N} \hat{u}_k T_k^{(p)}(x_i) \ , \tag{5.75}$$

by using Eq. 5.67. Then, by applying trigonometrical identities, we evaluate the sums which contain $T_k(x_i)$ and $T_k'(x_i)$(which are in turn in the form of cosines and sines ($T_k = \cos k\theta$)).

The first order derivative is then given by

$$d_{i,j}^{(1)} = \begin{cases} \dfrac{\bar{c}_i}{\bar{c}_j} \dfrac{(-1)^{i+j}}{(x_i - x_j)}, & 0 \le i, j \le N, i \ne j \ , \\ -\dfrac{x_i}{2\left(1 - x_i^2\right)}, & 1 \le i = j \le N - 1 \ , \\ \dfrac{2N^2 + 1}{6}, & i = j = 0 \ , \\ -\dfrac{2N^2 + 1}{6}, & i = j = N \ . \end{cases} \tag{5.76}$$

The higher order derivatives are obtained as follows :

$$d_{i,j}^{(2)} = \sum_{k=0}^{N} d_{i,k}^{(1)} d_{k,i}^{(1)} \quad \text{and so on} \tag{5.77}$$

In vector form, the derivatives can be expressed as

$$U^{(1)} = DU, \quad U^{(2)} = D^{(2)}U, \quad \ldots, U^{(p)} = D^{(p)}U \ , \tag{5.78}$$

where

$$U = \left(u_N(x_0), \ldots, u_N(x_0)\right)^T, \quad U^{(p)} = \left(u_N^{(p)}(x_0), \ldots, u_N^{(p)}(x_0)\right)^T \ , \tag{5.79}$$

and the differentiation matrix D is defined by

$$D = \left[d_{i,j}^{(1)}\right], \quad i, j = 0, 1, \ldots, N \ . \tag{5.80}$$

Finally, Eqs. 5.76 and 5.79 are the ones we use, to calculate the derivative in our system. For more information on Chebyshev collocation technique, refer Boyd (2001).

5.5 Grid Stretching

The domain for our problem is $[0, \infty]$. We first discretize the equations on a Chebyshev grid $[-1, 1]$, and later map it algebraically or exponentially to $[0, R_{max}]$.We have used three types of stretching to map the Chebyshev grid to the required grid $[0, R_{max}]$.

(a)

$$y = \frac{1-\xi}{b+\xi}, \quad b = 1 + \frac{2a}{R_{max}} \ , \tag{5.81}$$

where ξ is the Chebyshev coordinate defined by Eq. 5.68, and a is the radius within which close to half the points lie (Khorrami *et al.* 1989).

(b)

$$y = \frac{1-\xi}{b + c\xi + d\xi^3}, \quad b = 1 + \frac{2a}{R_{max}}, \quad a = \frac{pR_{max}}{R_{max} - 2p} \ , \tag{5.82}$$

$$(0.5 \leq c \leq 0.8) \, , \quad d = (1-c) \ ,$$

where p is the radius at which clustering is required.

(c)

$$y = \frac{aR_{max}}{\sinh(by_o)} \left\{ \sinh\left[\left(\frac{(\xi+1)}{2} - y_o \right) b \right] + \sinh(by_o) \right\} \ , \tag{5.83}$$

$$y_o = \frac{0.5}{b} log \left\{ \frac{\left[1 + \left(e^b - 1\right) a\right]}{\left[1 + \left(e^{-b} - 1\right) a\right]} \right\}, \quad (5 \leq b \leq 20) \ ,$$

where $p = (aR_{max})$ is the radius at which clustering is required (Govindarajan 2004).

It must be noted that mappings (a) and (b) are algebraic while mapping (c) is exponential. Also mapping (a) clusters the points near the origin and de-clusters the points away from it, while mappings (b) and (c) cluster the points at a chosen finite radius which in our case are regions of high shear. In other words, mapping (a) is used mainly for a mean profile of the q-vortex or Batchelor vortex (during the validation of the 3D code), while mappings (b) and (c) are used for a mean profile of an annular vortex which has regions of high shear at a finite radius away from the axis.

Chapter 6

Linear stability analysis of annular vortex: Validation and Results

6.1 Scope

This chapter contains the validation of the stability code and results from the linear stability analysis of an annular vortex. To begin with, we define the vorticity profiles and the various parameters involved in the analysis. We go on to discuss our main findings and then conclude.

6.2 Setting up the problem

Here we describe the mean vorticity profiles, the various parameters and non-dimensional numbers. We keep the total circulation Γ constant ($\Gamma = \Gamma_o = 2\pi$) throughout the analyses. The Reynolds number for the viscous studies is defined as $Re = \Gamma/\nu$. We then study the linear stability for the following three mean vorticity profiles

- Step profile (annular Rankine):

$$\omega = \begin{cases} 0, & 0 \leq r < b \ , \\ \dfrac{2}{(1-b^2)}, & b \leq r < 1 \ , \\ 0, & r \geq 1 \ . \end{cases} \tag{6.1}$$

  We define a thickness parameter δ as the ratio of the thickness to the mean radius of the annular vortex. Here, $\delta = \dfrac{2\,(1-b)}{(1+b)}$.

- Tanh profile:

$$\omega = \frac{\omega_{max}}{2}\left[\tanh\left(\frac{r-b}{c}\right) - \tanh\left(\frac{r-1}{c}\right)\right] \ , \tag{6.2}$$

  where $\omega_{max} = \dfrac{2}{(1-b^2)}$. This vorticity maximum gives $\Gamma = 2\pi$. This profile is similar to the step profile and approaches the step profile in the limit $c \to 0$. In our studies, we take $c = 0.01$.

- Generalized Lamb-Oseen (GLO) from chapter 4:

$$\omega = \frac{\Gamma_o}{4\pi\nu t} e^{-\left(\frac{a^2+r^2}{4\nu t}\right)} I_0\left\{\frac{ar}{2\nu t}\right\} \ . \tag{6.3}$$

For our stability analysis, we first consider profiles frozen in time by fixing the term 'νt' (we are performing a quasi-steady stability analysis). Next, we choose $a = 1$ and calculate the thickness of the annular vortex by looking at the radii at which the vorticity drops to $1/e$ of its maximum value. We then normalize this thickness by mean radius of the annulus (radius of vorticity maximum) to get δ (thickness parameter). From now onwards, we will refer to this profile as GLO.

It must be noted that the mean flow for our analysis is two-dimensional with no variation in the axial or vertical direction. We then perturb this mean flow in the usual manner (normal modes) and see if the perturbations grow or decay in time.

6.3 Validation and results for 2D perturbations

Here, we subject the mean flow to two-dimensional perturbations as discussed in chapter 5 and look for eigenvalues with positive imaginary part for the growth of perturbations. For the 2D analysis, we use the mappings 5.82 and 5.83 discussed in chapter 5. These mappings cluster the points at a region away from the axis where velocity and vorticity gradients are high. We find that both the algebraic and exponential mappings give similar results (which by itself is a validation). In the 2D case, we proceed to use the algebraic mapping 5.82 as the boundary conditions dictate that the eigenfunctions decay algebraically. Also, we must remember that our physical domain is $[0, R_{max}]$, following the mapping from the Chebychev grid $[-1, 1]$. For convergence of eigenvalues, we first keep R_{max} constant and vary the number of collocation points N. We then repeat this by increasing R_{max}. We start from $R_{max} = 20$ and go on till $R_{max} = 1000$. The R_{max} for convergence is large since the eigenfunctions decay algebraically (and not exponentially). For the tanh and GLO profiles, we vary the number of Chebychev collocation points N from 200 to 1000, with which we are able obtain convergence of eigenvalues up to decimal places.

By taking a look at the 2D inviscid and viscous equations in chapter 5, one can observe that for every growing mode with a positive m, there exists a corresponding decaying mode with a negative m (the equations remain unchanged when f and m are replaced by $-f$ and $-m$ respectively). Hence, we consider only positive values of m for our analysis. In addition to this, the periodicity in cylindrical co-ordinates dictates that m must be an integer. Also, we do not consider $m = 1$ disturbance as it only represents a translation.

In order to validate our 2D inviscid code, we compare the growth rate f_i vs the azimuthal wavenumber m for the step and tanh profiles. The dispersion relation for the step profile can be found analytically (Michalke & Timme 1967) and is given by

$$f = f_r + f_i i = \frac{m}{2} + \frac{\{4b^{2m} - \left[m\left(1-b^2\right) - 2\right]^2\}^{1/2}}{2\left(1-b^2\right)} i \ , \tag{6.4}$$

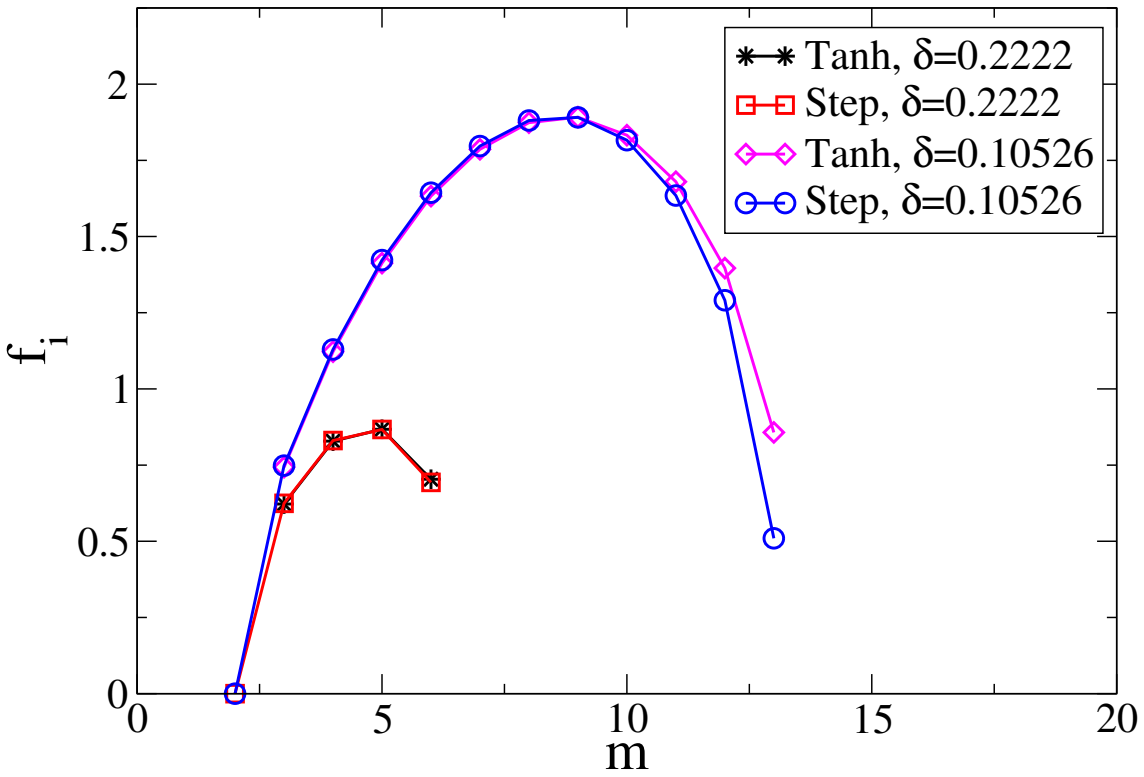

Figure 6.1: Validation of 2D code for inviscid case: Growth rate f_i vs azimuthal wavenumber m for Step (analytical result) and tanh (numerical result) profiles. $\delta = 0.2222$ and 0.10526 correspond to $b = 0.8$ and 0.9 respectively.

where f_r is the cyclic frequency and f_i is the growth rate. In the limit $b \to 1$ (infinitely thin cylindrical vortex sheet), this relation reduces to that of Rotunno (1978) given by

$$f = f_r + f_i i = \frac{m}{2} + \frac{[m\,(m-2)]^{1/2}}{2} i\ . \tag{6.5}$$

Thus, except for modes $m = 1$ and 2, the result for the infinitely thin cylindrical vortex sheet is analogous to that for a plane shear flow (there all wavelengths are unstable, with the smallest waves growing most rapidly). Apart from this, the step profile with finite thickness has an upper cutoff for unstable m beyond which it is stable again. This is in contrast to the infinitely thin cylindrical vortex sheet where all m beyond 2 are unstable.

As a validation, Fig. 6.1 shows growth rate f_i vs the azimuthal wavenumber m for step and tanh profiles. It can be seen that there is an excellent agreement in values of f_i for smaller wavenumbers. However, as we proceed to larger wavenumbers, there is a slight deviation of f_i for the tanh profile from that of the step profile. This is because of the presence of a length scale associated with the change in vorticity at the edges of the annulus for the tanh profile. Hence, the larger wavenumbers (smaller wavelengths) begin to sense the length scale over which the vorticity changes in the tanh profile. In the case of a step profile, the vorticity gradient at the edges of the annulus is a delta function (occurring over an infinitesimally small length scale), and the larger m do not sense this length scale. The deviation for larger values of m can be reduced by considering smaller values of the parameter c (to effectively reduce c/δ) in our tanh

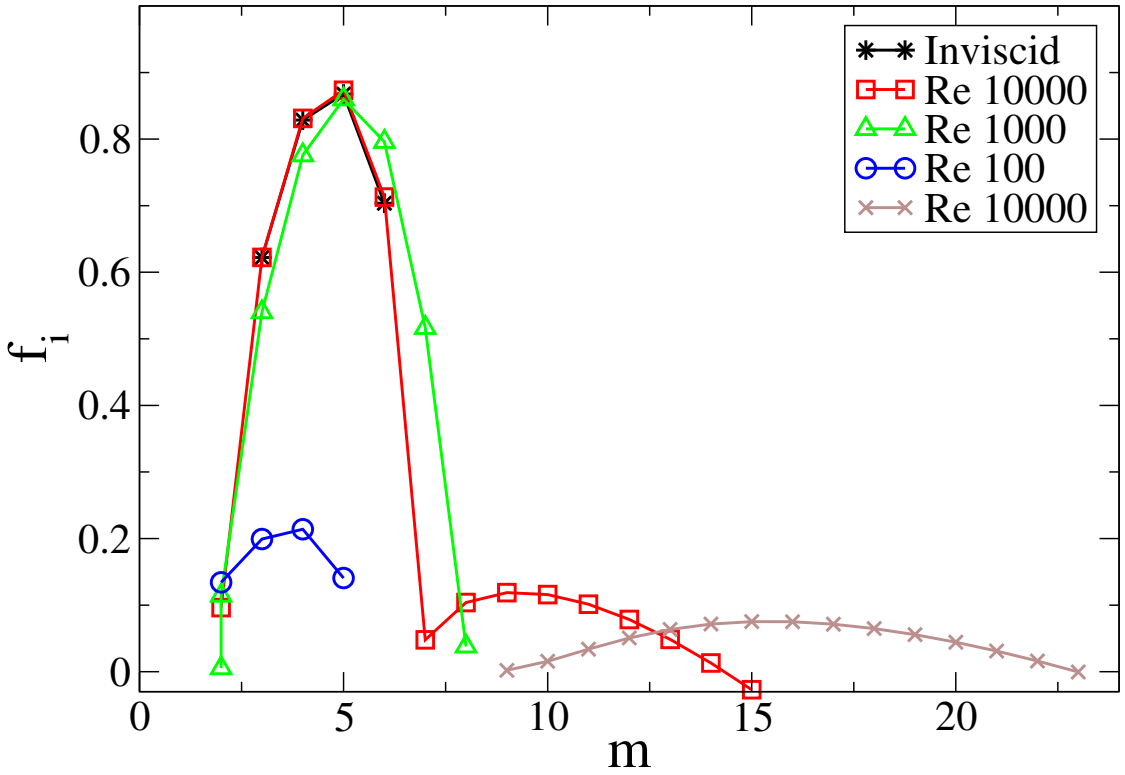

Figure 6.2: Growth rate f_i vs azimuthal wavenumber m for tanh profile with $\delta = 0.2222$ ($b = 0.8$) and varying Reynolds. Observe the multiple branches for $Re = 10000$.

profile (we use $c = 0.01$).

In the 2D viscous case, we validate the code by prescribing the mean flow as a simple Lamb-Oseen vortex (we use mapping 5.81, which clusters points near the axis). It is well known that the Lamb-Oseen is stable to two-dimensional disturbances, which is what we observe. In addition to this, we also check if the results for the annular vortex profiles at high Reynolds numbers tend to that of the inviscid case. This is evident from the figures discussed below.

We now move on to our results and findings in the linear stability analysis of the tanh and GLO vorticity profiles. Fig. 6.2 shows the growth rate f_i vs azimuthal wavenumber m for a tanh mean vorticity profile with $\delta = 0.2222$ ($b = 0.8$) and varying Reynolds. First, it can be seen that the $Re = 10000$ curve is very close to the inviscid curve for $m = 3$ to $m = 6$. From $m = 7$ onwards, the inviscid modes do not grow. It may be remembered that point vortices beyond seven in number on a circle were unstable. Thus, the inviscid result for a thin continuous circular sheet is in contrast to the inviscid result for discrete vortices. In the viscous case, there is an anomalous behavior for $Re = 10000$ case, wherein we obtain two local maxima for the growth rate. Viscosity seems to destabilize modes $m \geq 7$ till an upper cut off m, beyond which they are stable again. Note that this result is unusual. There is a high wavenumber viscous unstable mode, which is stabilized in the inviscid case. Also, the $m = 2$ disturbance is unstable for the viscous cases, with multiple (two) modes present for $Re = 1000$ (remember that $m = 2$ is stable for step profile in inviscid case). We also observe multiple branches (and multiples modes)

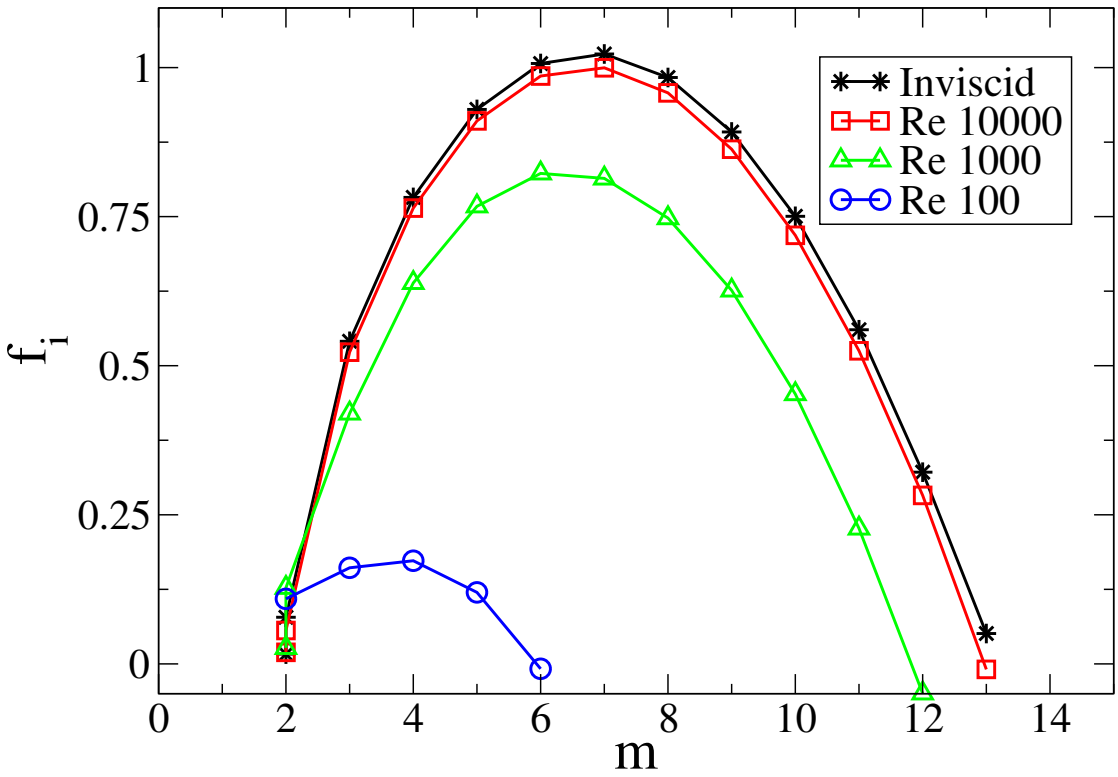

Figure 6.3: Growth rate f_i vs azimuthal wavenumber m for GLO profile with $\delta = 0.183$ ($\nu t = 0.002$) and varying Reynolds. $m = 2$ is unstable with multiple modes at higher Re.

for higher m at $Re = 10000$. As we decrease Re from 10000 to 1000, the curve shifts slightly towards the right with the anomalous behavior disappearing ($m = 9$ to 21 become stable) to give a single maximum for growth rate. As we go from $Re = 1000$ to 100, the maximum growth rate decreases strongly along with the unstable range of m.

Fig. 6.3 shows the growth rate f_i vs azimuthal wavenumber m for a generalized Lamb-Oseen profile with $\delta = 0.183$ ($\nu t = 0.002$) and varying Reynolds. It is evident from this that as Re decreases, the maximum growth rate decreases along with the unstable range of m (upper cut off decreases). However, the decrease is stronger when going from $Re = 1000$ to 100 than that from $Re = 10000$ to 1000. As we increase Re, the curve tends to that of the inviscid case, which is expected. In addition to this, $m = 2$ disturbance is once again unstable, having multiple (two) unstable modes for the inviscid as well as the viscous cases (except for very low $Re = 100$, which has only one mode). This can be clearly observed in Fig. 6.4. We have also plotted the radial velocity perturbation eigenfunctions for $m = 2$, 3 and 7 for various Reynolds numbers, as depicted in Figs. 6.5, 6.8, 6.6 and 6.7. Also, Fig. 6.9 reveals two branches or modes for the $m = 2$ disturbance. We can clearly observe a crossover (primary mode becomes secondary and vice versa) of the two modes at a particular Reynolds number. From Figs. 6.5 we can see the evolution of the shape of the eigenfunction with varying Re. Strangely enough, the eigenfunction for $Re = 600$ (for which only one mode is unstable) closely resembles that of the secondary mode for $Re = 1000$ and not that of the primary mode. This is surprising, as from Fig. 6.8, one can observe that it is the primary mode (higher growth rate) which remains unstable for very low Re.

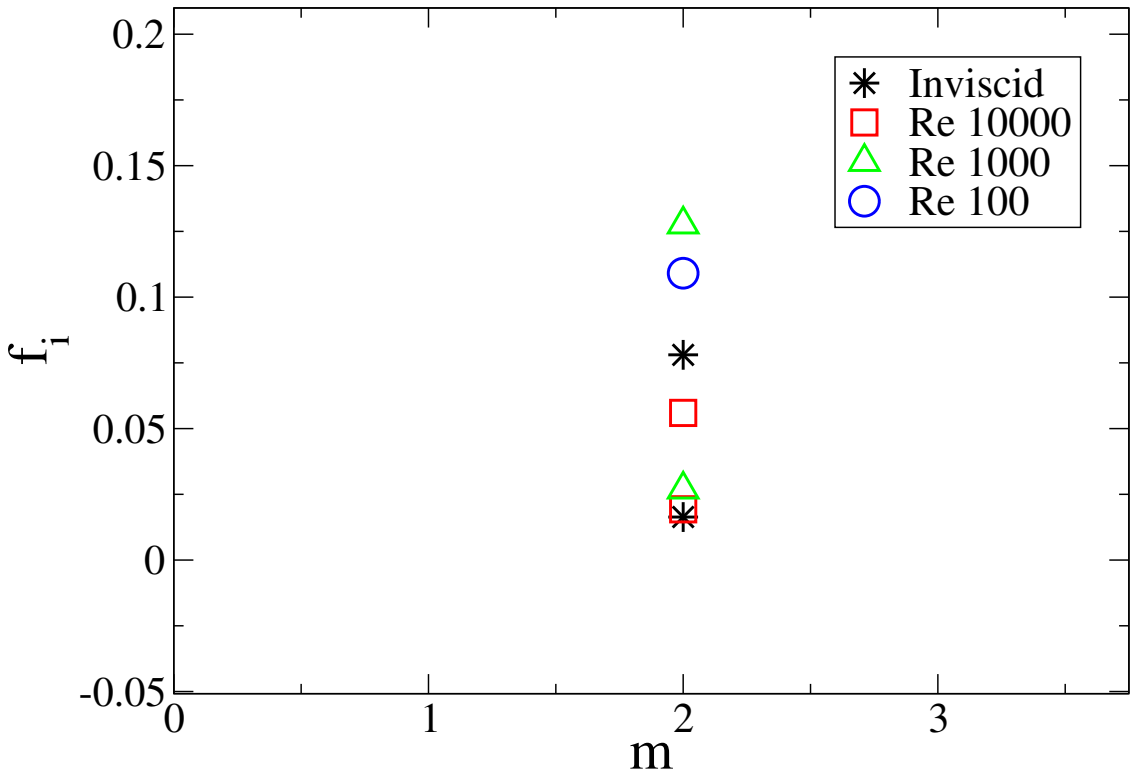

Figure 6.4: $m = 2$ disturbance growth rate for GLO profile with $\delta = 0.183$ ($\nu t = 0.002$) and varying Reynolds. Observe multiple modes for higher Re

Next, we fix the Reynolds ($Re = 10000$) and vary δ for the GLO profile. From Fig. 6.10, we can see that as δ decreases, the maximum growth rate increases strongly along with the unstable range of m (upper cut off increases). In other words, the thinner the vortex sheet, the more unstable it is, which is in accordance with intuition. In addition to this, we once again observe multiple modes for $m = 2$ for all δ.

Figs. 6.11 and 6.12 show a comparison of tanh and generalized Lamb-Oseen profiles, where we have plotted the growth rate f_i vs azimuthal wavenumber m for $\delta = 0.183$. It can the observed that the maximum growth rate is slightly higher for the tanh profile for $Re = 1000$ and 10000. However, due to the anomalous behavior of the tanh profile for higher modes at $Re = 10000$ case, we are unable to come to any conclusions about the range of modes going unstable.

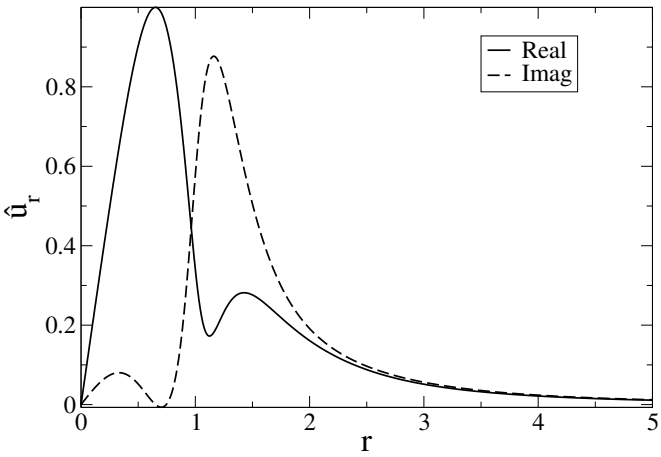

(a) $Re = 100$

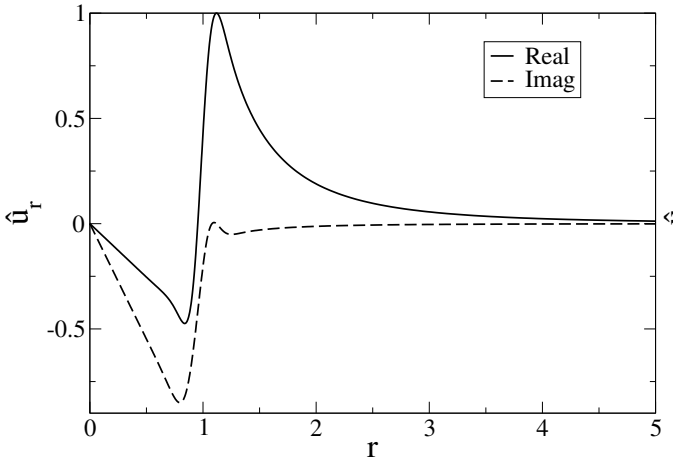

(b) $Re = 1000$, mode 1

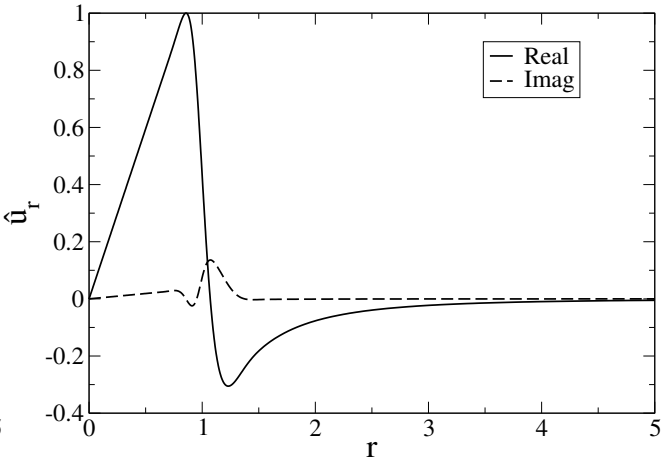

(c) $Re = 1000$, mode 2

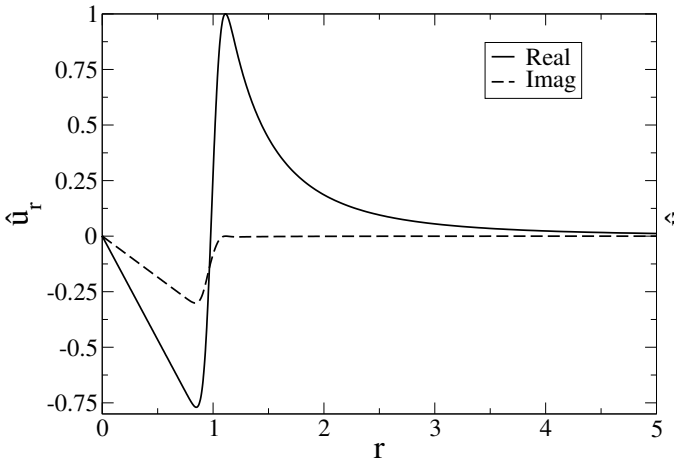

(d) $Re = 10000$, mode 1

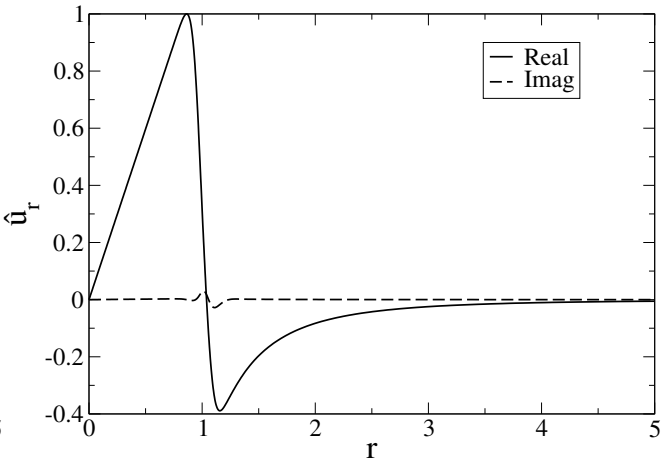

(e) $Re = 10000$, mode 2

Figure 6.5: Real and imaginary parts of radial velocity perturbation eigenfunctions for $m = 2$ disturbance.

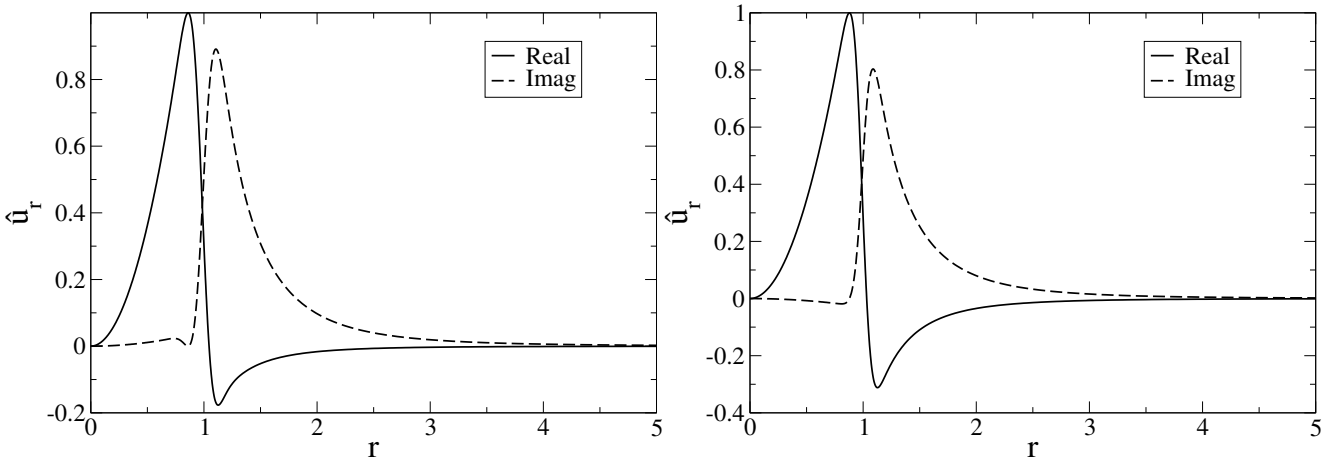

(a) $Re = 1000$ (b) $Re = 10000$

Figure 6.6: Real and imaginary parts of radial velocity perturbation eigenfunctions for $m = 3$.

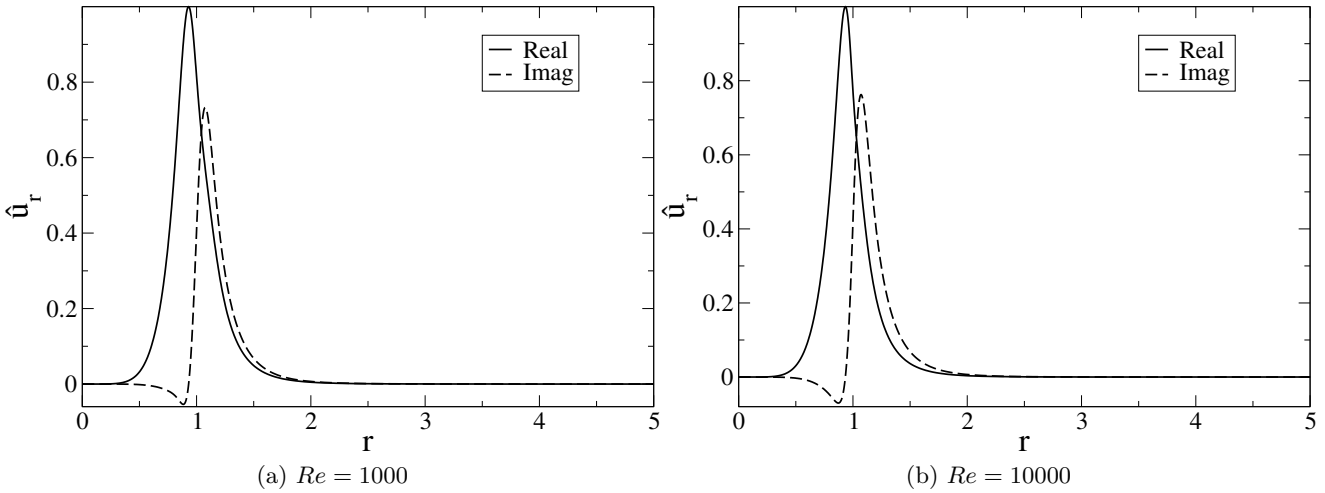

(a) $Re = 1000$ (b) $Re = 10000$

Figure 6.7: Real and imaginary parts of radial velocity perturbation eigenfunctions for $m = 7$.

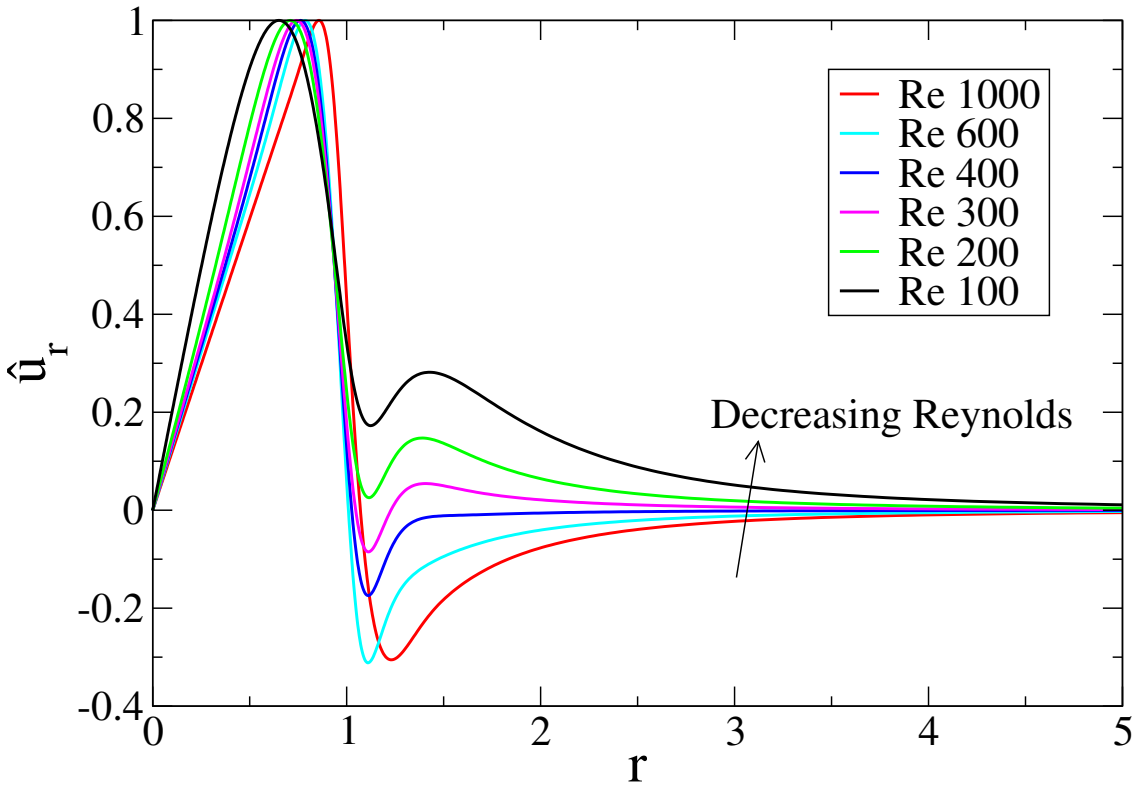

Figure 6.8: Evolution of radial velocity perturbation eigenfunctions for $m = 2$ disturbance with varying Re.

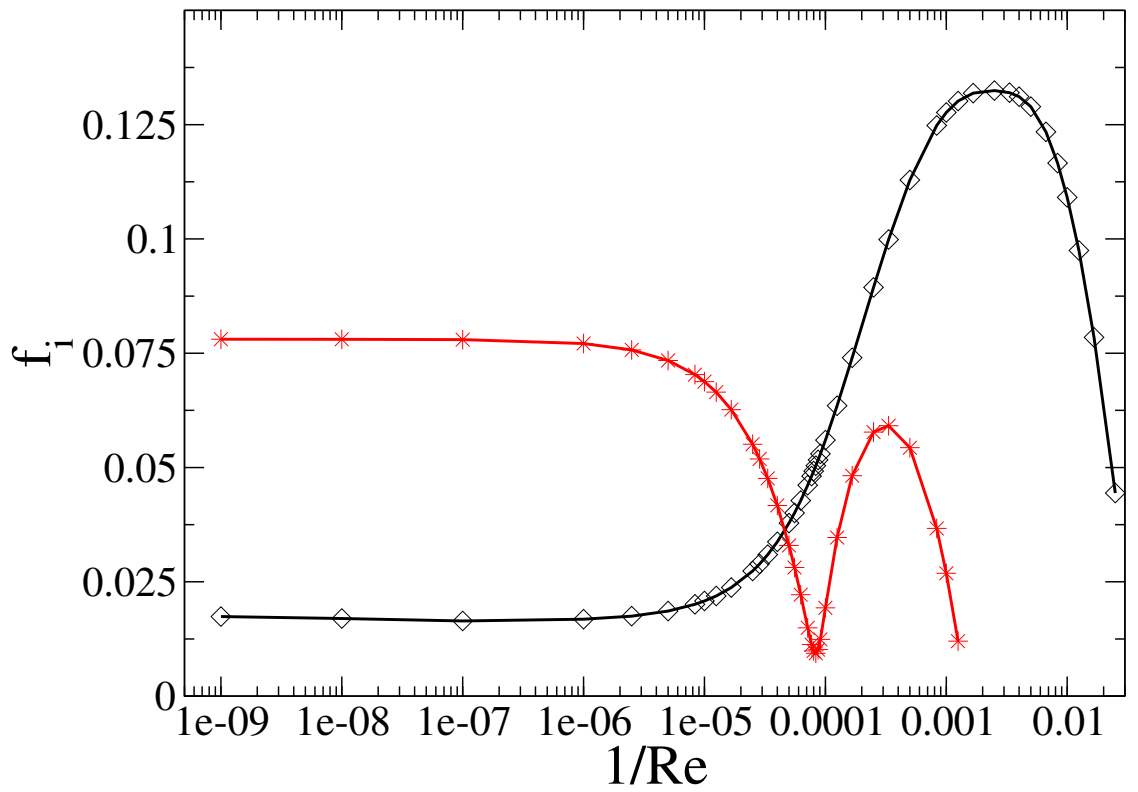

Figure 6.9: Growth rate f_i vs $1/Re$ for $m = 2$ disturbance revealing two modes at any Reynolds number in the range 950 to ∞

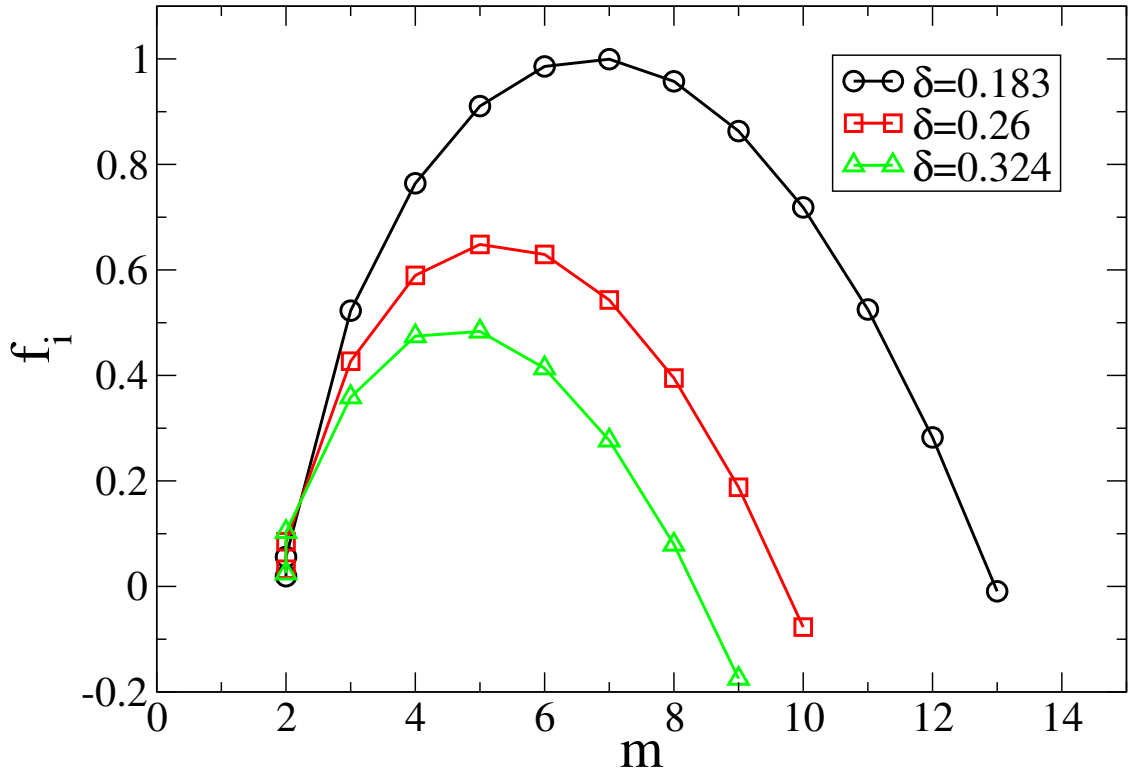

Figure 6.10: Growth rate f_i vs azimuthal wavenumber m for GLO profile with $Re = 10000$ and varying δ. $\delta = 0.183,\ 0.26$ and 0.324 correspond to $\nu t = 0.002,\ 0.004$ and 0.006 respectively.

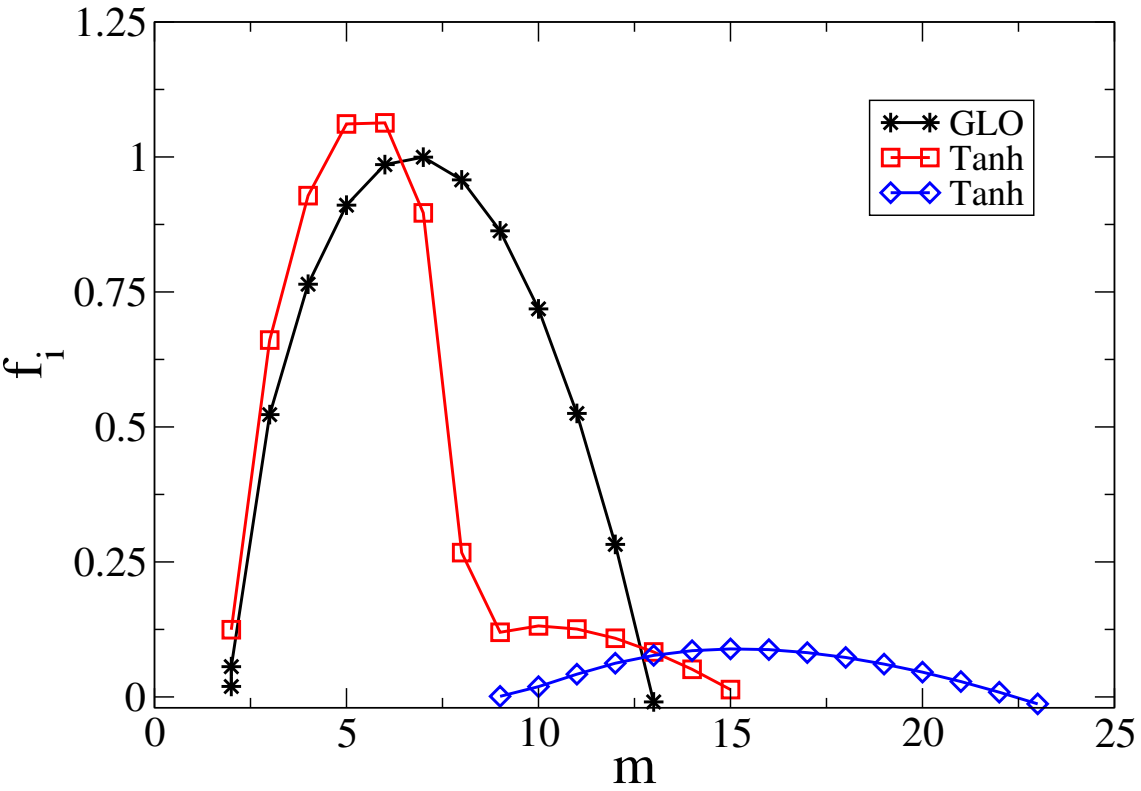

Figure 6.11: Comparison of tanh and GLO profiles: Growth rate f_i vs azimuthal wavenumber m for $Re = 10000$ and $\delta = 0.183$.

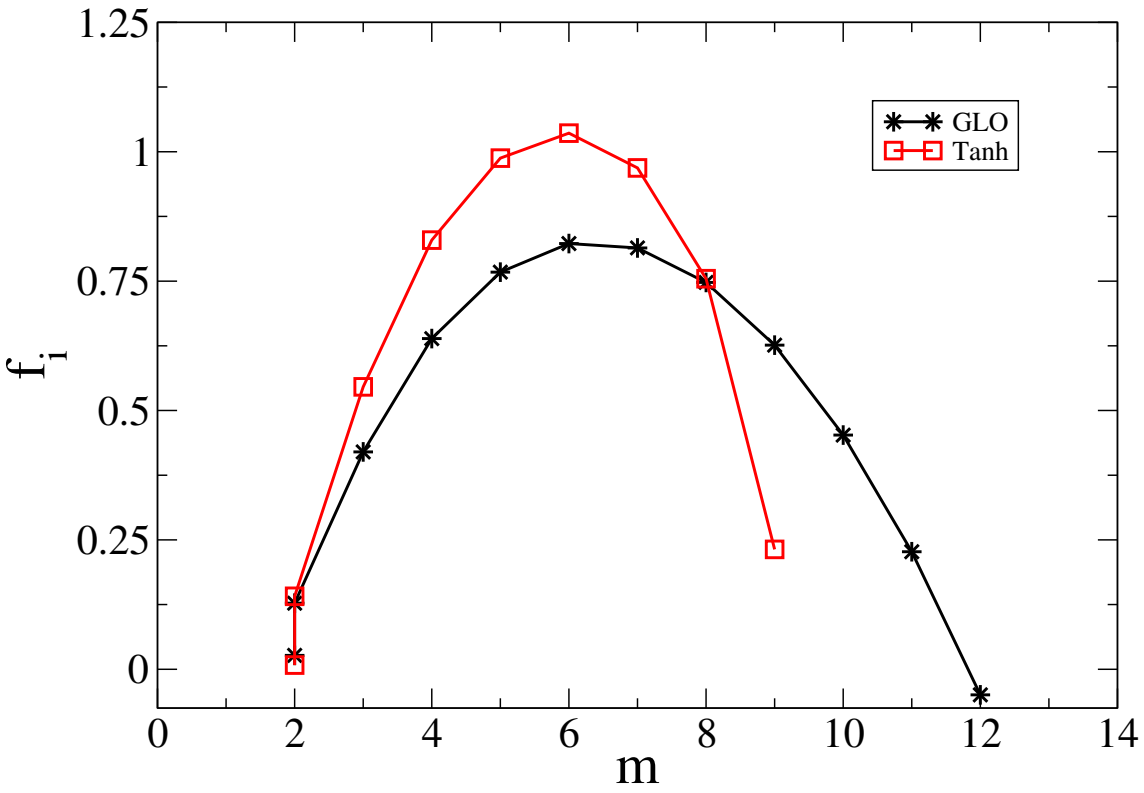

Figure 6.12: Comparison of tanh and GLO profiles: Growth rate f_i vs azimuthal wavenumber m for $Re = 1000$ and $\delta = 0.183$.

6.4 Validation for 3D perturbations

Here, we subject the mean flow to three-dimensional perturbations as discussed in chapter 5 and look for eigenvalues with positive imaginary part for the growth of perturbations. Only a validation exercise has been carried out so far, and the 3D study on the annular vortex is left for the future. In order to validate our code for 3D perturbations, we consider a well-known three-dimensional mean flow, namely the q-vortex. This vortex is widely used to model trailing line vortices, with the velocity distribution given by

$$U_r = 0, \quad U_\theta = \frac{q}{r}\left(1 - e^{-r^2}\right), \quad U_z = U_\infty + e^{-r^2}\ , \tag{6.6}$$

where U_r, U_θ and U_z are the radial, tangential and axial velocities, respectively. The swirl parameter, q, is related to the ratio of the maximum swirl velocity to the maximum axial velocity excess (or defect). The Reynolds number Re is based on the axial velocity scale and the dispersion radius of vorticity. The q-vortex actually corresponds to a simplification of the Batchelor (1964) vortex (trailing vortex model), which is a spatially evolving similarity solution of the incompressible Navier-Stokes equations under a quasi-parallel approximation. We use mapping 5.81, which clusters the points near the axis of the vortex. A closer look at 6.6 reveals that for $r > 3$, the axial velocity is essentially zero and the azimuthal velocity approaches q/r, which is a potential vortex. Therefore, we set the value of a in mapping 5.81 to 3. We follow the same procedure used in the 2D analysis for convergence of eigenvalues. In the 3D case, we vary the domain size R_{max} from 20 to 100, and number of collocation points N from 60 to 200. Note

that the R_{max} for convergence in the 3D case is much smaller than that for the 2D case because of exponential decay of eigenfunctions in the 3D case. We are able to obtain convergence of eigenvalues up to eleven decimal places. We have validated our 3D code with a few papers and the results are summarized below.

- $m = 1$, $\alpha = 0.5$, $q = -0.5$, Inviscid, most unstable modes
  Mayer & Powell (1992):

$$f_1 = 0.0497186499174 + 0.20262810129 42i$$
$$f_2 = -0.01620888889 + 0.10582318954i$$
$$f_3 = -0.029538003 + 0.060053650i$$

  Our Code:

$$f_1 = 0.0497186499 + 0.2026282013i$$
$$f_2 = -0.0162088889 + 0.10582318954i$$
$$f_3 = -0.0295380031 + 0.0600536528i$$

- $m = -1$, $\alpha = 0.811$, $q = 0.458$, $Inviscid$, maximum growth rate
  Fabre & Jacquin (1992): $f_i = 0.2424$
  Our Code: $f_i = 0.24244262434$

- $m = -2$, $\alpha = 1.180$, $q = 0.691$, $Re = 10000$, maximum growth rate
  Fabre & Jacquin (1992): $f_i = 0.3119$
  Our Code: $f_i = 0.31189428825$

- $m = -3$, $\alpha = 1.582$, $q = 0.656$, $Re = 100$, maximum growth rate
  Fabre & Jacquin (1992): $f_i = 0.1431$
  Our Code: $f_i = 0.14305692$

6.5 Conclusion

We successfully validated the two and three-dimensional Chebychev spectral collocation codes developed in chapter 5. With the help of the 2D code, we performed a preliminary study of the inviscid and viscous linear stability analysis of an annular vortex. The mean vorticity profiles that we examined include step, tanh and the generalized Lamb-Oseen profile obtained in chapter 4. We find similar trends for growth rate vs m for the step, tanh and GLO profiles in that there is an upper cut off for unstable m. However, for the tanh and GLO profiles, we find the $m = 2$ disturbance to go unstable with two modes for a particular range of Re. In fact, this is also observed by Michalke & Timme (1967) for their smooth vorticity profile, where they find $m = 2$ unstable with a single mode. This behavior is in contrast to that of the step profile, where the

$m = 2$ is neutrally stable. Next, we observe that as we decrease Re, the maximum growth rate decreases along with the range of unstable m (upper cut off decreases). This is more so the case for the GLO profile than the tanh profile (where we observe anomalous behavior for high Re). Thus, in general, viscosity seems to have a stabilizing effect, damping out the higher modes. On the other hand, as the annulus becomes thinner, the maximum growth rate increases strongly along with the unstable range of m (upper cut off increases). Thus, an annulus of vorticity can go linearly unstable and potentially lead to the formation of multiple vortices. This however, would only happen if the growth rate of the instability is larger than the rate at which the radius of the annulus decreases by viscous diffusion.

Chapter 7

Conclusions

This thesis is a study of the merger of multiple vortices arranged on the vertices of regular polygons, and the work is summarized as follows.

In chapter 2, we developed an OpenMP fourier pseudo-spectral code to solve the vorticity streamfunction equations. In chapter 3, we validated the code and then studied the merger of n equal co-rotating vortices placed on the vertices of regular polygons. A key finding here is a new stage in the merger of multiple (three or more) vortices - an annulus which is long-lived, in contrast to the 'second-diffusive stage' in the two-vortex merger case. This stage involves the reduction in radius of an annular vortex by viscous diffusion to form one single vortex maximum. We are able to observe a quantitative and qualitative change in the separation distance as we go from two to six vortices, with the annular stage dominating the merger process as the number of vortices increases, effectively delaying the merger. In the three-vortex case, the vortices initially elongate radially, and then reorient their long axis closer to the azimuthal direction, and then diffuse out to form an annulus. The inviscid case is similar at short times, but at longer times, rather pronounced filaments are visible (in the three and four- vortex cases), which are practically absent in the viscous case. However, in the six-vortex case, the vortices initially itself align themselves azimuthally. Thus, we find a qualitative change in the tilt history as we increase the number of vortices from three to six and more, which is ultimately responsible for the change in separation distance history.

However, at high Reynolds numbers, the vortices merge asymmetrically and the annulus even undergoes instabilities. To gain a better understanding of the physics involved in this, we perform a linear stability analysis of an annular vortex. Assuming azimuthal symmetry, we find an analytical solution of the Navier-Stokes equation, (chapter 4) with the initial condition of an infinitesimally thin cylindrical vortex sheet. We obtain a Generalized Lamb-Oseen vortex profile, which reduces in radius by pure diffusion and ultimately evolves into a regular gaussian vortex. In chapter 5, we derived the viscous stability equations in cylindrical co-ordinates, and discretized them using a Chebyshev collocation technique. In chapter 6, we carried out a quasi-steady 2D viscous linear stability analysis of the time-frozen Generalized Lamb-Oseen vorticity profile. We find that in the infinite Reynolds limit (inviscid case), there is an upper cut-off for the azimuthal modes going unstable. In general, we find that viscosity has a stabilizing effect, tending to preferentially stabilize the higher modes. We also find two modes going unstable for the azimuthal wavenumber two, till a low Re limit, where only one mode goes unstable. In addition to this, we also validated the 3D viscous linear stability code, with a q-vortex as the mean flow.

References

Abramowitz, M. & Stegun, I. A. 1965 *Handbook of Mathematical Functions*. New York: Dover.

Batchelor, G. K. 1964 Axial flow in trailing line vortices. *J. Fluid Mech.* **20**, 645–658.

Batchelor, G. K. & Gill, A. E. 1962 Analysis of the stability of axisymmetric jets. *J. Fluid Mech.* **14**, 529–551.

Boyd, J. P. 2001 *Chebyshev and Fourier Spectral Methods*. Dover Publications, Inc.

Brandt, L. K. & Nomura, K. K. 2006 The physics of vortex merger: further insight. *Phys. Fluids* **18**, 051701.

Brandt, L. K. & Nomura, K. K. 2007 The physics of vortex merger and the effects of ambient stable stratification. *J. Fluid Mech.* **592**, 413–446.

Brown, G. L. & Roshko, A. 1974 On density effects and large structure in turbulent mixing layers. *J. Fluid Mech.* **64**, 775–816.

Canuto, C., Hussaini, M. Y., Quarteroni, A. & Zang, T. A. 2006 *Spectral Methods : Fundamentals in Single Domains*. Springer.

Cerretelli, C. & Williamson, C. H. K. 2003*a* A new family of uniform vortices related to vortex configurations before merging. *J. Fluid Mech.* **493**, 219–229.

Cerretelli, C. & Williamson, C. H. K. 2003*b* The physical mechanism for vortex merging. *J. Fluid Mech.* **475**, 41–77.

Chandrasekhar, S. 1961 *Hydrodynamic and Hydromagnetic Stability*. Oxford University Press.

Deem, G. S. & Zabusky, N. J. 1978 Vortex waves: Stationary "v states," interactions, recurrence and breaking. *Phys. Rev. Lett.* **40**, 859–862.

Dritschel, D. G. 1985 The stability and energetics of corotating uniform vortices. *J. Fluid Mech.* **57**, 95–134.

Dritschel, D. G. 1986 The nonlinear evolution of rotating configurations of uniform vorticity. *J. Fluid Mech.* **172**, 157–182.

Ehrenstein, U. & Rossi, M. 1999 Equilibria of corotating nonuniform vortices. *Phys. Fluids* **11**, 3416–3425.

Erdélyi, A. 1954 *Tables of Integral Transforms*. McGraw-Hill Book Company, Inc.

Fabre, D. & Jacquin, L. 1992 Viscous and inviscid instabilities of a trailing vortex. *J. Fluid Mech.* **500**, 239–262.

Flierl, G. R. 1988 On the instability of geostrophic vortices. *J. Fluid Mech.* **197**, 349–388.

Freymuth, P. 1966 On transition in a separated boundary layer. *J. Fluid Mech.* **25**, 683–704.

Gent, P. R. & McWilliams, J. C. 1986 The instability of barotropic circular vortices. *Geophys. Astrophys. Fluid Dyn.* **35**, 209–233.

Govindarajan, R. 2004 Effect of miscibility on the linear instability of two-fluid channel flow. *Intl. J. Multiphase Flow* **30**, 1177–1192.

Havelock, T. H. 1932 The stability of motion of rectilinear vortices in ring formation. *Phil. Mag.* **11**, 617–634.

Hopfinger, E. J. & van Heijst, G. J. F. 1993 Vortices in rotating fluids. *Ann. Rev. Fluid Mech.* **25**, 241–289.

Howard, L. N. & Gupta, A. S. 1962 On the hydrodynamic and hydromagnetic stability of swirling flows. *J. Fluid Mech.* **14**, 463–476.

Huang, M. J. 2005 The physical mechanism of symmetric vortex merger: A new viewpoint. *Phys. Fluids* **17**, 07415.

Khorrami, M. R., Malik, M. R. & Ash, R. L. 1989 Application of spectral collocation techniques to the stability of swirling flows. *J. Comp. Phys.* **81**, 206–229.

Lé Dizès, S. & Verga, A. 2002 Viscous interactions of two co-rotating vortices before merging. *J. Fluid Mech.* **467**, 389–410.

Leibovich, S. & Stewartson, K. 1983 A sufficient condition for the instability of columnar vortices. *J. Fluid Mech.* **126**, 335–356.

Lessen, M. & Paillet, F. 1974 The stability of a trailing line vortex. part 2. viscous theory. *J. Fluid Mech.* **65**, 769–779.

Mayer, E. W. & Powell, K. G. 1992 Viscous and inviscid instabilities of a trailing vortex. *J. Fluid Mech.* **245**, 91–114.

Melander, M. V., McWilliams, J. C. & Zabusky, N. J. 1987 Axisymmetrization and vorticity gradient intensication of an isolated vortex through filamentation. *J. Fluid Mech.* **178**, 137–159.

Melander, M. V., Zabusky, N. J. & McWilliams, J. C. 1988 Symmetric vortex merger in two dimensions: causes and conditions. *J. Fluid Mech.* **195**, 305–340.

Meunier, P., Ehrenstein, U., Leweke, T. & Rossi, M. 2002 A merging criterion for two-dimensional co-rotating vortices. *Phys. Fluids* **14**, 2757–2766.

Meunier, P., Lé Dizès, S. & Leweke, T. 2005 Physics of vortex merging. *C. R. Physique* **6**, 431–450.

Meunier, P. & Leweke, T. 2001 Three-dimensional instability during vortex merging. *Phys. Fluids* **13**, 2747–2750.

Meunier, P. & Leweke, T. 2005 Elliptic instability of a co-rotating vortex pair. *J. Fluid Mech.* **533**, 125–159.

Michalke, A. & Timme, A. 1967 On the inviscid instability of certain two-dimensional vortex-type flows. *J. Fluid Mech.* **29**, 647–666.

Overman, E. A. & Zabusky, N. J. 1982 A merging criterion for two-dimensional co-rotating vortices. *Phys. Fluids* **25**, 1297–1305.

Pozrikidis, C. 2011 *Introduction to Theoretical and Computational Fluid Dynamics*. Oxford University Press.

Rayleigh, J. W. S. 1880 On the stability, or instability, of certain fluid motions. *Proc. Lond. Math. Soc.* **11**, 57–70.

Rayleigh, J. W. S. 1917 On the dynamics of revolving fluids. *Proc. Roy. Soc. A* **93**, 148–154.

Roberts, K. V. & Christiansen, J. P. 1972 Topics in computational fluid mechanics. *Comput. Phys. Commun.* **3**, 14–32.

Rossow, V. J. 1977 Convective merging of vortex cores in lift-generated wakes. *J. Aircraft* **14**, 283–290.

Rotunno, R. 1978 A note on the stability of a cylindrical vortex sheet. *J. Fluid Mech.* **87**, 761–771.

Saffman, P. G. & Szeto, R. 1980 Equilibrium shapes of a pair of equal uniform vortices. *Phys. Fluids* **23**, 2339–2342.

Schubert, W. H., Montgomery, M. T., Taft, R. T., Guinn, T. A., Fulton, S. R., Kossin, J. P. & Edwards, J. P. 1999 Polygonal eyewalls, asymmetric eye contraction, and potential vorticity mixing in hurricanes. *J. Atmos. Sci.* **56**, 1197–1223.

Terwey, W. D. & Montgomery, M. T. 2002 Wavenumber-2 and wavenumber-m vortex rossby wave instabilities in a generalized three-region model. *J. Atmos. Sci.* **59**, 2421–2427.

Thomson, J. J. 1883 *A Treatise on the Motion of Vortex Rings*. MacMillan and Co.

Velasco Fuentes, O. U. 2005 Vortex filamentation: its onset and its role on axisymmetrization and merger. *Dyn. Atmos. Oceans* **40**, 23–42.

Winant, C. D. & Browand, F. K. 1974 Vortex pairing: the mechanism of turbulent mixing layer growth at moderate reynolds number. *J. Fluid Mech.* **63**, 237–255.

Zabusky, N. J., Hughes, M. H. & Roberts, K. V. 1979 Contour dynamics for the euler equations in two dimensions. *J. Comput. Phys.* **30**, 96–106.